

# Individualized prescriptive inference in ischaemic stroke

DOMINIC GILES<sup>1\*</sup>, ROBERT GRAY<sup>1</sup>, CHRIS FOULON<sup>1</sup>, GUILHERME POMBO<sup>1</sup>, TIANBO XU<sup>1</sup>, H. ROLF JÄGER<sup>1</sup>, JORGE CARDOSO<sup>2</sup>,  
SEBASTIEN OURSELIN<sup>2</sup>, GERAINT REES<sup>1</sup>, ASHWANI JHA<sup>1</sup>, PARASHKEV NACHEV<sup>1\*</sup>

*<sup>1</sup>UCL Queen Square Institute of Neurology, University College London, London, UK*

*<sup>2</sup>School of Biomedical Engineering & Imaging Sciences, King's College London, London, UK*

*\*Corresponding authors*

## Abstract

The gold standard in the treatment of ischaemic stroke is set by evidence from randomized controlled trials. Yet the manifest complexity of the brain's functional, connective, and vascular architectures introduces heterogeneity in treatment susceptibility that violates the underlying statistical premisses, potentially leading to substantial errors at both individual and population levels. The counterfactual nature of therapeutic inference has made quantifying the impact of this defect difficult. Combining large-scale meta-analytic connective, functional, genetic expression, and receptor distribution data with high-resolution maps of 4 119 acute ischaemic lesions, here we conduct a comprehensive series of semi-synthetic virtual interventional trials, quantifying the fidelity of the traditional approach in inferring individual treatment effects against biologically plausible, empirically informed ground truths, across 103 628 800 distinct simulations. Combining deep generative models expressive enough to capture the observed lesion heterogeneity with flexible causal modelling, we find that the richness of the lesion representation is decisive in determining individual-level fidelity, even where freedom from treatment allocation bias cannot be guaranteed. Our results indicate that complex modelling with richly represented lesion data is critical to individualized prescriptive inference in ischaemic stroke.

## Main text

Marked individual variability in response to treatment is near-universal across medicine. However plausible the therapeutic mechanism, determining the likely success of an intervention—for a specific patient and across the population—requires *inference from empirical observations of treatment outcomes*. The established inferential approach, enshrined in the randomized controlled trial (RCT), assumes our knowledge of individuals is limited to the average of the population, described simply enough to permit modelling with standard statistical methods under randomized treatment allocation<sup>1</sup>. The assumption of random inter-subject variability is secure where the underlying biological mechanisms are homogeneous across the population, but violated where they are heterogeneous, invalidating any inference that rests on it: for both the individual patient and the whole population<sup>2</sup>. For example, in the presence of two sub-populations of equal size and diametrically opposite responses—one negative, one positive—the average treatment effect will tend towards zero, regardless of the statistical power of the study, the quality of the data, and the magnitude of subpopulation-specific effects (Figure 1). Crucially, heterogeneity is not detectable within the trial evaluation itself, nor necessarily in any subsequent subgroup analysis based on the same description of the population<sup>3</sup>. Only where the heterogeneity is explicitly exposed by an identified covariate—the differentiation between ischaemic and haemorrhagic stroke in thrombolysis offers a striking example<sup>4</sup>—may the inferential error be detected.

This cardinal problem has three major consequences. First, an intervention may be mistakenly judged to be ineffective for all when it benefits an identifiable many, prematurely dismissing a valuable treatment, wasting the cost of its development, and discouraging further research into its mechanism and application<sup>5</sup>. Second, an intervention may be avoidably prescribed to those who do not respond or are harmed by it, degrading clinical outcomes, exposing patients to unnecessary risk, and promoting systematic inequalities in care. Third, since RCTs have been placed on the highest pedestal, at the apex of the hierarchy of clinical evidence, neither argument nor data outside the established framework is permitted to gainsay them, indefinitely perpetuating both the errors and their consequences<sup>6</sup>.

Arguably nowhere is this defect more important than in stroke, worldwide the second commonest cause of death and the commonest cause of adult neurological disability<sup>7,8</sup>. Though the aetiology is comparatively simple—vascular rupture, occlusion, or both—and the immediate treatment commensurately focused<sup>9,10</sup>, the functional deficits subsequent management must address may be as complex as the organization of the brain itself<sup>11</sup>. The observed patterns of disability, responses to treatment, and long-term recovery all suggest marked heterogeneity<sup>12</sup>, explicitly violating the assumptions on which conventional interventional inference rests. Indeed, what we know of the functional anatomy of the brain<sup>13</sup>, and the topology of ischaemic lesions, makes it inevitable that their interaction in stroke should exhibit a complex but nonetheless organized structure that may not be dismissed as random noise<sup>14–16</sup>. A “one-size-fits-all” assumption is not only biologically implausible here: it is directly contradicted by the facts<sup>2</sup>.

Without a means of capturing this heterogeneity historically, we have had no option but to ignore it<sup>17</sup> or model it in an oversimplified manner<sup>18</sup>. But the combination of machine learning with large-scale data now renders statistical models of sufficient expressivity and flexibility computationally tractable and deployable in real world practice. Inferences about individuals may now be informed by the local subpopulation to which they belong—defined by many clinical, physiological, and anatomical characteristics—quantifying individual treatment effects opaque to the global population-level perspective that is the limit of conventional methods. Within such *individualized prescriptive inference*, the underlying statistical model seeks to determine not the *average treatment effect* across the population, but the *conditional average treatment effect* informed by the

patient's distinctive features, resulting in more faithful individual-level estimates with reduced systematic variability across the population<sup>19</sup>. Just as the now familiar heterogeneity of ischaemic vs haemorrhagic stroke was resolved by brain imaging, so as yet unknown heterogeneities defined by multiple factors may be resolved by complex modelling of rich data<sup>12,20-22</sup>.

How do we realize such an individualized approach? Where available, observations of responses to unbiased treatment allocation—such as from a traditional RCT—may be combined with established low-<sup>23</sup> or novel high-dimensional<sup>16</sup> multivariable modelling of conditional outcomes. But in the setting of unknown heterogeneity defined by *many* interacting factors, the necessary data scale becomes infeasibly large, forcing reliance on routine clinical data streams with limited control over randomization. We must therefore determine the *comparative* importance of minimizing treatment allocation bias *vs* maximizing model expressivity and flexibility in inferring the optimal treatment for each individual patient. If generalizable individual-level accuracy is shown to be more sensitive to bias than to modelled heterogeneity, then a RCT remains the optimal approach. Conversely, if model expressivity and flexibility are shown to be decisive, then achieving the data scales machine learning requires—and only routine clinical streams can provide—becomes paramount.

Examining the largest set of registered acute stroke lesion data ever assembled—4 119 lesions—here we perform a comprehensive comparison of the individual-level fidelity of traditional interventional inference—randomized allocation with simple covariate adjustment—*vs* a novel approach—flexible counterfactual modelling of non-randomized data based on deep representation learning. Our analysis tests the hypothesis that capturing treatment response heterogeneity with generative models of the necessary expressivity, in combination with flexible causal models, may be substantially *more* important than unbiased treatment allocation in inferring optimal individual treatments. On the answer rests the right choice of inferential approach in evaluating treatments in acute stroke sensitive to the functional organization of the brain.

This comparison *can only be performed with semi-synthetic counterfactuals*, within a potential outcomes framework<sup>24</sup>, for our knowledge of real conditional outcomes is both wholly empirical and derived from the very inferential approach we are testing<sup>25-29</sup>. To use data within the RCT framework is to beg the question of what the right standard should be: our task here. To assure real-world generalizability, our simulations are maximally informed by complex multi-modal empirical data: high-resolution lesion anatomy, and meta-analytic functional<sup>30</sup>, gene transcription<sup>31</sup>, and neurotransmitter receptor<sup>32</sup> maps. Moreover, we traverse a wide space of plausible real-world circumstances—the richness of lesion parameterization, the magnitude and variability of treatment effects, the extent of treatment allocation bias, and the biological nature of the underlying deficit and treatment susceptibility—across the largest set of simulations ever performed with brain lesion data of any kind.

Following well-established principles of causal inference<sup>33-35</sup>, our approach relies on a causal model, represented by a directed acyclic graph, of the spatial relationship between brain lesions and functional anatomy—a map of disrupted functions—and between treatment receipt and physiological anatomy—a map of treatment susceptibility—that explains observed patient outcomes (Figure 2). This formulation allows us to quantify the impact on the fidelity of individual treatment recommendation of *both* observable *and* unobservable treatment assignment bias, across the full space of plausible real-world scenarios, including a wide range of treatment and spontaneous recovery effects. We can thus directly address the question of the relative contribution of randomization—the advantage of RCTs—and greater model expressivity and flexibility—the advantage of complex models of large-scale observational data.

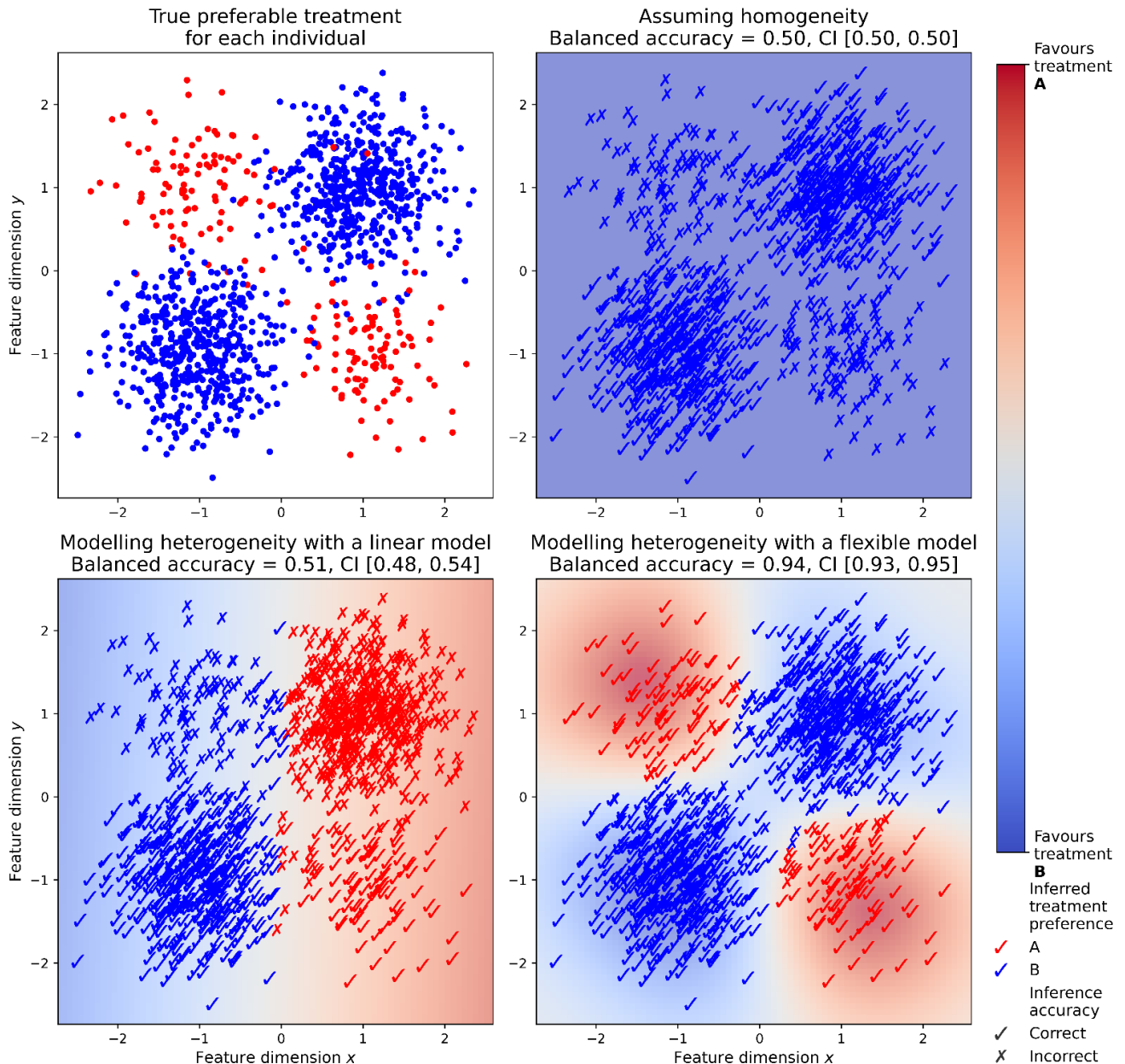


**Figure 1. Inferring treatment effects in the setting of heterogeneity.** Consider a hypothetical scenario where the members of a population described on continuous dimensions ( $x$  &  $y$ ) systematically differ in their susceptibility to two treatments (A (red) & B (blue)). The two populations differ in size (A is smaller), and are non-linearly distinguished by their features (occupying diametrically opposed quadrants of the feature space). A statistical model of the optimal treatment that ignores the heterogeneity entirely, unconditionally averaging across all patients, inevitably favours B wholesale as the larger proportion, achieving chance level balanced accuracy (upper right). A model accounting for heterogeneity in simple, linear terms (a linear support vector machine) achieves only slightly better accuracy, for the distinguishing features are not linearly separable (lower left). By contrast, a model flexible enough to absorb complex, non-linearly defined heterogeneity (a support vector machine with a radial basis function kernel) achieves near perfect balanced accuracy (lower right). Note the differences in fidelity here can only be entrenched by higher quality or larger scale data, for they are a consequence not of the data or its sampling but of the mismatch between the complexity of the data and the flexibility of the statistical model.

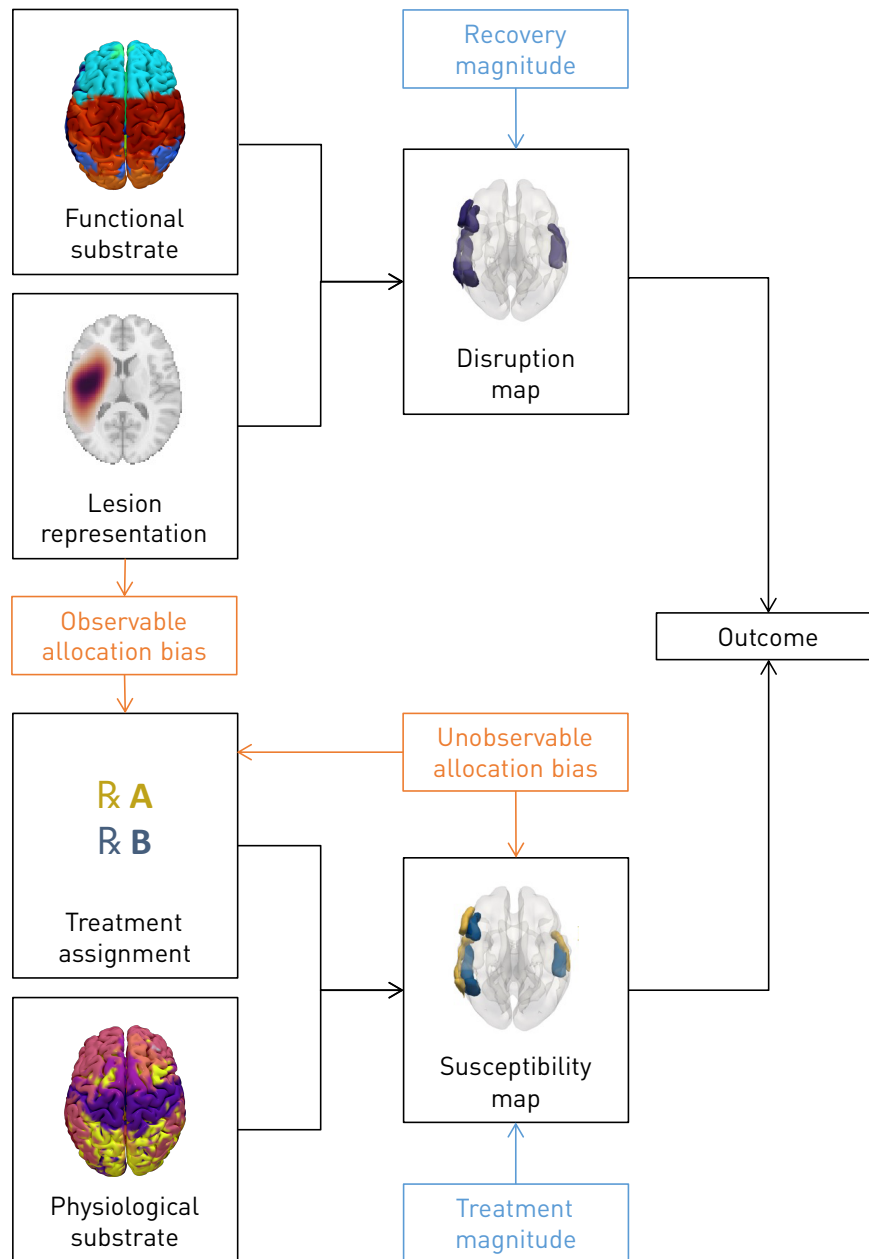
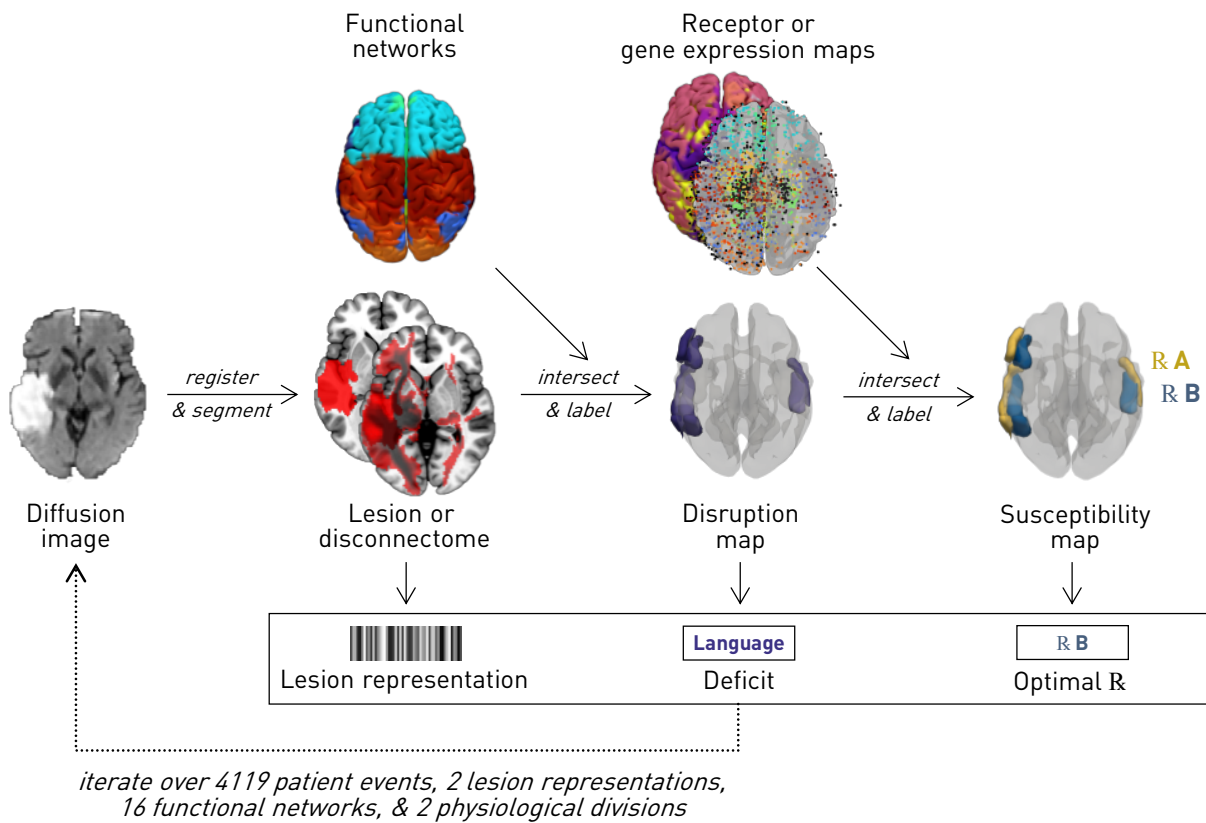


**Figure 2. Causal modelling of treatment—conditional outcomes in stroke.** Directed acyclic graph of the modelled causal relations between brain lesions and functional anatomy—a map of disrupted functions—and between treatment receipt and physiological anatomy—a map of treatment susceptibility—in generating the observed outcome. The lesion anatomical representation (lesion or disconnectome) interacts with the functional substrate to generate a data-driven functional *disruption map*; in parallel, hypothetical treatment assignment interacts with the physiological substrate (microarray RNA transcription or neurotransmitter receptor data) to generate a data-driven treatment *susceptibility map*. These two spatial maps intersect to generate the patient outcome, modulated by the magnitudes of recovery and treatment effects. The relationships are modelled to be corrupted by varying degrees of observable or unobservable treatment allocation bias, enabling quantification of their impact on the fidelity of inferred optimal treatment.

## Ground truth generative process



## Virtual interventional trials

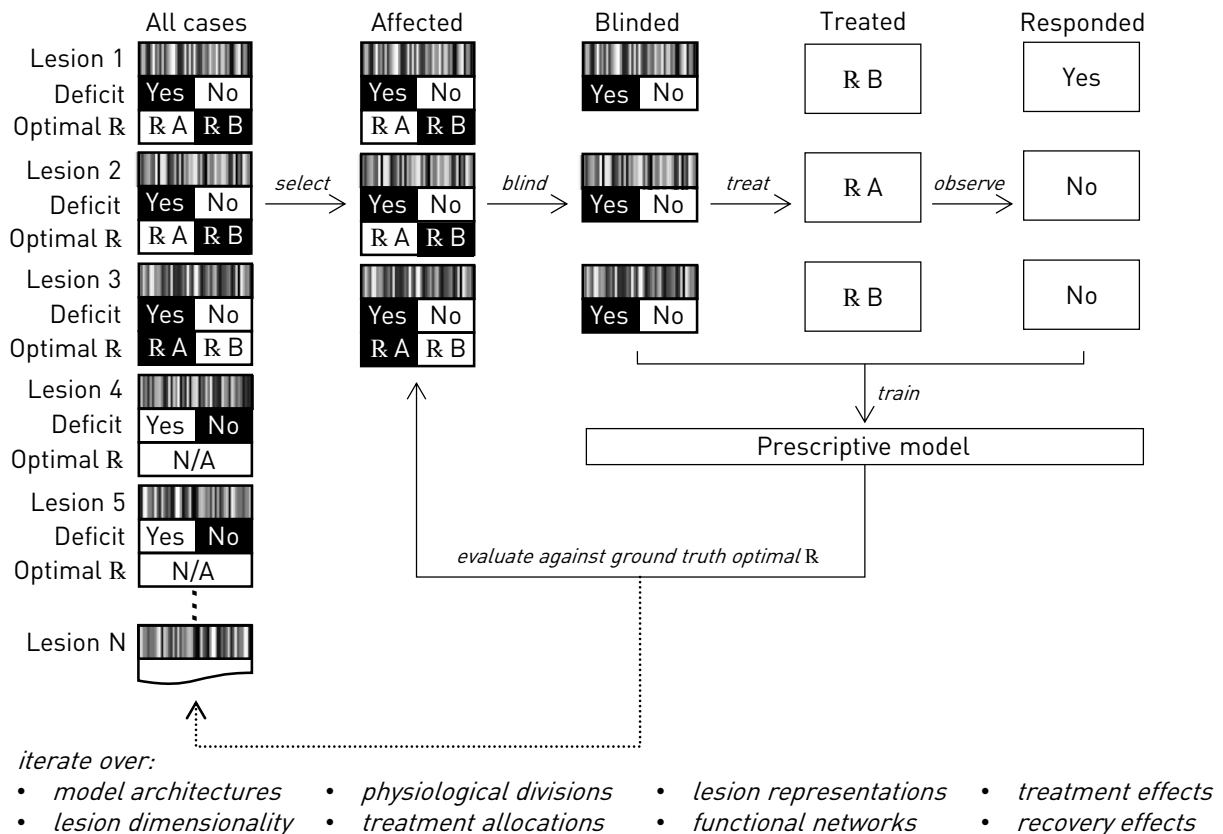


**Figure 3. Semi-synthetic ground truth synthesis (upper panel).** Schematic of the process of semi-synthetic ground truth generation from lesions or disconnectomes, given meta-analytic maps of brain functional organization and physiology. Diffusion weighted magnetic resonance images were obtained from patients with confirmed acute ischaemic stroke. Each image volume was non-linearly transformed into Montreal Neurological Institute (MNI) template space, facilitating voxel-based comparisons between different lesioned images and with meta-analytic functional and physiological maps. A binary ischaemic mask was automatically segmented from each image, and used to simulate real-world individual-level variability of functional deficits and treatment responses. The overlap between each lesion and each of 16 meta-analytic functional grey matter networks, transformed into MNI space, was used to generate plausible synthetic functional deficits (lesion—deficit simulation). The anatomical territory associated with each functional network were further subdivided by transcriptome or receptome distribution data into two subregions, variably responsive to different hypothetical interventions, furnishing treatment effect heterogeneity. A plausible anatomically determined ground truth for hypothetical treatment susceptibility is thereby established, enabling explicit quantification of the fidelity in inferring the optimal treatment. The resulting semi-synthetic data comprise stroke phenotype representations, associated functional deficits, and the designated optimal treatment for each patient simulation.

**Virtual interventional trials (lower panel).** We used Monte Carlo methods to simulate a large number of virtual trials across the full set of modelled lesion-deficit relationships, treatment susceptibilities, and treatment allocation policies. For each functional network, all patients with corresponding deficits were virtually recruited to receive one of two hypothetical treatments, of which at least one was modelled as truly effective. Non-random treatment allocation as may occur in an observational setting was simulated using an allocation bias parameter, ranging from 0 (randomized) to 1 (treatment selection based strongly upon patient phenotype). A patient's response to a given treatment was dependent upon two sources of probabilistic noise: treatment effect,  $\mathbb{P}(\text{response} | \text{truly susceptible})$ , and recovery effect,  $\mathbb{P}(\text{spontaneous response})$ , independent of treatment received and susceptibility. These sources of noise are always present to some degree in any trial, randomized or observational. Within 10-fold cross-validation, prescriptive models were fitted using the training set, with quantified noise and bias, for the objective of retrieving the optimal treatment, to each individual patient. The model was evaluated using a held-out test set, for lesion representations, disconnectome representations, functional networks, gene expression-derived treatment susceptibility subnetworks, and receptor distribution-derived treatment susceptibility subnetworks, across the ranges of allocation bias, treatment effect and recovery effect.

## Results

To test our hypothesis, we must first establish a semi-synthetic framework for empirically-informed *virtual interventional trials* (Figure 3). A real trial is inadequate, for the success or failure of a treatment has no ground truth against which the fidelity of the inference can be quantified. Since the disability caused by a stroke is directly related to the underlying disrupted functional anatomy, it is natural to posit lesion—deficit relations in terms of observed, potentially disrupted, neural patterns of functional organization. Equally, susceptibility to treatments acting downstream of the vascular disruption—e.g. tissue preservation, modulation, or regeneration—is plausibly sensitive to the biological properties of the damaged or threatened substrate. Our semi-synthetic simulation framework therefore combines lesion—deficit ground truth maps from functional anatomical data with treatment susceptibility ground truth maps from physiological, receptor distribution and genetic expression data. Both sets of simulated ground truths are derived from comprehensive, large-scale, meta-analytic data in the public domain. Finally, we need a large, maximally inclusive collection of acute stroke lesion maps that is plausibly representative of the heterogeneity of the population, registered into a common anatomical space to allow faithful comparison between individuals. A small sample biased by selective recruitment would inevitably lead to under-estimates of observed heterogeneity and our capacity to model it.

### **A data-driven map of functional networks in the human brain**

To construct a set of hypothetical ground truth lesion-deficit relations maximally grounded in real-world evidence, we derived a hierarchical grey matter functional parcellation of the human brain from a comprehensive analysis of NeuroQuery meta-analytic functional imaging and associated textual data<sup>30</sup>. Hierarchical voxel-based clustering of individual behavioural and cognitive terms based on the similarity of corresponding neural activation patterns yielded 16 distinct functional networks covering the full range of imaged behaviours (Figure 4; Supplementary Figure S1). Remarkably, though the clustering was driven solely by these activation patterns, strong commonalities in the keyword terms belonging to each cluster emerged—across the network archetypes of hearing, language, introspection, cognition, mood, memory, aversion, co-ordination, interoception, sleep, reward, visual recognition, visual perception, spatial reasoning, motor, and somatosensory—corroborating the fidelity of the mapping approach (Supplementary Figure S2). Each of these 16 archetypal functional networks provided a plausible ground truth for the critical neural substrates of the associated group of behaviours, replicating the likely spatial form and complexity of actual lesion—deficit relations, across the entire behavioural landscape.

### **Gene expression and receptor-determined treatment susceptibility**

To create biologically plausible patterns of treatment response heterogeneity, individual variation in response was determined by further subdivision of the functional networks guided by physiological, whole-brain gene expression maps<sup>31</sup> or by neurotransmitter receptor distributions<sup>32</sup>. A deficit associated with a given functional network could thus be designated as preferentially susceptible to one of two hypothetical treatments, dependent on which gene expression or receptor-directed subdivision (Supplementary S9 & S10) is primarily disrupted by a given lesion. Crucially, treatment susceptibility, like the deficit itself, is thereby rendered sensitive to the anatomy of the lesion in its interaction with plausibly material biological features. Again, the objective is to replicate the likely form and complexity of anatomically organized determinants of susceptibility, not to identify them for any specific function.

## Lesion-deficit and treatment response simulation

A set of 4 119 non-linearly registered diffusion-weighted (DWI) magnetic resonance images from 2 830 unique unselected patients with confirmed acute ischaemic stroke was used to create a set of empirically informed, simulated lesion-deficit relations (Figure 3, upper panel; Figure 5). Though a proportion were drawn from the same patient, no images from within the same 30-day period from the same individual were retained in the dataset, as visualized in Supplementary S3.

Lesion binary masks automatically segmented from each DWI and transformed into standard MNI stereotactic space were intersected with each of the 16 functional grey-matter networks, yielding 4 119 lesion-deficit relations across the full range of lesions and behaviours. A lesion intersecting with  $\geq 5\%$  of a subnetwork was designated as causing a corresponding deficit. To capture the broader impact of lesions on grey matter-defined functional areas through white matter damage, “disconnectome” representations were also generated from each lesion mask<sup>36,37</sup>, extending each lesion to remote grey matter areas disconnected by it, weighted in proportion to the extent of connectivity (Figure 5). Disconnectome deficits were analogously designated, using a threshold of 0.5 to binarize the representation.

For each lesion and each functional network it affects, the intersection with the physiological subdivisions was used to designate susceptibility to one of two hypothetical treatments, qualifying each lesion—deficit pair by a hypothetical treatment susceptibility, and enabling us to conduct biologically plausible virtual interventional trials.

## Prescriptive inference with virtual interventional trials

With an individual-level ground truth in place, we conducted a series of virtual interventional trials, where each patient event—defined by empirical lesion anatomy, the corresponding simulated deficit, and simulated treatment susceptibility—was allocated to receive one of two hypothetical treatments differing in their individual-level effects as outlined above (Figure 3, lower panel). The task, as in a real trial, is to infer treatment susceptibility from a model of the lesion, the deficit, and treatment allocation alone. Unlike a real trial, however, here we can quantify the fidelity of the inference against an explicit individual-level ground truth, enabling us to compare the performance of different models and experimental settings objectively<sup>24</sup>.

To capture the full space of possible treatment and response scenarios, we varied both treatment and recovery effects across their entire possible range within independently conducted trials. Similarly, to capture allocation bias effects, we varied treatment allocation from random (no bias) to directly determined by the location of the centroid of each lesion (high bias). An alternative allocation bias regime for based on unobserved covariates was additionally implemented. The complete combination of these parameters—functional network, treatment susceptibility, lesion representation, treatment effect, recovery effect, and allocation bias—yielded 22 528 separate virtual clinical trial conditions, of which a 10-fold cross-validation scheme was implemented and results evaluated over 460 representation—prescriptive configuration combinations, leading to a total of 103 628 800 simulations.

For each trial, we built a series of flexible multivariate models of counterfactual individual treatment outcome—prescriptive inference—based on extremely randomized trees<sup>38</sup>, XGBoost<sup>39</sup>, random forest<sup>40</sup>, Gaussian process<sup>41</sup>, and logistic regression<sup>42</sup>, incorporating treatment allocation, observed outcome, and lesion anatomy, trained and tested on independent, randomly selected subsets of the data. These models fit a function predictive of individual counterfactual outcome, given each intervention, that generalizes to unseen patients. Optimal treatment can thus be prescribed by selecting the intervention with the greatest

predicted probability of success, and the fidelity of the prescription can be quantified against the ground truth.

To quantify the value of capturing the anatomical detail of lesions with expressive representational models, each stroke lesion representation (binary lesion mask or disconnectome) was compressed, using a volume variational deep auto-encoder (VAE)<sup>43</sup>, volume non-variational deep auto-encoder (AE), non-negative matrix factorization (NMF)<sup>44</sup> and principal component analysis (PCA)<sup>45</sup> to latent embeddings of varying length up to 50 components<sup>14</sup>. Independent models employing progressively higher dimensional representations were then compared against the baseline low-dimensional lesion representations typically employed in conventional stroke trials, vascular territory (anterior circulation ischaemic stroke or posterior circulation ischaemic stroke), or 6 specific arterial divisions, adapted from the atlases presented by Liu et al<sup>46</sup>. Each trial was thus evaluated with 46 representations: two low-dimensional baselines and eleven incrementally higher dimensional ones across four representational rationales.

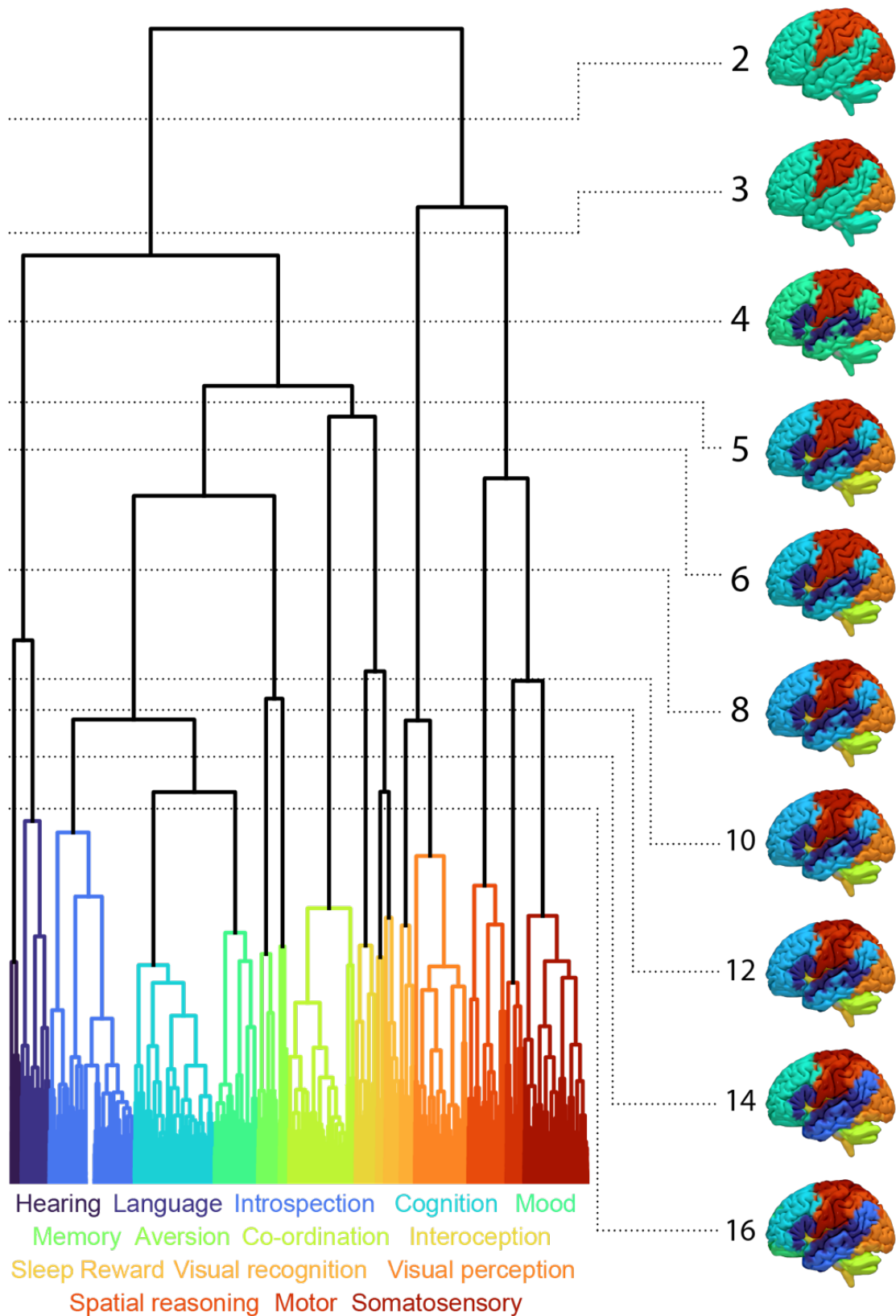


**Figure 4. Functional ground truths.** Functional grey matter parcellation dendrogram, showing agglomerative voxel-based clustering based upon association distances between voxels in their functional distributions. Visualizations of functional groupings at various thresholds up to 16 are shown on the right, displaying the grey matter functional hierarchy. From the 16-network parcellation, the archetypal terms associated with each group are shown below the dendrogram, with consistency of colours throughout.

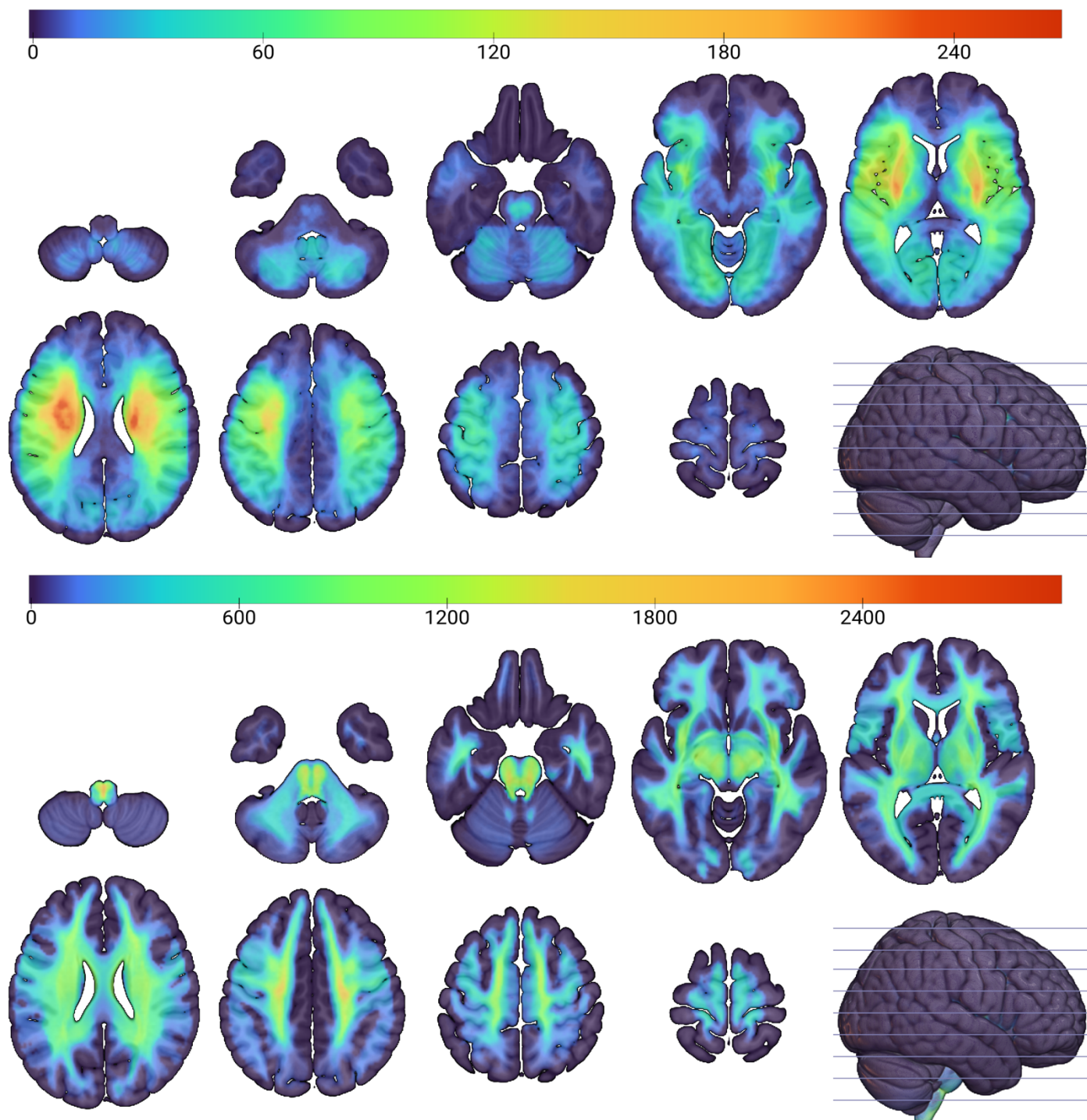


**Figure 5. Lesion (upper panel) and disconnectome (lower panel) anatomical distributions.** Axial slices showing the coverage in voxel-based summation of binary ischaemic maps of lesions (upper), and the summation of binarized disconnectome distributions ( $p > 0.5$ ) associated with each of the lesions (lower), showing coverage across the brain. For both representations,  $N = 4\ 119$ .

## Prescriptive inference is limited by model dimensionality, not allocation bias

Under statistically ideal conditions—large treatment effects, infrequent spontaneous recovery, random allocation—richly expressive representations achieved significantly higher individual-level predictive fidelity than simple vascular baseline models overall (Figure 6, upper left corners of each panel; Figure 7, upper row of each panel).

With lesion masks as the input, balanced accuracy for inferring the optimal treatment from the 50-dimensional VAE representation, averaged across all 16 functional networks, was 0.793 [95% CI [0.75, 0.84]], vs 0.523 [95% CI [0.50, 0.55]] for a simple vascular baseline ( $t = 10.5$ ,  $p = 1.66 \times 10^{-18}$ , Cohen's  $d = 1.96$ ). A similarly striking difference was revealed by precision-in-estimation-of-heterogeneous-treatment-effects (PEHE, lower is better), yielding 0.466 [95% CI [0.44, 0.49]] for the 50-dimensional VAE representation vs 0.676 [95% CI [0.63, 0.72]] for the simple vascular baseline ( $t = -8.12$ ,  $p = 3.92 \times 10^{-13}$ , Cohen's  $d = -1.44$ ), indicating superiority of the richly expressive representation across both metrics.

With disconnectomes as the input, balanced accuracy from the 50-dimensional VAE representation was 0.875 [95% CI [0.83, 0.92]], vs 0.546 [95% CI [0.52, 0.57]] for the simple vascular baseline ( $t = 13.5$ ,  $p = 4.28 \times 10^{-24}$ , Cohen's  $d = 2.62$ ); by PEHE, 50-dimensional VAE yielded 0.349 [95% CI [0.33, 0.37]] vs 0.592 [95% CI [0.56, 0.63]] for the simple vascular baseline ( $t = -10.2$ ,  $p = 2.86 \times 10^{-17}$ , Cohen's  $d = -2.13$ ), similarly indicating broad superiority of the richly expressive representation.

With increasing noise—small treatment effects, frequent spontaneous recovery—the advantage of the richly expressive representations remained significant across most of the parameter space (white filled circles in Figure 6, right column; Figure 7, upper right panel), except for the noisiest settings where no statistical distinction could be made. Crucially, this relationship persisted even under strong corruption by allocation bias (white filled circles in Figure 6, right column; Figure 7, lower right panel), generally yielding higher prescriptive fidelity even from a markedly biased and noisy trial modelled with a richly expressive representation than from a fully randomized trial at the same noise level modelled with a simple one.

The observed patterns of comparative performance were broadly invariant when averaged across the criteria of treatment susceptibility—transcriptome or receptome (Figure 6a, b); lesion anatomical representation—lesion masks or disconnectomes (Figure 6c, d); and observability of treatment allocation bias—location-based or unobservable (Figure 6e, f). A high-dimensional representation, even in the setting of strongly biased allocation, was almost always at least non-inferior to a RCT employing low-dimensional models, and in the vast majority substantially superior. These findings were consistently replicated across most functional deficit simulations (Figure 7), based on the functional—anatomical networks visualized in Supplementary S9 and S10. An identical analysis based on PEHE demonstrated the same overall patterns (Supplementary S11-17).

These results provide strong grounds for rejecting the null hypothesis of no superiority of richly expressive representations under biased treatment allocation conditions vs low-dimensional models under randomization.

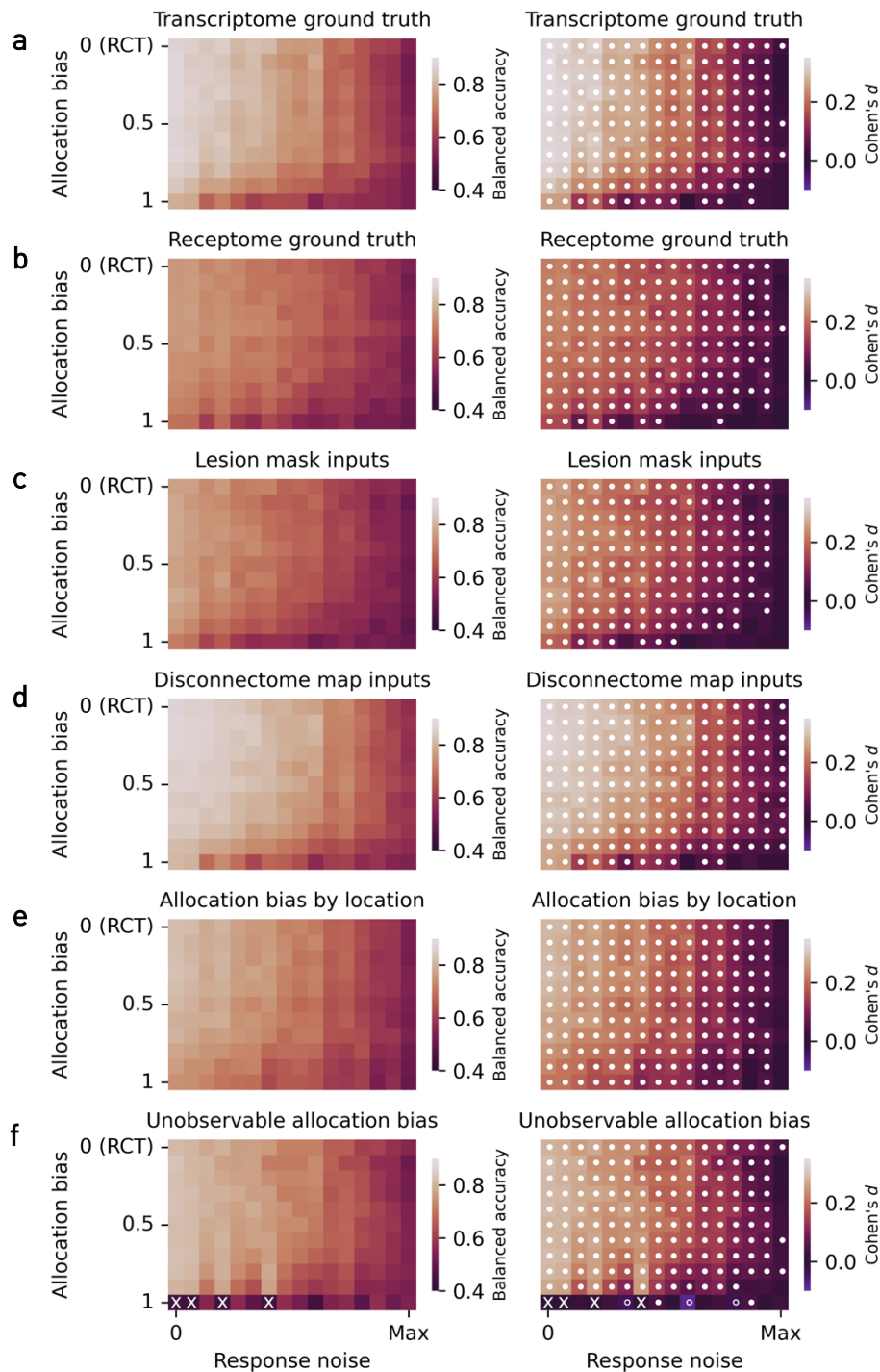


**Figure 6.** Prescriptive performance with the optimal richly expressive representation quantified by balanced accuracy (left panel column, see Supplementary S11-S14 for full descriptions), and statistical comparison against a simple vascular baseline, anterior or posterior vascular territories (right panel column). A filled circle indicates significantly higher performance for the expressive representation, and an unfilled circle significantly higher performance for the baseline model (using a Benjamini-Hochberg corrected critical value for 0.05 significance level). An 'x' indicates simulation conditions with insufficient class balance to permit prescriptive model fitting (e.g. because there are no non-responders). Rows **a** and **b** show performance averaged across the criteria for treatment susceptibility (transcriptome or receptome); rows **c** and **d** across lesion input representation type (lesion masks or disconnectomes); and rows **e** and **f** across allocation bias observability (location-based or unobservable). The optimal expressive representation is shown to be non-inferior to simple vascular territories at informing prescription across almost the full landscape of observational conditions, and superior in the vast majority. See S15 for respective PEHE plots.

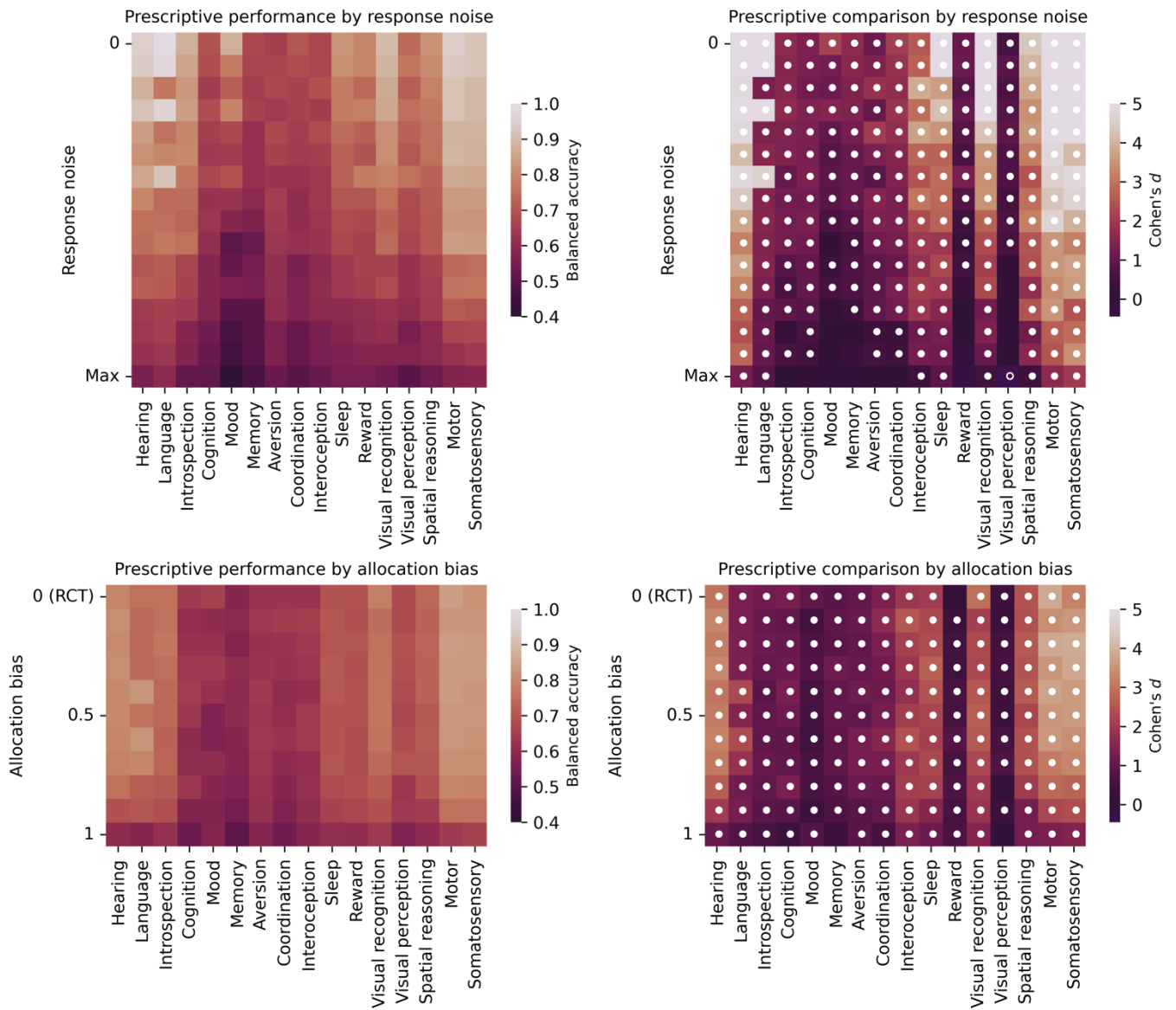


**Figure 7.** Prescriptive performance with the optimal richly expressive representation quantified by balanced accuracy (see S11-S14 for full description), stratified according to the modelled functional deficit, and averaged across all simulation conditions. The right column shows Cohen’s  $d$ -effect size when comparing prescriptive performance using the optimal representation against a simple vascular baseline. A filled circle indicates superior performance for the optimal representation, beyond the Benjamini-Hochberg corrected critical value for 0.05 significance level; an unfilled circle indicates superior performance for the simple vascular baseline correspondingly. The full anatomical—physiological modelling framework is visualized in Supplementary S9 & S10 for receptome and transcriptome, respectively. The advantage in prescriptive performance for the richly expressive approach is shown to generalize across modelled functional deficits as well as data conditions defined by outcome response noise and treatment allocation bias. See S16 for respective PEHE plot.

## Discussion

We address a cardinal question in the domain of ischaemic stroke: the optimal approach to evaluating a treatment where the deficit and treatment susceptibility may exhibit sensitivity to anatomical patterns of functional activation, neurotransmitter receptors, gene expression, or other neural properties of similar spatial structure. This is a question no-one has previously examined. Yet the unusually large number of interventions discarded at the trial stage<sup>47</sup>, and the protracted history of those now persuasively shown to be beneficial<sup>48</sup>, cast doubt on the felicity of the established approach. Moreover, the picture of the brain emerging at every level—from the molecular to the physiological—indicates a finely granular, replicable organization overwhelmingly likely to result in treatment heterogeneity that invalidates the kind of inference interventional trials currently employ. Not only may we not assume that conventional RCTs will converge on the correct inference here, there are strong reasons for doubting the fundamental grounds on which they rest<sup>5</sup>. Given the sheer scale of stroke worldwide, millions of years of disability may be lost not because we do not have the good treatments but because we have failed to mitigate the impact of heterogeneity on the determinability of their effects.

Crucially, this is not a question that can be answered with conventional empirical studies alone. When—as almost always—only one of many treatments can be offered to a given patient, the question of which is optimal is counterfactual, to be settled by inference across a population of patients for which there can be no hard ground truth. A failure of inference here cannot be distinguished from a failure of the intervention, and if the inferential approach is never questioned, replication will not correct the error but typically entrench it. It is striking that whereas absence of evidence is understood not to constitute evidence of absence, negative RCTs are widely interpreted as conclusive proof of a lack of meaningful therapeutic effect<sup>49</sup>, for provided the trial has been correctly conducted, no other outcome is assumed to be possible<sup>6</sup>.

The only way to address this urgent question is through semi-synthetic simulations where the space of hypothetical treatment—outcome relationships is comprehensively surveyed with as much biological constraint as the problem permits. If we can show that one inferential approach is superior to another—*across the broadest accessible space of hypothetical possibility*—we need not have evaluated any *specific* relationship for our conclusions plausibly to generalize across the field. Here we therefore combine the largest and most diverse collection of stroke lesion anatomical maps ever assembled with functional<sup>30</sup>, genetic expression<sup>31</sup>, and receptor distribution<sup>32</sup> maps drawn from the largest accessible data scales, and evaluate the treatment—outcome relationships across the full range of magnitudes of treatment and recovery effects. Our analysis spans 103 628 800 prescriptive simulations, involving >72 000 CPU-core hours of computation on a high-performance cluster. Evaluating any specific treatment-outcome relationship—however finely described and empirically corroborated—would not be sufficient, because generalization across arbitrary relationships would remain untested.

Our analysis shows that the expressivity of the representational models used to infer treatment effects has a profound impact on their fidelity, across the surveyed space of hypothetical possibility, irrespective of the representation of the lesion, the functional domain of the deficit, or the source—receptor or gene expression—of the determinants of treatment susceptibility. The use—near universal in the field—of simple, highly reductive lesion descriptors, such as crude vascular territory, is revealed to be suboptimal. Now that advances in machine learning have made rich representation of stroke lesions easily realisable, failing to model lesion architecture with the granularity the underlying anatomical relationships demand is hard to justify.

The superiority of inference with complex models extends to the setting of biased treatment allocation such as observational studies inevitably risk. We show that richly expressive models of non-randomized data are typically superior to simple models of fully randomized data even where strong allocation biases are present. Though randomization itself is always desirable, it is shown to matter *less* than representational expressivity. Where resourcing or other constraints force a choice between achieving the data scales complex models demand in an observational context vs conducting a RCT with simple methods, the latter may no longer be assumed to be preferable, indeed our findings suggest the contrary. Where resources permit it, randomization may, of course, be combined with complex modelling; equally, an effect drawn from observational data may be subsequently evaluated with randomized, prospectively acquired data from plausibly homogeneous subpopulations.

That there are bound to be aspects of treatment—revascularization, for example—where a therapeutic mechanism may be simple and general enough to be captured with conventional inferential methods does not imply that alternatives should be pursued only where the mechanism is plausibly complex. The critical outcome measure in stroke—as in medicine generally—is the impact on the patient’s life, which is here expressed through the complex interaction between the anatomical patterns of damage and the functional organization of the underlying neural substrate. If one link in the chain of causation requires it, a more flexible inferential approach must be used for all. Even revascularization requires reference to the structure of the vascular tree, whose intricate organization entails the possibility of complex heterogeneity. In any event, our mechanistic knowledge is rarely, if ever, sufficiently secure to place hard bounds on the requisite model flexibility.

Equally, though we may use a highly compressed representation—a two-dimensional embedding of lesion anatomy, for example—to stratify patients upstream of randomization within an otherwise conventional RCT, the loss of fidelity in the compression may offset any gain in enabling randomization. Representation learning dependent on large-scale data would be required anyway, for the quality of the embedding is likely to be at least as dependent on data scale as a discriminative model of comparable flexibility. It is highly unlikely that overt—rather than latent—low-dimensional descriptors can commonly be found, for no (say) blood-borne signal could plausibly capture anatomically distributed information.

Though model compactness should be encouraged, the objective to be maximized here is generalizable individual-level fidelity, not interpretability. The representational machinery we use permits the visualization of latent lesion archetypes (Supplementary S4 & S5), grounding prescriptive recommendations in an anatomically meaningful “lexicon”. Our extremely randomized trees-based prescriptive models, though highly flexible, also offer feature importances, explicitly quantifying the influence that each lesion component exerts on the prescription. Note there is no ethical basis for preferring a low-fidelity, readily interpretable model over a higher fidelity, comparatively opaque one. In any event, the matter cannot be settled without soliciting the views of patients and the public at large, to whom this choice has never been presented.

Unmodelled heterogeneity is not merely a statistical nuisance, limiting our power to identify the correct treatment at the individual level. It has consequences for medical equity, for where a failure of inference affects a distinct subpopulation, systematic epistemic inequity is introduced<sup>50</sup>. That the disadvantaged may here be identified by multiple interacting factors—creating diverse, intersectional groups—and that the defining factors may lie outside recognized protected characteristics, does not make the resultant inequity any less significant. Medicine has a duty to maintain equity across all, regardless of the basis for their identity.

Medicine also has a duty to make the maximum use of the knowledge it draws from individual patients, often at some discomfort to them, and always at a cost to someone. For treatments already in widespread use, individually prescriptive systems can be built on—and delivered through—established clinical streams. Not only may such systems render the process of individual prescription objective and easily scalable beyond specialist centres, they enable fine-tuning to local populations, including in response to dynamic changes over time, in a way wholly unattainable within the RCT framework. Note that the relevant features of ischaemic stroke—discrete spatial signals with high contrast-to-noise ratio on routine diffusion-weighted imaging—are comparatively invariant to the imaging instrument, and easy to project into standard stereotactic space, rendering the modelling pipeline readily implementable. Indeed, our study exclusively uses clinical data collected in the course of routine practice, drawn from a wide diversity of scanners and image sequence types.

Finally, in common with all inference, our framework depends on foundational assumptions about the nature of the underlying causal relationships and their accessibility to imperfect observation. Inference here, as elsewhere, must always be qualified, and no model may be assumed to be the best, only more or less credibly better than another. Our approach leaves a great deal of room for further optimization it is the task of future studies to explore. But if the complexity of the brain, in both health and disease, is now undeniable, so ought to be the direction in which prescriptive models must evolve to deliver personalized, equitable care.

# Methods

## Patient population

Patients attending the University College London Hospitals NHS Foundation Trust hyperacute stroke service undergo diffusion weighted imaging (DWI) within 24 hours of presentation where feasible as part of the clinical routine. We used irrevocably anonymized magnetic resonance imaging data from unselected patients with an admission diagnosis—both clinical and radiological—of acute ischaemic stroke. This dataset comprises 4 119 irrevocably anonymized diffusion-weighted magnetic resonance images from 2 830 unique patients. Where multiple images per patient were available, only those  $\geq 30$  days apart were used, ensuring—given the duration of DWI positivity<sup>51</sup>—that each image represented a new lesion. Nonetheless, train/test splits never included data from the same patient in both compartments. Supplementary S3 shows a CONSORT-2010 flow chart of the recruitment. The age and sex distributions are shown in Supplementary S8. Note that only the anatomical lesion architecture, as captured by segmented DWI, is studied here, for our concern is solely with the marginal value of modelling lesion anatomy with high-dimensional methods. Equally, beyond basic demographics, no other characteristics, including observed outcomes, were either collected or modelled, for we are concerned with modelling counterfactual, unobserved outcomes given hypothetical, yet to be identified, interventions. A proportion of the data reported here have been used in previous studies<sup>14–16,37,52</sup>.

## Image processing & lesion segmentation

A U-Net transformer model (UNETR)<sup>53</sup>, a variation of the convolutional neural network U-Net tailored for volume segmentation, was used to segment each lesion from each DWI. The architecture comprises a stack of transformers as the encoder, connected to the decoder through skip connections. The training dataset contained 1 803 DWI with a  $b$ -value of 1 000 for the high contrast between acute stroke lesions and the surrounding brain tissues. From this dataset, 1 256 images comprised a group for manual validation, a subset documented in the published study by Mah et al<sup>15</sup> and 547 images were segmented using a simpler U-Net model and then manually corrected by a neurologist (PN) experienced in the task. All images were first registered to MNI space on a  $91 \times 109 \times 91$  grid of  $2 \text{ mm}^3$  voxels, using non-linear registration computed from the  $b$ -value = 0 images and applied to the  $b$ -value = 1 000 images<sup>52</sup>. Five UNETR models were trained, each time using a different division of the dataset into a training set (80% of the data) and a validation set (20%), from which the model showing the highest performance was selected for further use. Both the Dice similarity coefficient and binary cross-entropy were used to train the model, as the former alone is too stringent given the quantity of noise in clinical imaging, improving capacity for generalization to unseen data. The Dice similarity coefficient alone was used to evaluate the performance on the validation set.

All images presented to the model were padded to fit the model size and the intensities were normalized to between 0 and 1. 3 CoordConv<sup>54</sup> channels were added: 3 arrays of equal size to the images containing the increasing  $x$ ,  $y$  and  $z$  coordinates, providing the model with voxel locations, with the intention to reduce the risk of false positives due to artefacts. A set of augmentation functions were used to improve the generalization of the model further. These functions, randomly applied, included shifting the intensity of the voxels, applying minor affine and elastic transformations, and flipping the image in the sagittal plane.

## Disconnectome representation

Since ischaemic lesions do not substantially discriminate between tissue classes, the impact on grey matter-based functional parcellations is ideally quantified not only by grey matter damage but also by the grey matter disconnections white matter damage incurs. For each lesion in this dataset ( $N = 4 119$ ), a disconnectome representation was therefore generated, providing a probabilistic distribution of affected tissue, including grey matter, resulting from the focal ischaemia.

We employed the Disconnectome Map method from BCBtoolkit to achieve this<sup>36</sup>. Since individual-level white matter connectivity is not available at the necessary data scale, and the long acquisition times it requires would either render it infeasible in the acute setting or liable to introduce strong biases against scanning-intolerant patients, here in conformity with established practice<sup>55,56</sup> we used a reference dataset of healthy participants' tractographies. For each

lesion mask, segmented as described, the white matter fibres passing through the lesion were tracked for each of 178 healthy tractographies<sup>37</sup>, computed from the Human Connectome Project 7T diffusion imaging dataset<sup>57</sup>. 178 binary disconnection masks were obtained, from which averaging was performed to create a probabilistic disconnectome map for each patient. This map shows, for each voxel, the probability of having disconnected white matter fibres passing through it, according to the healthy population dataset. In other words, each voxel's intensity describes the proportion of healthy participants where a white matter connection exists between this voxel and the lesion. The disconnectome maps provide the means to estimate disrupted connections, while taking into account interindividual variability across the population.

### **Compressed data-driven lesion representations**

Image volumes, whether lesion masks or disconnectomes, contain many redundant variables arising from the characteristic distribution of ischaemic damage. Redundancy harms computational efficiency and model stability. Creating compressed, concise representations shorn of redundancy furthermore allows explicit control over the richness of the lesion representation, allowing us to quantify the value of its descriptive detail. Since the optimal method of representational compression for this data is unknown, here we employed an array, including principal component analysis (PCA)<sup>45</sup>, non-negative matrix factorization (NMF)<sup>44</sup>, and volume deep auto-encoders (standard (AE) and variational (VAE))<sup>43</sup>, and independently evaluated downstream models employing each method. The use of a VAE was motivated by the potential value of modelling the representation with the greater structure of a probability distribution with a standard normal prior.

The dataset of images from unique individuals in the dataset,  $N = 2\,830$ , was first divided into a series of 10 train-test splits of 9:1 ratio; in a K-fold cross-validation approach, meaning that all images were assigned once to a test set, in a random manner. The remaining images, each  $\geq 30$  days distinct from all other images from the same individual, were then randomly distributed across the 10 training sets only. This division, before any modelling, ensures that the representational methods do not allow a 'leak' of information that could affect the prescriptive methods; as the test set is held-out for the entirety of the fitting process, from representation on. Therefore, the representational methods were fitted to the training set the applied jointly to both the same training set and the corresponding test set. Across all compression methods, latent embedding lengths of [2, 5, 10, 15, 20, 25, 30, 35, 40, 45, 50] were used.

#### *Principal component analysis*

PCA has the attraction of a closed form solution, but is limited to capturing linear relations. The principal components are visualized in Supplementary S4.2 for ischaemic mask lesion archetypes and S5.2 for disconnectome archetypes, by this method. The standard implementation from SciKit-Learn<sup>58</sup> with default parameters was used for this approach.

#### *Non-negative matrix factorization*

The use of NMF in this setting is now well established<sup>14</sup>. The Nimfa library<sup>59</sup>, with 'random vcol' initialization was used, with archetypal visualizations available in Supplementary S4.1 for lesion archetypes and S5.1 for disconnectome archetypes.

#### *Deep auto-encoders*

The AE's encoder was composed of four layers of three-dimensional ResNet-type convolution blocks, followed by fully connected layers yielding the embedding. Its decoder used the same architecture, in reverse. The VAE used this architecture except the encoder produces the mean and standard deviation of the  $m$ -dimensional posterior latent distribution, from which samples were drawn with the reparameterization trick<sup>43</sup>. At least 16 epochs over the full training set were applied, with a maximum of 32. Between this, if the loss has not improved for 4 consecutive full training set epochs, an early stopping criterion was triggered. A batch size of 10 was used, owing to computational resource constraints.

## Atlas-based lesion representations

To quantify the value of the foregoing rich lesion representations, we created a set of baseline representations based on simple vascular territories of the kind commonly used in stroke studies<sup>60</sup>. Atlases mapping vascular territories by Liu et al<sup>46</sup>, with varying levels of arterial tree specificity, are freely available and suitable for this task. The simplest consisted of expansive territories indexing whether the tissue located by the voxel is supplied broadly by the anterior or posterior arterial systems<sup>61</sup>. To model this, the identity of the disrupted vascular origin was inferred by computing the Dice similarity coefficients between the affected spatial distributions and the vascular territories, with the maximum indexed as a categorical feature. This feature can then be used as a baseline representation for the prescriptive model, for comparison with our richer representations.

Liu et al<sup>46</sup> also offer an atlas for the territories supplied by specific major arteries: anterior cerebral artery, middle cerebral artery, posterior cerebral artery and vertebrobasilar artery. By computing Dice similarity coefficients between the affected distribution and each of these separately lateralized territories, the maximum inferred the identity of the occluded artery, which was applied as a one-hot-encoded feature vector. This vector provides a further baseline representation than the anterior/posterior vascular supply.

## Functional deficit modelling

To evaluate hypothetical prescription across the varied range of clinical presentations associated with ischaemic stroke, a functional parcellation was sought, enabling empirically informed imputation of a deficit across functional archetypes from the spatial distribution of tissue damage. This was derived by agglomerative clustering of open source meta-analytic data from the neurological and neuroscientific literature, compiled by NeuroQuery<sup>30</sup>, as visualized in Figure 4. The process is outlined below.

### *Functional parcellation*

The NeuroQuery dataset<sup>30</sup> consists of predicted neural activation maps, where the intensity of each voxel describes the  $Z$ -value for the association with a specific  $n$ -gram drawn from a large corpus of neuroscientific papers reporting imaging results in MNI space. Each image volume comprised  $46 \times 55 \times 46$  voxels at  $4 \text{ mm}^3$  resolution in MNI space. Volumes associated with  $n$ -grams that could not be plausibly associated with cognitive and behavioural functions were manually excluded, leaving 2095  $n$ -grams for analysis. A grey matter mask was generated by thresholding the tissue probability map<sup>62</sup>, selecting voxels where  $\mathbb{P}(\text{grey matter}) > 0.2$ . To match the template space of the functional data, this mask was spatially resampled from  $121 \times 145 \times 121$  voxels at  $1.5 \text{ mm}^3$  to  $46 \times 55 \times 46$  voxels at  $4 \text{ mm}^3$ , leaving 21410 voxels. Grey matter was selected to isolate neural substrates plausibly associated with functional deficits when lesioned. Lesioned white matter, mediating connectivity, is handled downstream using disconnectome analysis to infer probabilistic estimates of additional disrupted functional tissue resulting from each lesion<sup>37</sup>. The grey matter voxels from the selected functional  $Z$ -distributed volumes were reshaped into a  $2095 \times 21410$  matrix, where each column represented a grey matter voxel, and each row quantified the functional association with each of the neuroscientific terms, localized to the column-indexed voxel.

This matrix was reorganized into clusters with a voxel-based agglomerative approach<sup>63</sup>, where the associative distance reflected functional dissimilarity between the grey matter voxels. Agglomeration of voxels was then performed by adjusting the critical distance threshold, forming clusters of voxels according to their functional similarity (Figure 4), without consideration of spatial relations. A custom program was developed for rapid post-hoc manipulation of the distance threshold. Voxels from discrete connected components of volumes  $< 4^3$  voxels were reclassified using  $K$ -nearest neighbours ( $K = 5$ ) to mitigate the risks of potential low-effect size artefacts resulting from underlying noise. The voxels assigned to each functional network underwent reconstruction to template space via the grey matter mask back to a binary mask of  $46 \times 55 \times 46$  voxels at  $4 \text{ mm}^3$ . Combining these discrete network masks formed the functional parcellation. Figure 4 shows a visualization of the functional parcellation at each level of the hierarchy. Supplementary S1 shows further visualizations of this 16-group functional parcellation, which will also be made available in Neuroimaging Informatics Technology Initiative (NIfTI) format.

Recovery of functional n-grams associated with each functional network is then achieved by taking each network from the functional parcellation individually and computing similarity metrics with the  $Z$ -distributed NeuroQuery data of its origin<sup>30</sup>. The dot-products were listed in order, giving a ranking of functional similarity for each network. The 16-group parcellation revealed functional networks with n-grams clearly falling within a distinct functional theme, in accordance with expectations. The 10 n-grams most closely associated with each component of this parcellation are shown in Supplementary S2, from which the coherent functional themes were manually drawn.

## Ground truth modelling

A perfect evaluation of prescriptive inference demands a counterfactually complete ground truth: observation of the distribution of unobserved responses to all available treatments for all individuals. Since this is impossible<sup>24,33</sup>—a disease event located in time cannot be treated twice—we are obliged to create a semi-synthetic ground truth that combines patient data with empirically informed hypothetical patterns of treatment susceptibility. Given this synthetic ground truth, random or non-random treatment allocation and observational outcomes can be simulated, from which prescriptive models can be fitted to infer which treatment yields the highest probability of causing a subsequent successful outcome in the same individual, and evaluated against the ground truth where this information is available.

For each network in the 16-group functional parcellation, a further subdivision is established for modelling biologically plausible targets of two different hypothetical treatments. These subnetworks were informed by independent physiological data: neurotransmitter receptor<sup>32</sup> or genetic transcriptome<sup>31</sup> anatomical distributions, spanning all regions for which meta-analytic data is available. Note we are concerned with replicating the plausible anatomical structure of treatment targets, rather than their molecular identity, for we are here evaluating hypothetical treatments consistent in their selectivity, not any specific therapeutic agent. The modelling of treatment targets in this manner allows us to synthesize a ground truth, where each individual's susceptibility to a hypothetical treatment can be determined by the overlap of these subnetworks with the lesion anatomy. For each lesion representation, and each functional network, a virtual lesion is thus obtained, establishing a functional deficit and a treatment susceptibility profile specific to the functional network. From each susceptibility-determining subnetwork, the voxel-wise dot-product with each lesion representation was computed. If this measure of overlap exceeded 5% of the volume of each subnetwork (considered within the ranges of critical damage thresholds by Mah et al<sup>15</sup>), the lesion was designated as susceptible to the corresponding treatment. The disconnectome representations were binarized at 0.5, and processed identically. This provided sufficient and diverse sample sizes across the 16 functional networks, with both lesion masks or disconnectomes, and susceptibility informed by meta-analytic neurotransmitter receptor or genetic transcription distributions. The tables describing the sample sizes, separability and overlap are available in Supplementary S6.

### *Neurotransmitter receptome*

A large-scale analysis for neurotransmitter organization within the human neocortex was performed by Hansen et al<sup>32</sup>, for the establishment of a receptor-based atlas. Positron emission tomography (PET) data were collected from >1 200 healthy individuals, with tracers targeting 19 neurotransmitter receptors, across 9 systems: 5-hydroxytryptamine (5HT), dopamine, noradrenaline, histamine, acetylcholine (ACh), cannabinoid, opioid, glutamate and  $\gamma$ -aminobutyric acid (GABA). The group-averaged PET images for each of the 19 neurotransmitter receptors were available from Hansen et al<sup>32</sup>.

To determine the preponderance of the receptor distributions within each functional network, we computed the Dice similarity coefficient between a binarized map of each network and the  $Z$ -transformed group-averaged PET image for each receptor. This was performed at both the level of the specific receptor subtypes, and at the level of the neurotransmitter system. From the two most preponderant receptor types (Supplementary S9) in each functional network, voxel-based classification according to the receptor type with the greatest  $Z$ -score was performed to generate contrasting subnetwork pairs that could describe plausible heterogeneous treatment targets.

### *Genetic transcriptome*

The Allen Institute provides microarray ribonucleic acid (RNA) data with an “all genes, all structures” approach, sampled across six cadaveric adult control brains<sup>31</sup>. Aggregating these data yielded 3 702 samples, across 58 691 genes

per sample. The spatial origin of each sample was supplied in MNI co-ordinates, aligned with the template space of our functional parcellation.

Iterating across the functional networks, samples located within each network mask were selected. These data points were then agglomeratively clustered into two groups according to their microarray RNA data<sup>63</sup>, providing support for a subdivision into molecular profiles based on similarity. Since the microarray data do not cover every grey matter voxel in the brain, unsampled voxels were imputed using Gaussian smoothing in three dimensions, guided by the voxels where gene expression data were present. The magnitude of each Gaussian distribution remained at 1, however the standard deviation was chosen in an automated manner, between 0.25 and 5, to optimize for balance between groups (20% weighting), and for minimizing the number of discrete connected components within subdivisions (40% weighting each, respectively). The functional subnetworks acquired from this method are visualized in Supplementary S10. Note the fidelity of this imputation process is not critical: the objective here is to derive plausible spatial distributions of susceptibility as far as available data allows.

### *Treatment response heterogeneity*

The preceding steps yielded an array of functional networks spanning the entire brain, with two sets of physiological subdivisions each defining plausible patterns of heterogeneous treatment susceptibility. Lesions surpassing the threshold for more than one subnetwork were included, but some classification metrics, such as balanced accuracy, excluded them to avoid inflating the baseline of fidelity (since there is no 'wrong answer' where the individual is susceptible to both treatments). Metrics such as precision-in-estimation-of-heterogeneous-effects, PEHE<sup>28</sup>, include these lesions, penalizing the model for inferring superiority where the two treatments are equivalent.

The above-described methods allow for modelling of heterogeneous responses to treatment within cohorts of individuals presenting with observable functional deficits. It is then the task of the prescription model, evaluated on held-out test data, to infer the causal relation between the deficit, the lesion, and susceptibility to treatment, using observational data corrupted by non-random treatment allocation and interventional noise.

### *Modelling treatment allocation*

Treatment effect estimation is susceptible to biases in the data. RCTs mitigate treatment allocation bias by reducing the risk of treatment-related confounding. For example, if a patient is more likely to receive a treatment in the context of severe disease associated with worse outcomes, a naïve comparison against those who do not receive the treatment will be contaminated by the confounding effects of disease severity. Observational data is especially susceptible to this, as treatments are typically guided by prior beliefs about their efficacy in a specific patient. We must therefore evaluate the impact of such bias in our simulation framework, so that its effect on prescriptive inference can be estimated and compared with performance when using randomized data, and compared with other effects on prescriptive fidelity such as the expressivity of the lesion representation.

All patients presenting with hypothetical deficits (within the above-described 16 functional networks) were recruited to virtual trials, where they received one of two hypothetical treatments, A or B. Both treatments are modelled with non-zero average treatment effects (ATE) for the affected functional network (e.g. language), but with heterogeneous treatment susceptibility, since each hypothetical treatment targets a subdivision of the network, defined by the physiological profiles.

Treatment allocation bias may be observable or unobservable: we need to consider the impact of each.

### *Observable bias*

We used lesion location to simulate this type of treatment allocation bias, given that the treatment targets were also distributed anatomically. The bias was simulated with a single parameter in the ground truth synthetic process, ranging from 0 (randomized to treatment) to 1 (deterministic treatment allocation based on lesion location). This quantifies bias towards receipt of a given intervention.

For each pair of the susceptibility-determining subnetworks, the three-dimensional centroid of each region was computed, as  $\text{argmax}(|c_{x,A} - c_{x,B}|, |c_{y,A} - c_{y,B}|, |c_{z,A} - c_{z,B}|)$ , where  $c_{a,t}$  is each centroid, axis  $a$ , target for

intervention  $t$ , revealing the axis ( $x$ ,  $y$  or  $z$ ) of greatest variation in true treatment response. To maximize the potential for bias, this axis was chosen in the bias allocation process, individually for each pair of subnetworks.

The probability of individual  $i$  being allocated treatment A or B, was modelled using vector  $\rho$ , where biased allocation was intended. The parameter of treatment allocation bias is given by  $b_{\text{obs}}$  ( $b_{\text{obs}} \in [0, 1]$ ). If  $b_{\text{obs}} = 0$ , each patient has an equal probability of allocation to each treatment group, effectively simulating a RCT. If  $b_{\text{obs}} = 1$ , treatment allocation is deterministic, resulting directly from whether each lesion representation within the training set exists above or below the median in the axis of greatest variance by centroid co-ordinates.

Where  $0 < b_{\text{obs}} < 1$ , the bias parameter is used to define the probabilities for allocating each patient to each treatment across a set of Monte Carlo simulations. The specific propensity for each patient is determined according to the order within the training set of the lesion representation centroid location within the axis of maximal variance. For  $0 < b_{\text{obs}} < 0.5$ , the vector of propensities in this ordered list is set by  $\rho = \text{linspace}(0.5 - b_{\text{obs}}, 0.5 + b_{\text{obs}}, N)$ , with  $N$  being the number of participants in the training cohort. The allocation is then simulated using Monte Carlo methods, sampling from a non-uniform probability distribution.

For  $0.5 < b_{\text{obs}} < 1$ , the extremes of the ordered data have fixed allocation with certainty to either treatment, depending on their relation to the training set median. These patients are allocated to the group for which the treatment is targeted to the region in the same direction along the axis of maximal variance. The degree of  $b_{\text{obs}}$  beyond 0.5 to 1 reflects the size of these tails (balanced at the extremes) where allocation is certain. In the middle section, all patients have propensity allocated in order, as if  $b_{\text{obs}} = 0.5$ .

#### *Unobservable bias*

To model the scenario where allocation to treatment is influenced by unobservable factors not captured in the lesion representation, another approach to modelling this bias was separately implemented. This approach 'leaks' information to the treatment allocation process determined by the true treatment susceptibility distribution. An analogous bias parameter,  $b_{\text{un_obs}}$  was used to model the extent to which treatment allocation is influenced by these unobservable confounders. This was implemented using Monte Carlo modelling, where  $\mathbb{P}(W = w^*) = b_{\text{un_obs}}$ , where  $w^*$  is a treatment that the individual is truly susceptible to, according to the ground truth synthetic process, hidden from the prescriptive training data.

#### *Interventional noise*

The causal inference literature distinguishes the recipients of interventions as doomed, causal, preventive and immune<sup>64</sup>. Treatment effects were simulated to mimic the possibility that some patients are 'doomed' not to respond to an individually optimal treatment; recovery effects were simulated to model that some patients (dubbed 'immune') may observably respond spontaneously, regardless of the treatment received, even if it was individually suboptimal. These effects are manipulated by probabilistic hyperparameters to the observational data synthetic pipeline.

#### *Fixed treatment effects*

The fixed treatment effect (TE) is applied to reflect for the probability that each individual displays an observable response, given that they received their truly individually optimal intervention. Therefore  $\text{TE} < 1$  results in some patients not responding to treatment, despite optimal treatment selection.

#### *Fixed recovery effects*

The fixed recovery effect (RE) reflects the probability that an individual is 'immune', such that they would display an observable response, irrespective of the treatment received (or spontaneous recovery). Therefore, if  $\text{RE} > 0$ , some patients will observably respond, even if the treatment received was not optimal.

These probabilistic approaches are the foundations for the Monte Carlo simulations used to synthesize observational outcomes. A synthetic ground truth with  $\text{TE} = 1$  and  $\text{RE} = 0$  would therefore have no added response noise, with all patients responding according to whether their stroke phenotype is truly susceptible to the intervention that they were allocated to receive.

## Prescriptive inference

### *Problem setup*

With the semi-synthetic ground truth established, we are presented with data consisting of a phenotypic characterization—a representation of the lesion—the allocated treatment, and the outcome. We employ notation consistent with the causal inference literature<sup>27,65</sup>. For each individual  $i$ , the representation of the patient and pathology is denoted  $\mathbf{X}_i$ , the treatment received  $W_i$ , and the observed outcome  $Y_i$ . This therefore constitutes a modelled observational dataset,  $\mathcal{D} = \{\mathbf{X}_i, W_i, Y_i\}_i^n$ . Each are assumed to be i.i.d. from some distribution  $\mathbb{P}(\mathbf{X}, W, Y)$ . For each individual, only one potential outcome can be observed,  $Y_i$ , dependent on which treatment was received by patient  $i$ . If treatment A is received, this would be  $Y_i^{(A)}$ ; if treatment B then  $Y_i^{(B)}$ . The individual treatment effect:  $Y_i^{(A)} - Y_i^{(B)}$  therefore cannot be evaluated empirically; it is this difference from which the true optimal treatment,  $w_i^*$ , is inferred. The inference of individual treatment effects,  $\tau_i$ , is bounded by a set of assumptions, under which  $\tau_i = Y_i^{(A)} - Y_i^{(B)}$  can be validly approximated by  $\hat{\tau}(\mathbf{x}) = \mathbb{P}(Y = 1 | W = A, \mathbf{X} = \mathbf{x}) - \mathbb{P}(Y = 1 | W = B, \mathbf{X} = \mathbf{x})$ , where  $Y = 1$  describes a favourable response to treatment. The assumptions are: that the interventions are sufficiently well-defined (consistency), that the allocation to treatment depends only on observed covariates (conditional exchangeability), and that the probability of receiving each available treatment is non-zero across all individuals (overlap)<sup>35,66</sup>.

### *Assumptions*

If the assumptions of consistency, conditional exchangeability, and overlap are all valid, causal interpretation is deemed *identifiable*.

*Consistency* denotes that the intervention is sufficiently well defined, and the observed outcome is truly the outcome following receipt of treatment. This implies that for an individual allocated treatment A:  $W_i = A$ , the observed outcome will follow such that  $Y_i = Y_i^{(A)}$ . It also implies that the treatment, as defined, is applied in the same manner across the population allocated to receive it (e.g. the same dose and route of drug administration). In some of the causal modelling literature, an assumption of stable unit treatment value assumption, or SUTVA, is stated, conveying the same condition. This further makes explicit the underlying assumption of independence between units: that one individual's receipt of a treatment has no effect on another individual's treatment allocation, also encapsulating the concept of no variation within defined treatments.

*Conditional exchangeability*, denotes the absence of unobserved confounders (sometimes independently described as *unconfoundedness*). Here, the characteristics between the treatment groups should be similarly distributed, or capable of being thereby modelled with the available variables. Violations of this assumption is what RCTs seek to address. The assumption of [strongly] ignorable treatment allocation—an alternative formulation—conveys the same idea: that outcomes are independent of treatment allocation, when conditioned on the captured observable characteristics, which can be presented symbolically as  $(Y^{(A)}, Y^{(B)}) \perp W | \mathbf{X}$ . *Strong* ignorability should also convey that the probability of allocation to treatment is always non-zero, which is often explicitly stated as a separate assumption of *positivity*, or *overlap*.

*Positivity, or overlap*, denotes that before allocation to treatment of each individual in the data, there is a possibility that they could be allocated to any treatment from those available:  $0 < \mathbb{P}(W = w | \mathbf{X} = \mathbf{x}) < 1$  for all  $w, \mathbf{x}$ . If treatment allocation is already pre-determined, the causal implications of receiving the treatment cannot be recovered from the data.

This simulation analysis, while empirically driven, employing modelled ground truths, seeks to investigate the fidelity of prescription when these assumptions are controllably weakened. By manipulating fixed treatment and recovery effects, the assumptions of consistency are weakened, while also modelling the unavoidable resultant noise that exists in all healthcare data. Modelling treatment allocation bias by location investigates the effect of stressing conditional exchangeability, and modelling unobservable treatment allocation bias tests its violation. At the extreme of this modelled treatment allocation bias, the assumption of positivity/overlap is weakened, where some individuals are inclined very strongly to be allocated to one treatment over another (or when  $b = 1$ , it becomes deterministic).

Testing the fidelity of prescriptive performance under all conditions was by design: it is not a limitation, but deliberate, systematic evaluation of circumstances where the benefits of high-dimensional modelling from observational data may be able to overcome the limitations of non-random trial design, compared with using traditional covariates within an RCT framework.

### *Prescriptive configurations*

Fitting models capable of individual treatment effect—and therefore prescriptive—inference, here is based on two relatively simple configurations, in keeping with established practice<sup>27,65,67,68</sup>.

The *one-model* approach adds an additional feature to the representation of each case indicating the received treatment. A classifier is then fitted, using this combined representation and treatment input, to predict outcome. For unseen individuals, this additional feature can be set to each available treatment, and the same model can then provide an estimation of the probability of success of each treatment, which can then be used for individualized treatment effect (ITE) and prescriptive inference.

The *two-model* approach employs two separate classifiers, each fitted independently on data relating to individuals allocated to each treatment, to predict outcome. For unseen individuals, each model predicts the probability of success of its respective treatment, selecting the highest probability to derive the ITE and deliver prescriptive inference.

### *Models*

An array of well-established estimators were implemented within these prescriptive configurations for this evaluation, primarily default parameterizations of extremely randomized trees<sup>38</sup>, random forest<sup>40</sup>, Gaussian process<sup>41</sup> and logistic regression<sup>42</sup> from the SciKit-Learn Python package<sup>58</sup>, and XGBoost classifiers<sup>39</sup>. We used a wide array of model architectures to provide assurance of generalizability across architectural approaches.

### *Model evaluation*

The fidelity of prescription was assessed by prescriptive balanced accuracy and observed PEHE. The presented evaluation always relates to performance averaged over the test sets of the overarching 10-fold cross-validation, established before the representational modelling and maintained throughout.

**PRESCRIPTIVE BALANCED ACCURACY.** Prescriptive balanced accuracy excludes all individuals who were (in the ground truth) modelled to be truly susceptible to both treatments: any method of treatment allocation in these individuals would be correct and therefore artificially inflate the classification metrics. From the remaining individuals, where there is a hierarchy of treatment selection, the proportion of those correctly allocated from those modelled to be susceptible to each treatment are computed, and the mean of these proportions forms the final measure of prescriptive performance.

**OBSERVED PRECISION IN ESTIMATION OF HETEROGENEOUS EFFECTS.** Observed PEHE uses all the data, since the probabilistic predictions are used, to evaluate whether the model is sufficiently capable of inferring where individuals are susceptible to both treatments, instead of falsely inferring a hierarchy. The performance measure is then computed accordingly as the root-mean-square-error of estimating the individualized treatment effects,  $\sqrt{\frac{1}{N_{test}} \sum_{i=1}^{N_{test}} (\hat{\tau}_i - \tau_i)^2}$ , in this situation where a lower value indicates superior performance.

**COMPARING PERFORMANCE MEASURES.** While much of the heterogeneous treatment effect inference literature uses PEHE; we argue that here a classification metric would be more suitable. Balanced accuracy was selected for its quality of not misleadingly diminishing the influence of minorities where treatment susceptibility is imbalanced, and was preferred over PEHE for prioritizing proportion of individuals inferred to the most suitable treatment rather than the precision of inference; the influence over the measure is distributed uniformly across all individuals susceptible to each treatment.

**COMPARISON.** The question we seek to answer is whether, and if so under which conditions, complex modelling of observational data mitigates the risks of non-randomization in comparison with traditional inferential approaches using RCTs, for heterogeneous conditions such as ischaemic stroke, based on empirical data. We therefore used affected vascular territories arising from the broad anterior or posterior arterial systems as a simple, low-dimensional baseline, as this is already reflected in the UK clinical guidance as a factor influencing the decision between the acute ischaemic

stroke treatments of mechanical thrombectomy or intravenous thrombolysis<sup>60</sup>. Performance comparisons therefore contrasted the use of high-dimensional representations, using observational data modelled with specific allocation bias values as described, with the unbiased allocation (RCT surrogate) performance of this anterior/posterior vascular supply model; at the same respective treatment effect/recovery effect pairs, since randomization does not control for these features of interventions. Prescriptive performance relating to ischaemic lesion mask and disconnectome representations and functional deficits are presented using their aggregate mean and compared using independent sample two-sided *t*-tests across each of these; with superiority determined by exceeding the critical *p*-value as determined by the Benjamini-Hochberg method<sup>69</sup>, with the family-wise error rate reflecting 0.05 significance level.

#### **Data availability**

Functional grey matter parcellations including their subdivided versions will be made available after publication. Neuroimaging data cannot be released publicly owing to the terms of access to clinical data specified in the ethical approval.

#### **Code availability**

Will be made available after publication.

## References

1. Deaton, A. & Cartwright, N. Understanding and misunderstanding randomized controlled trials. *Social Science & Medicine* vol. 210 2–21 (2018).
2. Mulder, R. *et al.* The limitations of using randomised controlled trials as a basis for developing treatment guidelines. *Evid. Based Ment. Health* **21**, 4–6 (2018).
3. Rothwell, P. M. Subgroup analysis in randomised controlled trials: importance, indications, and interpretation. *The Lancet* **365**, 176–186 (2005).
4. Wardlaw, J. & Warlow, C. Thrombolysis in acute ischemic stroke: does it work? *Stroke* **23**, 1826–1839 (1992).
5. Rothwell, P. M. External validity of randomised controlled trials: “to whom do the results of this trial apply?” *The Lancet* **365**, 82–93 (2005).
6. Sackett, D. L., Rosenberg, W. M., Gray, J. M., Haynes, R. B. & Richardson, W. S. Evidence based medicine: what it is and what it isn't. *Bmj* vol. 312 71–72 (1996).
7. Feigin, V. L. *et al.* Global, regional, and national burden of stroke and its risk factors, 1990–2019: a systematic analysis for the Global Burden of Disease Study 2019. *Lancet Neurol.* **20**, 795–820 (2021).
8. Vos, T. *et al.* Global burden of 369 diseases and injuries in 204 countries and territories, 1990–2019: a systematic analysis for the Global Burden of Disease Study 2019. *The Lancet* **396**, 1204–1222 (2020).
9. Smith, W. S. *et al.* Mechanical thrombectomy for acute ischemic stroke: final results of the Multi MERCI trial. *Stroke* **39**, 1205–1212 (2008).
10. Wardlaw, J. M., Murray, V., Berge, E. & Del Zoppo, G. J. Thrombolysis for acute ischaemic stroke. *Cochrane Database Syst. Rev.* (2014).
11. Langhorne, P., Bernhardt, J. & Kwakkel, G. Stroke rehabilitation. *The Lancet* **377**, 1693–1702 (2011).
12. Bustamante, A. *et al.* Ischemic stroke outcome: a review of the influence of post-stroke complications within the different scenarios of stroke care. *European journal of internal medicine* vol. 29 9–21 (2016).
13. Haak, K. V. & Beckmann, C. F. Understanding brain organisation in the face of functional heterogeneity and functional multiplicity. *NeuroImage* **220**, 117061 (2020).
14. Bonkhoff, A. K. *et al.* Reclassifying stroke lesion anatomy. *Cortex* **145**, 1–12 (2021).
15. Mah, Y.-H., Husain, M., Rees, G. & Nachev, P. Human brain lesion-deficit inference remapped. *Brain* **137**, 2522–2531 (2014).
16. Xu, T., Jha, A. & Nachev, P. The dimensionalities of lesion-deficit mapping. *Neuropsychologia* vol. 115 134–141 (2018).
17. Xie, Y., Brand, J. E. & Jann, B. Estimating heterogeneous treatment effects with observational data. *Sociol. Methodol.* **42**, 314–347 (2012).
18. Giraudeau, B. *et al.* Heterogeneity in pragmatic randomised trials: sources and management. *BMC Med.* **20**, 1–16 (2022).
19. Kent, D. M., Steyerberg, E. & van Klaveren, D. Personalized evidence based medicine: predictive approaches to heterogeneous treatment effects. *Bmj* **363**, (2018).
20. Holmes, M., Davis, S. & Simpson, E. Alteplase for the treatment of acute ischaemic stroke: a NICE single technology appraisal; an evidence review group perspective. *Pharmacoeconomics* **33**, 225–233 (2015).
21. Montaner, J. *et al.* Multilevel omics for the discovery of biomarkers and therapeutic targets for stroke. *Nat. Rev. Neurol.* **16**, 247–264 (2020).
22. White, P. *et al.* Standards for providing safe acute ischaemic stroke thrombectomy services (September 2015). *Clin. Radiol.* **72**, 175–e1 (2017).
23. Nguyen, T.-L., Collins, G. S., Landais, P. & Le Manach, Y. Counterfactual clinical prediction models could help to infer individualized treatment effects in randomized controlled trials—An illustration with the International Stroke Trial. *J. Clin. Epidemiol.* **125**, 47–56 (2020).
24. Holland, P. W. Statistics and causal inference. *J. Am. Stat. Assoc.* **81**, 945–960 (1986).
25. Alaa, A. & van der Schaar, M. Limits of estimating heterogeneous treatment effects: Guidelines for practical algorithm design. *International Conference on Machine Learning* 129–138 (2018).

26. Alaa, A. & van der Schaar, M. Bayesian inference of individualized treatment effects using multi-task gaussian processes. *Advances in Neural Information Processing Systems* 3424–3432 (2017).
27. Curth, A. & van der Schaar, M. Nonparametric estimation of heterogeneous treatment effects: From theory to learning algorithms. in *International Conference on Artificial Intelligence and Statistics* 1810–1818 (PMLR, 2021).
28. Hill, J. L. Bayesian Nonparametric Modeling for Causal Inference. *Journal of Computational and Graphical Statistics* vol. 20 217–240 (2011).
29. Lu, M., Sadiq, S., Feaster, D. J. & Ishwaran, H. Estimating Individual Treatment Effect in Observational Data Using Random Forest Methods. *Journal of computational and graphical statistics : a joint publication of American Statistical Association, Institute of Mathematical Statistics, Interface Foundation of North America* vol. 27 209–219 (2018).
30. Dockès, J. *et al.* NeuroQuery, comprehensive meta-analysis of human brain mapping. *Elife* **9**, e53385 (2020).
31. Hawrylycz, M. J. *et al.* An anatomically comprehensive atlas of the adult human brain transcriptome. *Nature* **489**, 391–399 (2012).
32. Hansen, J. Y. *et al.* Mapping neurotransmitter systems to the structural and functional organization of the human neocortex. *Nat. Neurosci.* (2022) doi:10.1038/s41593-022-01186-3.
33. Rubin, D. B. Estimating causal effects of treatments in randomized and nonrandomized studies. *Journal of educational Psychology* vol. 66 688 (1974).
34. Pearl, J. *Causality*. (Cambridge university press, 2009).
35. Hernán, M. A. & Robins, J. M. *Causal Inference: What If*. (2020).
36. Foulon, C. *et al.* Advanced lesion symptom mapping analyses and implementation as BCBtoolkit. *Gigascience* **7**, giy004 (2018).
37. Thiebaut de Schotten, M., Foulon, C. & Nachev, P. Brain disconnections link structural connectivity with function and behaviour. *Nat. Commun.* **11**, 5094 (2020).
38. Geurts, P., Ernst, D. & Wehenkel, L. Extremely randomized trees. *Mach. Learn.* **63**, 3–42 (2006).
39. Chen, T. & Guestrin, C. XGBoost: A scalable tree boosting system. in *Proceedings of the 22nd ACM SIGKDD international conference on knowledge discovery and data mining* 785–794 (2016).
40. Breiman, L. Random forests. *Mach. Learn.* **45**, 5–32 (2001).
41. MacKay, D. J. *Information theory, inference and learning algorithms*. (2003).
42. McCullagh, P. *Generalized Linear Models*. (Routledge, 2019).
43. Kingma, D. P. & Welling, M. Auto-encoding variational bayes. *ArXiv Prepr. ArXiv13126114* (2013).
44. Lee, D. D. & Seung, H. S. Learning the parts of objects by non-negative matrix factorization. *Nature* **401**, 788–791 (1999).
45. Jolliffe, I. T. *Principal Component Analysis for Special Types of Data*. (Springer, 2002).
46. Liu, C.-F. *et al.* Digital 3D Brain MRI Arterial Territories Atlas. *Sci. Data* **10**, 1–17 (2023).
47. Cook, D. *et al.* Lessons learned from the fate of AstraZeneca’s drug pipeline: a five-dimensional framework. *Nat. Rev. Drug Discov.* **13**, 419–431 (2014).
48. Bespalov, A. *et al.* Failed trials for central nervous system disorders do not necessarily invalidate preclinical models and drug targets. *Nat. Rev. Drug Discov.* **15**, 516–516 (2016).
49. Kersten, P., Ellis-Hill, C., McPherson, K. M. & Harrington, R. Beyond the RCT—understanding the relationship between interventions, individuals and outcome—the example of neurological rehabilitation. *Disabil. Rehabil.* **32**, 1028–1034 (2010).
50. Carruthers, R. *et al.* Representational ethical model calibration. *Npj Digit. Med.* **5**, 170 (2022).
51. Augustin, M. *et al.* Diffusion-weighted imaging of patients with subacute cerebral ischemia: comparison with conventional and contrast-enhanced MR imaging. *Am. J. Neuroradiol.* **21**, 1596–1602 (2000).
52. Xu, T., Rolf Jäger, H., Husain, M., Rees, G. & Nachev, P. High-dimensional therapeutic inference in the focally damaged human brain. *Brain* **141**, 48–54 (2018).
53. Hatamizadeh, A. *et al.* UNETR: Transformers for 3D Medical Image Segmentation. in *Proceedings of the IEEE/CVF Winter Conference on Applications of Computer Vision* 574–584 (2022).

54. El Jurdi, R., Petitjean, C., Honeine, P. & Abdallah, F. CoordConv-Unet: Investigating CoordConv for Organ Segmentation. *IRBM* **42**, 415–423 (2021).
55. Van Essen, D. C. *et al.* The WU-Minn human connectome project: an overview. *Neuroimage* **80**, 62–79 (2013).
56. Maier-Hein, K. H. *et al.* The challenge of mapping the human connectome based on diffusion tractography. *Nat. Commun.* **8**, 1349 (2017).
57. Vu, A. T. *et al.* High resolution whole brain diffusion imaging at 7 T for the Human Connectome Project. *Neuroimage* **122**, 318–331 (2015).
58. Pedregosa, F. *et al.* Scikit-learn: Machine learning in Python. *the Journal of machine Learning research* vol. 12 2825–2830 (2011).
59. Zitnik, M. & Zupan, B. Nimfa: A Python Library for Nonnegative Matrix Factorization. *J. Mach. Learn. Res.* **13**, 849–853 (2012).
60. National Institute for Health and Care Excellence. Stroke and transient ischaemic attack in over 16s: diagnosis and initial management. (2019).
61. Frid, P. *et al.* Detailed phenotyping of posterior vs. anterior circulation ischemic stroke: a multi-center MRI study. *J. Neurol.* **267**, 649–658 (2020).
62. Blaiotta, C., Cardoso, M. J. & Ashburner, J. Variational inference for medical image segmentation. *Comput. Vis. Image Underst.* **151**, 14–28 (2016).
63. Virtanen, P. *et al.* SciPy 1.0: fundamental algorithms for scientific computing in Python. *Nat. Methods* **17**, 261–272 (2020).
64. Greenland, S. & Robins, J. M. Identifiability, exchangeability, and epidemiological confounding. *Int. J. Epidemiol.* **15**, 413–419 (1986).
65. Künzel, S. R., Sekhon, J. S., Bickel, P. J. & Yu, B. Metalearners for estimating heterogeneous treatment effects using machine learning. *Proc. Natl. Acad. Sci.* **116**, 4156–4165 (2019).
66. Imbens, G. W. & Rubin, D. B. *Causal Inference in Statistics, Social, and Biomedical Sciences*. (Cambridge University Press, 2015).
67. Shalit, U., Johansson, F. D. & Sontag, D. Estimating individual treatment effect: generalization bounds and algorithms. in *International Conference on Machine Learning* 3076–3085 (PMLR, 2017).
68. Johansson, F. D., Shalit, U., Kallus, N. & Sontag, D. Generalization bounds and representation learning for estimation of potential outcomes and causal effects. *J. Mach. Learn. Res.* **23**, 7489–7538 (2022).
69. Benjamini, Y. & Hochberg, Y. Controlling the false discovery rate: a practical and powerful approach to multiple testing. *J. R. Stat. Soc. Ser. B Methodol.* **57**, 289–300 (1995).

## Acknowledgements

Funded by UCLH NIHR Biomedical Research Centre (NIHR-INF-0840) and UKRI EPSRC (2252409). The authors acknowledge the use of the UCL Myriad High Performance Computing Facility (Myriad@UCL), and associated support services, in the completion of this work.

Corresponding authors: Dominic Giles ([dominic.giles@ucl.ac.uk](mailto:dominic.giles@ucl.ac.uk)) and Parashkev Nachev ([p.nachev@ucl.ac.uk](mailto:p.nachev@ucl.ac.uk)).

## Inclusion & Ethics Statement

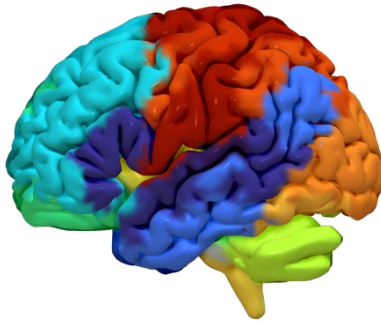
This study was performed under ethical approval by the West London & GTAC research ethics committee for consentless use of fully anonymized data. The data is an unselected sample based on clinical diagnosis of acute ischaemic stroke; no other specific inclusion or exclusion criteria were used. It should therefore be proportionally representative of the acute ischaemic stroke patient population presenting to hospital in London, UK.

## Supplementary Material

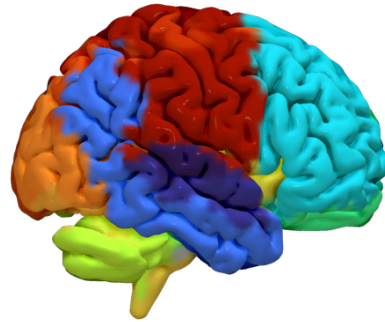
Fig.	Title	Page
S1	Functional parcellation visualisation	1
S2	Ordered list of neurological terms for each functional network	3
S3	CONSORT 2010 flow diagram of dataset curation	4
S4	Lesion archetypes	5
S5	Disconnectome archetypes	7
S6	Separability, overlap, and sample size for each virtual trial	9
S7	Lesion volume distribution	10
S8	Patient age and sex distributions	11
S9	Neurotransmitter receptome subnetworks	12
S10	Transcriptome subnetworks	45
S11	Lesion representations & location bias results	78
S12	Disconnectome representations & location bias results	83
S13	Lesion representations & unobservable bias results	88
S14	Disconnectome representations & unobservable bias results	93
S15	Prescriptive analysis summary by PEHE	98
S16	Prescriptive analysis summary, stratified by deficit, by PEHE	99
S17	Performance comparison under ideal experimental conditions	100

## S1.1: Functional parcellation surface renders

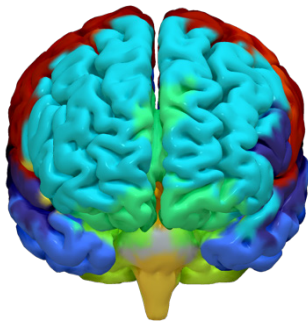
a



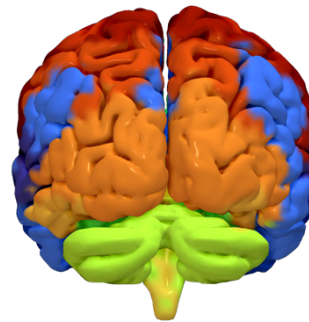
b



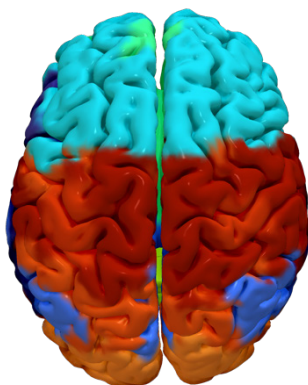
c



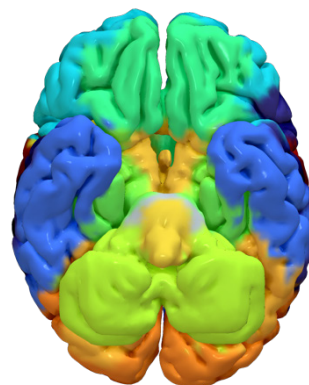
d



e

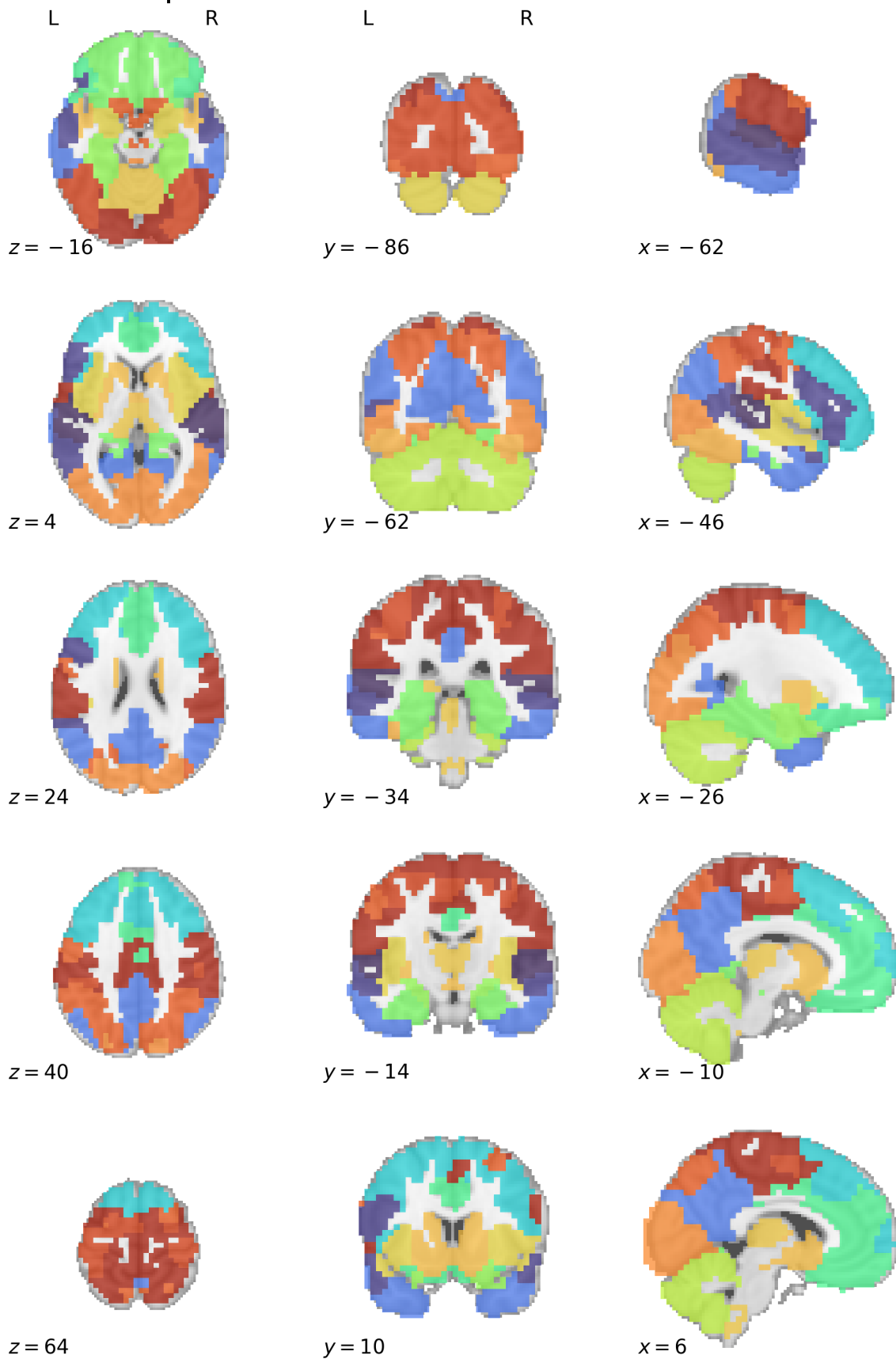


f



Surface rendering of the functional grey matter parcellation, with 16 distinct regions labelled by colour. The same colours are used in Figures 4, S1.2, and S2. The functional categories associated with each region are described in the coloured text of Figures 4, derived from the term lists in Figure S2. Each panel shows the same surface rendering from a different spatial perspective: **a**, left; **b**, right; **c**, anterior; **d**, posterior; **e**, superior; **f**, inferior.

## S1.2: Functional parcellation axial slices



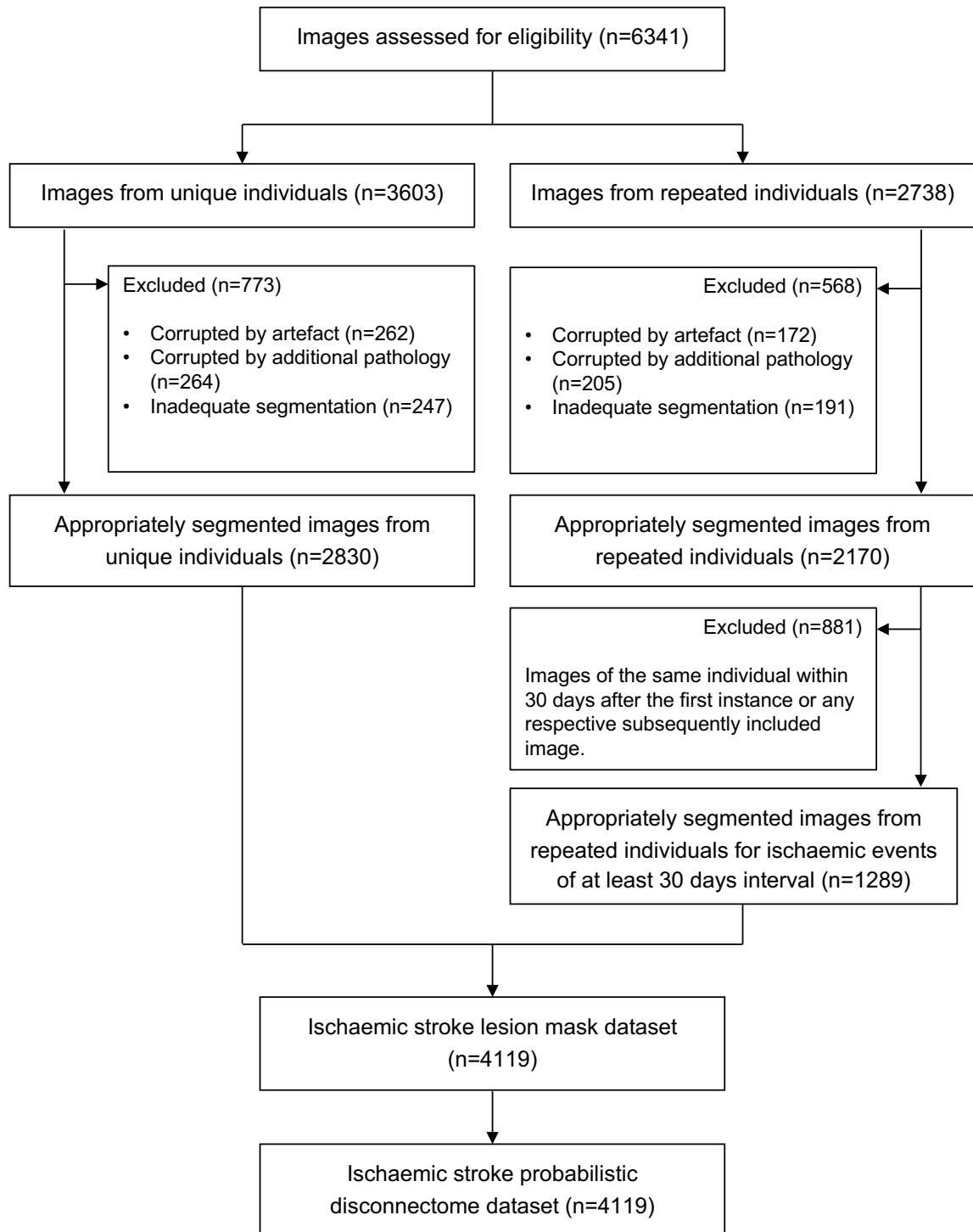
Axial slice visualisation of the functional grey matter parcellation, with 16 distinct regions labelled by colour, overlaid onto the standard MNI152 template. The slice co-ordinates refer to MNI space. The same colours are used in Figures 4, S1.1 and S2. The functional categories associated with each region are described in the coloured text of Figure 4, derived from the term lists in Figure S2.

## S2: Ordered list of neurological terms for each functional network

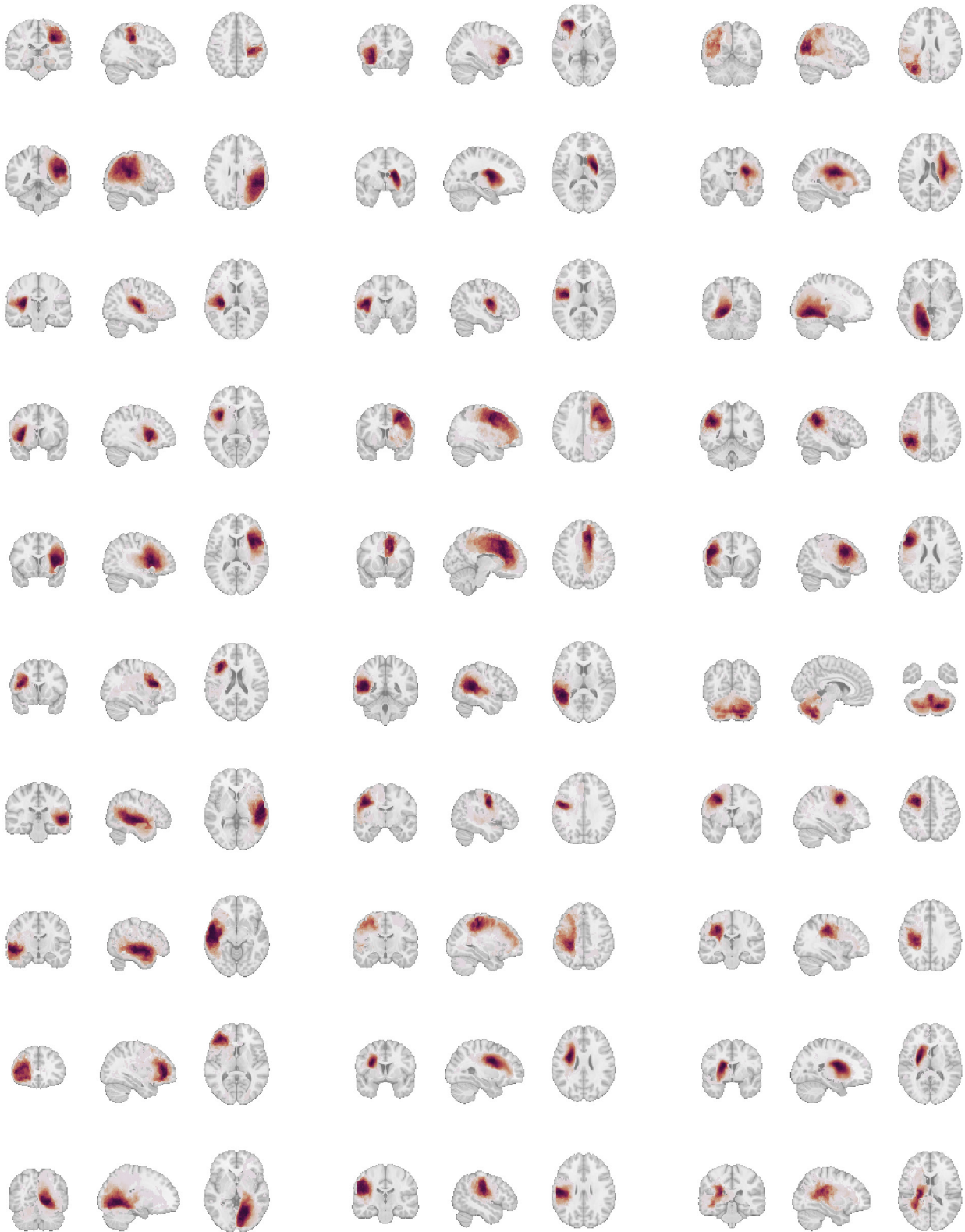
Hearing Auditory feedback Acoustic Auditory perception Acoustic processing Auditory stimuli Auditory stream segregation Vocalisation Hearing loss Melody	Lexical processing Phonological processing Linguistic Story Spoken Auditory sentence comp. Parsing Deafness Lexical Speaker	Self-referential Referential Mind Conscious Rumination Dream Narcissistic Self-control Schizotypal personality dis. Wandering	Sorting Cognitive control Handling Response execution Opiate dependence Primitive Psychological stress Inattentional blindness Reappraisal Punish
Compulsive behaviour Mood Mania Discipline Unipolar depression Reversal learning Suicidability Accountability Hoarding Awakening	Amnesia Novelty detection Active retrieval Spatial memory Spatial navigation Memory loss Navigation Cognitive symptom Encoding Maze	Fearful faces Fearful Temperament Aggressive Emotional stimuli Uninhibited Psychopathic personality Neutral stimuli Bereavement Separation anxiety	Tremor Orthostatic Corneal Dysmetria Incoordination Friedreich ataxia Uvula Gastrocnemius Ataxia Spatial organisation
Feeling Viscerosensory Interoceptive Destructive Hate Shyness Tachycardia Risk processing Gustation Disgust	Cataplexy Slow wave sleep Sleep latency Sleep Slow wave sleep REM sleep Sleep disordered breathing Memory acquisition Circadian rhythm Tiredness	Gratification Negative reinforcement Habit learning Habit Physical anhedonia Love Substance dependence Anhedonia Erotic Instrumental conditioning	Recognition Photographs Facial recognition Visual representation Prejudice Selective Agnosia Viewing Repetition suppression Recognised
Blindness Visual perception Sighted Blind Visual impairment Visual angle Blindsight Ambyopia Form perception Stereoscopic	Calculation Mathematical Visuospatial Mental arithmetic Procedural knowledge Acalculia Cue validity Capacity limitation Arithmetic processing Arithmetic	Flexor Extremity Extensor Finger movements Voluntary Paresis Execution Extension Dressing Isometric	Sensory perception Extremity Count Primary somatosensory Muscle Kinaesthetic Plantar Proprioceptive Embodied Reflex

Ordered lists of the 10 commonest functional labels associated with each grey matter network in the parcellation (as visualized in Figures 4 and S1) by dot product with the original meta-analytic statistical maps from NeuroQuery. The colours are unified with Figure 4 and S1, with the archetypal functional categories manually identified from the above to be: (upper row, left to right) hearing, language, introspection, cognition; (second row, left to right) mood, memory, aversion, co-ordination; (third row, left to right) interoception, sleep, reward, visual recognition and (lower row, left to right) visual perception, spatial reasoning, motor, somatosensory.

### S3: CONSORT 2010 lesion dataset flow chart

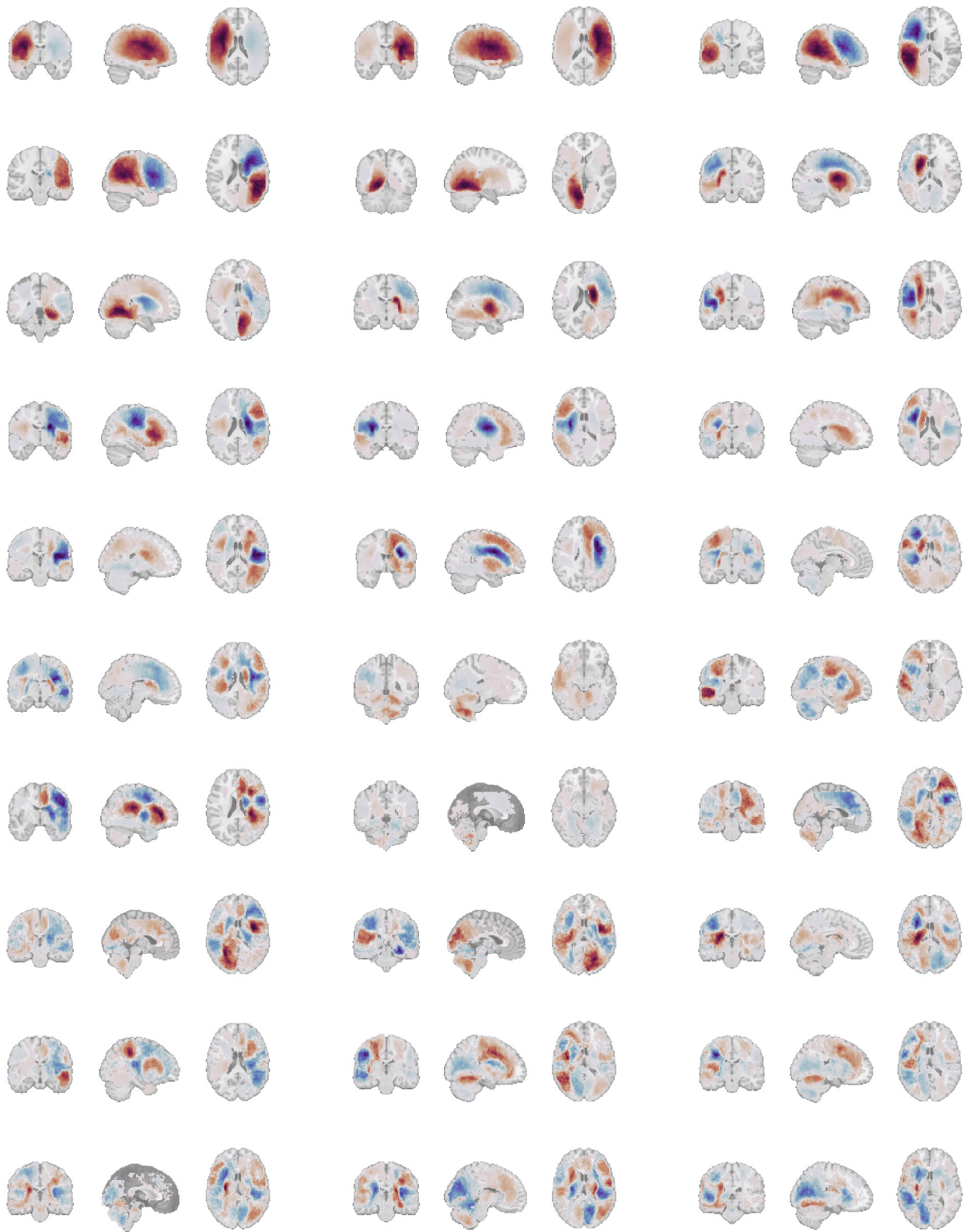


## S4.1: Lesion NMF archetypes



Spatial reconstructions of the latent factors from a 30-dimensional non-negative matrix factorisation of the lesion masks. The spatial distribution of each reconstruction is visualized. Coronal (left), sagittal (centre) and axial (right) slice are shown for each, with co-ordinates set to the location of maximum density.

## S4.2: Lesion PCA archetypes



Spatial reconstructions of the latent factors from a 30-dimensional principal component analysis-derived representation of the lesion masks. The spatial distribution of each reconstruction is visualized. Coronal (left), sagittal (centre) and axial (right) slice are shown for each, with co-ordinates set to the location of maximum density.

## S5.1: Disconnectome NMF archetypes



Spatial reconstructions of the latent factors from a 30-dimensional non-negative matrix factorisation of the disconnectomes. The spatial distribution of each reconstruction is visualized. Coronal (left), sagittal (centre) and axial (right) slice are shown for each, with co-ordinates set to the location of maximum density.

## S5.2: Disconnectome PCA archetypes



Spatial reconstructions of the latent factors from a 30-dimensional principal component analysis-derived representation of the disconnectomes. The spatial distribution of each reconstruction is visualized. Coronal (left), sagittal (centre) and axial (right) slice are shown for each, with co-ordinates set to the location of maximum density.

## S6: Linear separability, overlap, & sample sizes

Lesions, N = 4 119, threshold = 0.05

	Receptome				Transcriptome			
	Linear separability		Overlap	N	Linear separability		Overlap	N
	OR	XOR			OR	XOR		
Hearing	0.618	0.985	0.603	305	0.684	0.949	0.506	322
Language	0.567	NaN	0.463	240	0.991	0.991	0	264
Introspection	0.799	0.857	0.309	94	0.739	0.908	0.291	103
Cognition	0.546	0.500	0.321	196	0.653	0.919	0.548	168
Mood	0.593	0.667	0.516	31	0.938	1	0.194	31
Memory	0.580	0.643	0.779	136	0.593	0.954	0.650	157
Aversion	0.603	0.686	0.341	88	0.695	0.780	0.344	96
Coordination	0.816	0.950	0.413	109	0.648	0.883	0.543	105
Interoception	0.623	0.938	0.669	495	0.577	0.903	0.665	487
Sleep	0.702	0.938	0.337	83	0.722	0.908	0.372	102
Reward	0.694	0.900	0.355	304	0.550	0.667	0.039	356
Visual recognition	0.876	1	0.151	86	0.784	0.895	0.190	84
Visual perception	0.762	0.772	0.318	154	0.655	0.950	0.506	176
Spatial reasoning	0.658	0.925	0.594	207	0.819	0.955	0.339	239
Motor	0.737	0.940	0.403	278	0.993	0.993	0.006	324
Somatosensory	0.693	0.902	0.464	267	0.981	0.992	0.009	335

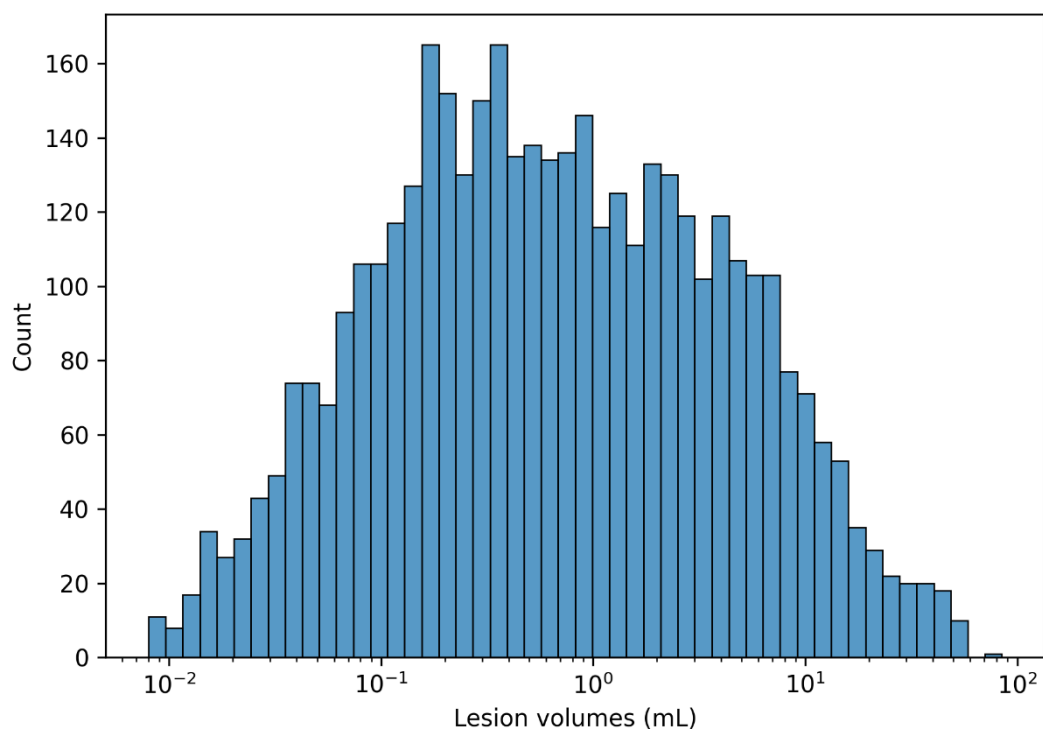
Separability, overlap and sample size characteristics of the virtual cohorts defined by functional subgroup and physiology type for lesion models. The *linear separability* column lists the balanced accuracy of a linear support vector machine trained to distinguish between “affected” and “unaffected” members of each cohort as defined by the intersection of the functional and physiological labels at a threshold of 0.05; the *overlap* column lists the proportion of lesions that exceed the threshold for both hypothetical treatments; and the *N* column lists the total number of patients from the dataset with lesions meeting the threshold for at least one subnetwork.

Disconnectomes, N = 4 119, threshold = 0.05,  $p > 0.5$

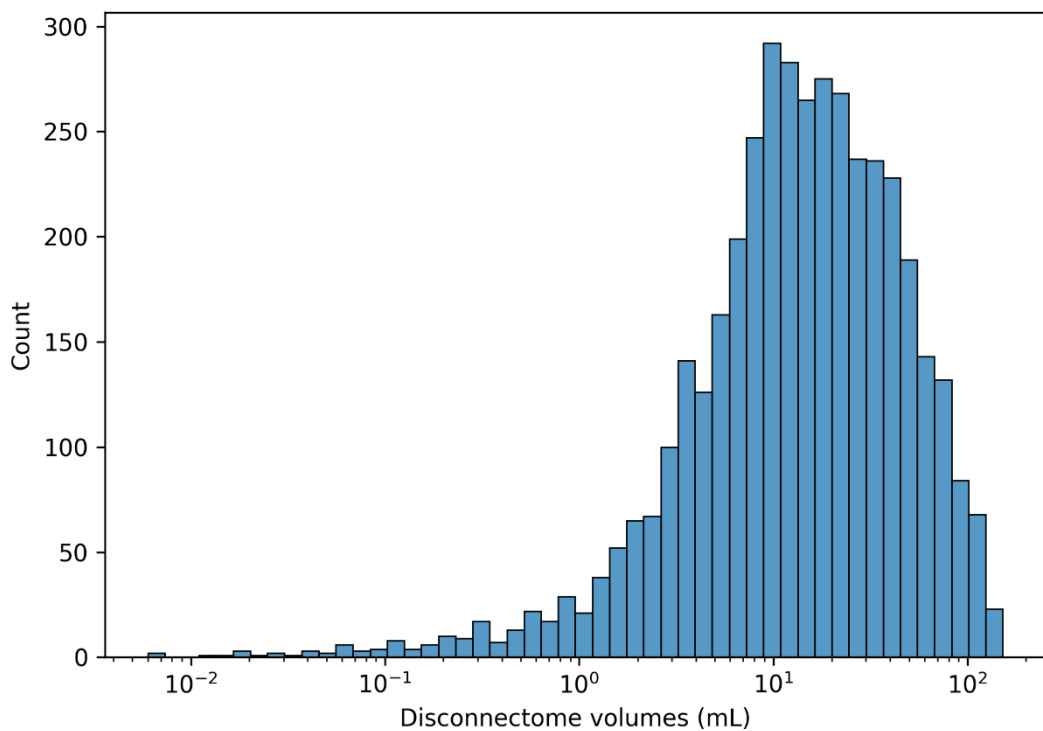
	Receptome				Transcriptome			
	Linear separability		Overlap	N	Linear separability		Overlap	N
	OR	XOR			OR	XOR		
Hearing	0.645	0.987	0.614	868	0.704	0.986	0.512	887
Language	0.593	0.500	0.660	688	0.989	0.998	0.009	851
Introspection	0.666	0.990	0.545	508	0.846	0.990	0.223	637
Cognition	0.574	0.800	0.573	853	0.580	0.982	0.743	829
Mood	0.605	0.988	0.604	364	0.645	0.949	0.588	381
Memory	0.617	NaN	0.409	978	0.566	0.958	0.708	955
Aversion	0.608	0.769	0.645	1503	0.556	0.953	0.800	1346
Coordination	0.529	0.772	0.698	325	0.607	0.943	0.616	378
Interoception	0.554	0.903	0.761	1806	0.583	0.823	0.675	1872
Sleep	0.652	0.939	0.553	3078	0.616	0.993	0.630	2781
Reward	0.629	0.974	0.658	1854	0.660	0.972	0.550	1993
Visual recognition	0.848	0.988	0.167	335	0.838	0.963	0.215	297
Visual perception	0.626	0.843	0.469	407	0.577	0.900	0.234	376
Spatial reasoning	0.662	0.972	0.408	1011	0.714	0.951	0.407	863
Motor	0.697	0.970	0.461	1230	0.903	0.998	0.157	1394
Somatosensory	0.700	0.966	0.452	1202	0.905	0.999	0.158	1427

Separability, overlap and sample size characteristics of the virtual cohorts defined by functional subgroup and physiology type for disconnectome models, where the disconnectome is binarized at a disconnection threshold of 0.5. The *linear separability* column lists the balanced accuracy of a linear support vector machine trained to distinguish between “affected” and “unaffected” members of each cohort as defined by the intersection of the functional and physiological labels at a threshold of 0.05; the *overlap* column lists the proportion of lesions that exceed the threshold for both hypothetical treatments; and the *N* column lists the total number of patients from the dataset with lesions meeting the threshold for at least one subnetwork.

## S7: Lesion volume distribution

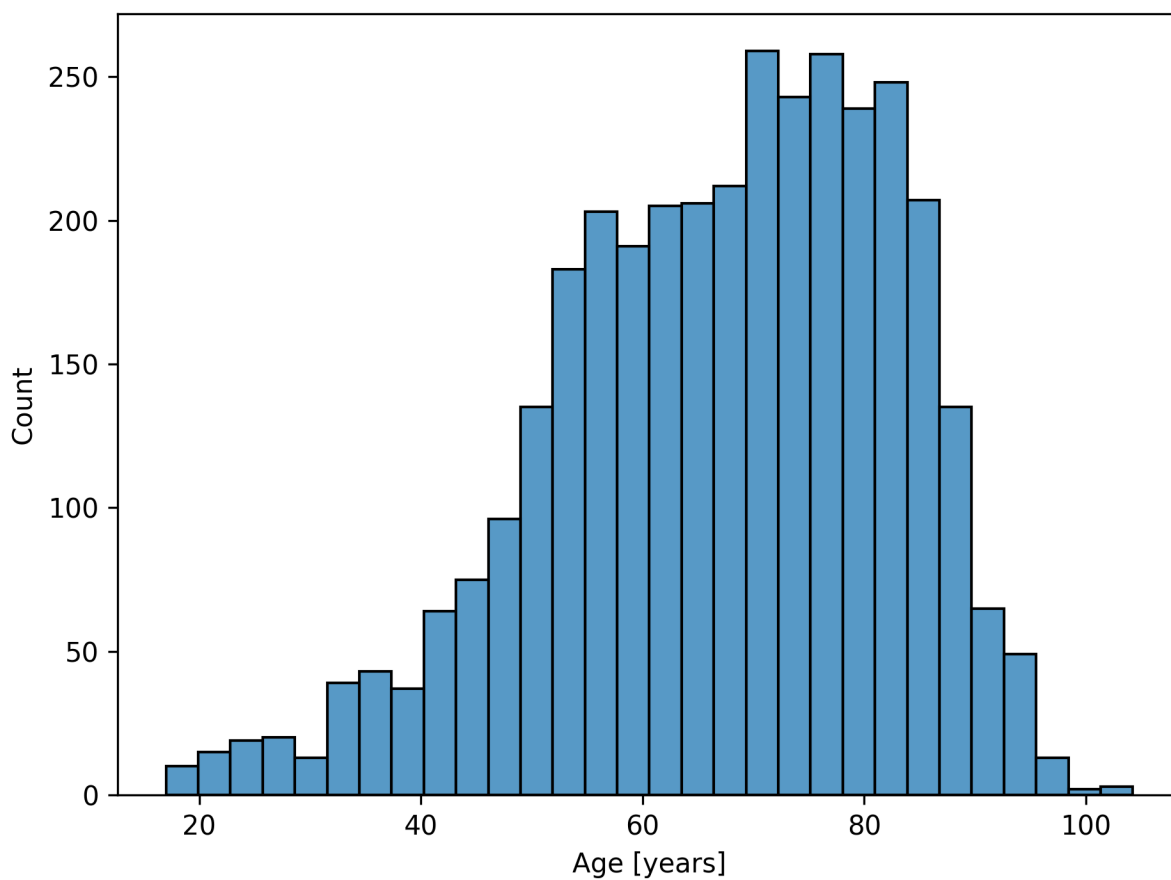


Histogram showing the distribution of lesion volumes for the dataset of 4 119 events, after non-linear registration to MNI space. The mean is 2.92 mL, with standard deviation of 6.37 mL. Note decimal log scale.



Histogram showing the distribution of binarized ( $p > 0.5$ ) disconnectome volumes for the dataset of 4 119 events, after non-linear registration to MNI space. The mean is 23.56 mL, with standard deviation of 25.26 mL. Note decimal log scale.

## S8: Patient age distribution



Histogram showing the distribution of patient age. Age data was available for 3487/4119 images and exhibited a mean of 67.042 years and standard deviation 15.46 years. From 3478/4119 images with complete data on patient sex, 1960 were recorded as male (56.4%) and 1518 as female (43.6%).

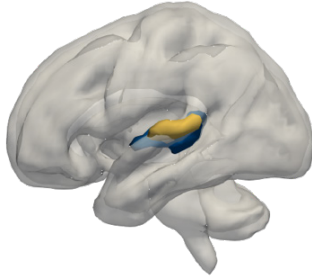
## S9: Neurotransmitter receptome subnetworks

Functional Deficit	Primary receptor type	Secondary receptor type
Hearing	Noradrenaline	Glutamate
Language	Cannabinoid	Glutamate
Introspection	Glutamate	5HT
Cognition	Cannabinoid	Opioid
Mood	Opioid	Histamine
Memory	Dopamine	5HT
Aversion	Dopamine	Histamine
Coordination	Opioid	Acetylcholine
Interoception	Dopamine	Histamine
Sleep	Opioid	Noradrenaline
Reward	Dopamine	Histamine
Visual recognition	Cannabinoid	GABA
Visual perception	GABA	5HT
Spatial reasoning	Glutamate	Noradrenaline
Motor	Noradrenaline	Glutamate
Somatosensory	Noradrenaline	Glutamate

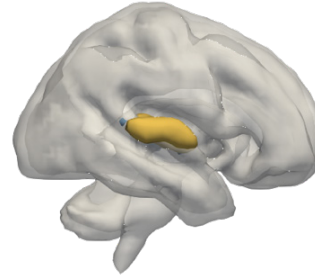
The primary and secondary receptor classes by preponderance within each of the functional networks, according to aggregation of Z-valued transformations of positron emission tomography data, each targeted to receptor subclasses. The preponderance was determined by the proportions of voxels from each functional network whose receptor type aggregated Z-value was maximal (primary) and second-maximal (secondary) over all others. The following figures show, for each functional network, the functional network subdivisions based upon neurotransmitter receptor preponderance, derived from positron emission tomography data made available by Hansen et al. (2022).

### S9.1.1: *Hearing* subnetwork render

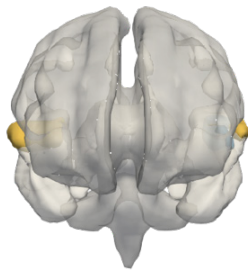
**a**



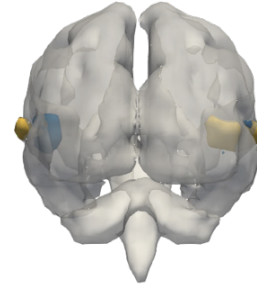
**b**



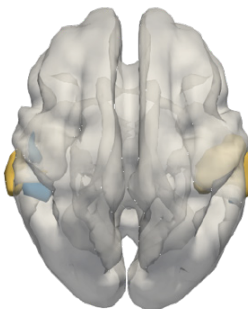
**c**



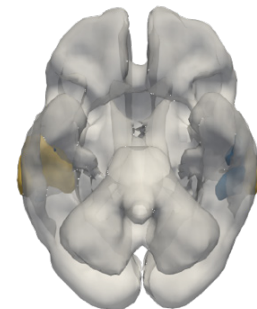
**d**



**e**

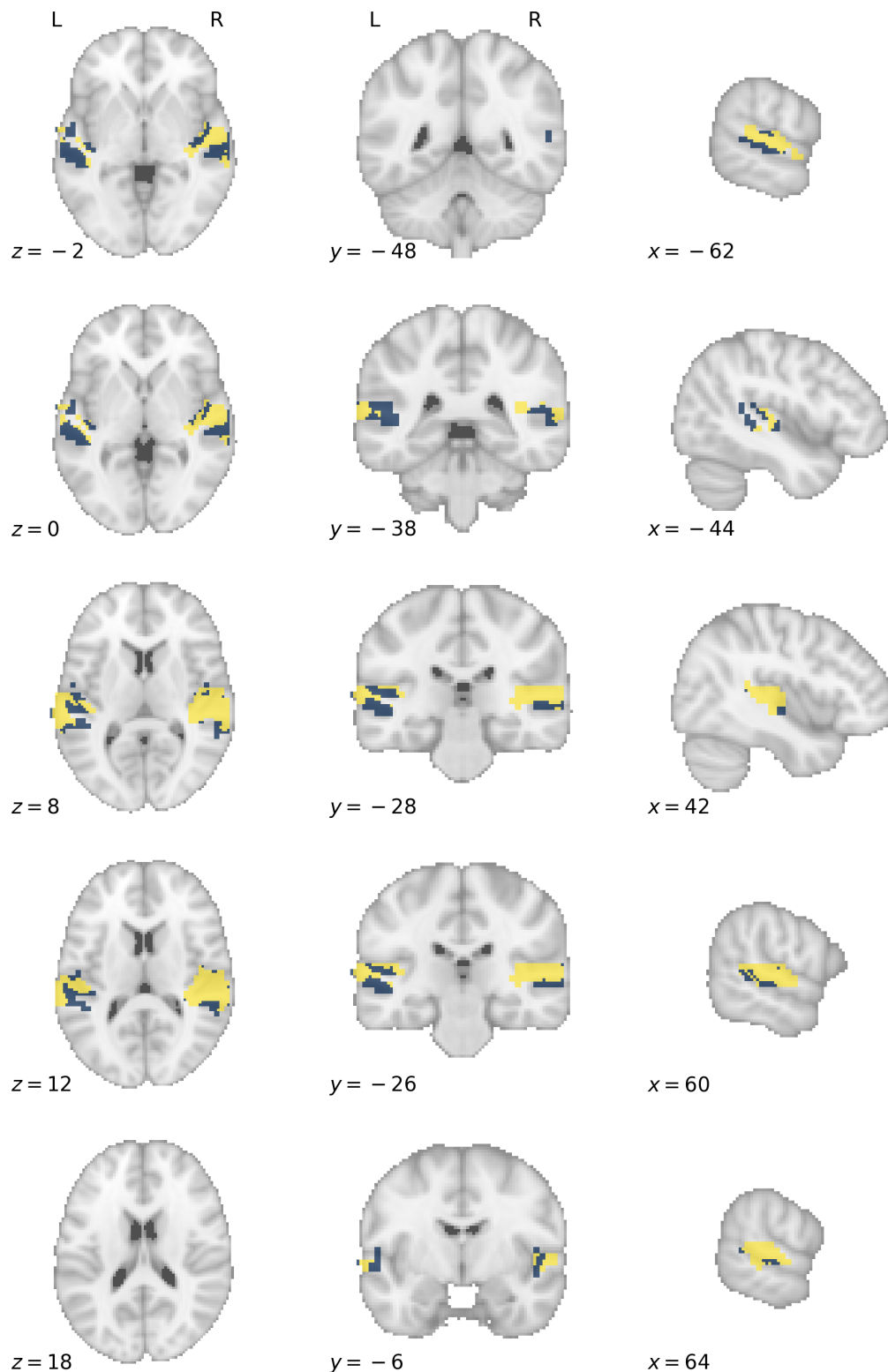


**f**



Three-dimensional rendering of the functional grey matter network representing *hearing*. The colours label functional subnetworks separated by neurotransmitter receptor distribution preponderance, here noradrenaline in yellow and glutamate in blue. This forms the basis upon which treatment effect heterogeneity is simulated, with hypothetical treatments selectively effective for lesions disrupting defined receptor territories. Each panel shows the same render from a different spatial perspective: **a**, left; **b**, right; **c**, anterior; **d**, posterior, **e**, superior; **f**, inferior. The underlay is a thresholded white matter template surface in MNI.

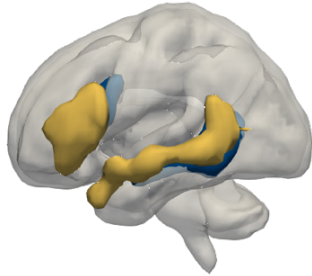
### S9.1.2: *Hearing* subnetwork axial slices



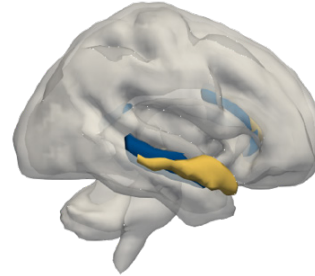
Axial slice visualisation of the functional grey matter network representing *hearing*, overlaid onto the standard MNI152 template. The labelled co-ordinates map to MNI space. The colours label functional subnetworks separated by neurotransmitter receptor distribution preponderance, here noradrenaline in yellow and glutamate in blue. This forms the basis upon which treatment effect heterogeneity is simulated, with hypothetical treatments selectively effective for lesions disrupting defined receptor territories.

### S9.2.1: *Language* subnetwork render

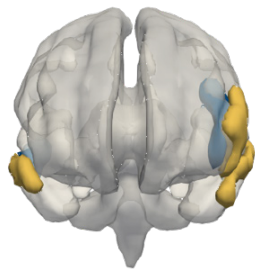
a



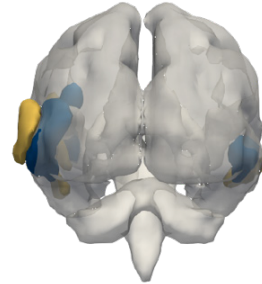
b



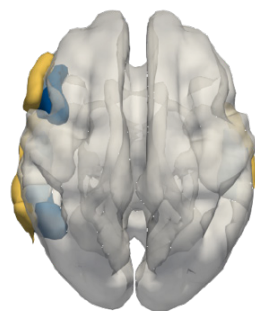
c



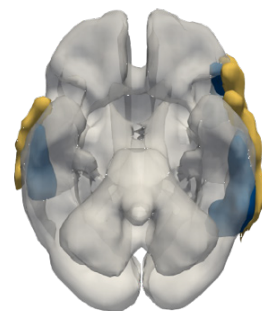
d



e

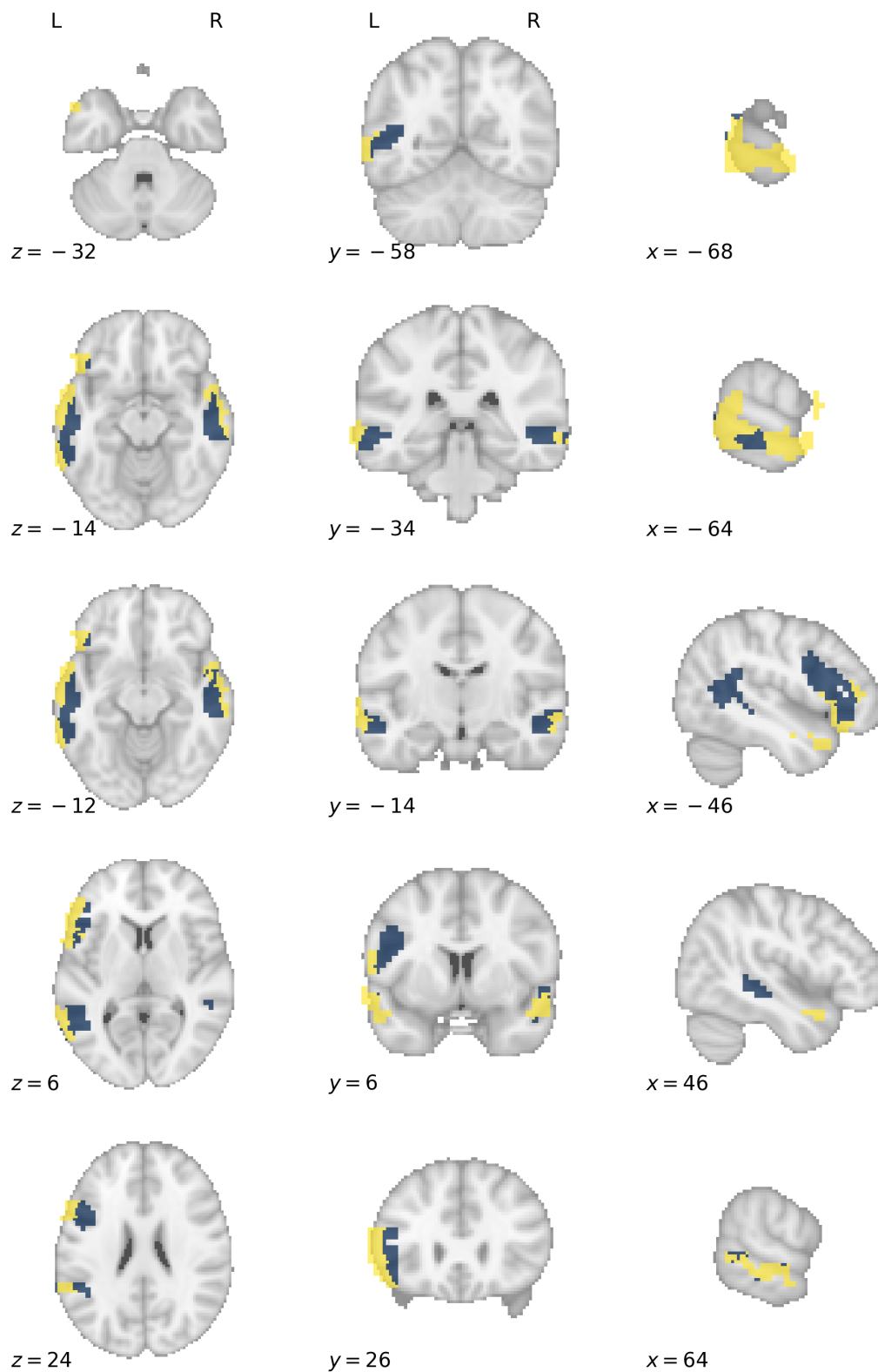


f



Three-dimensional rendering of the functional grey matter network representing *language*. The colours label functional subnetworks separated by neurotransmitter receptor distribution preponderance, here cannabinoid in yellow and glutamate in blue. This forms the basis upon which treatment effect heterogeneity is simulated, with hypothetical treatments selectively effective for lesions disrupting defined receptor territories. Each panel shows the same render from a different spatial perspective: **a**, left; **b**, right; **c**, anterior; **d**, posterior, **e**, superior; **f**, inferior. The underlay is a thresholded white matter template surface in MNI.

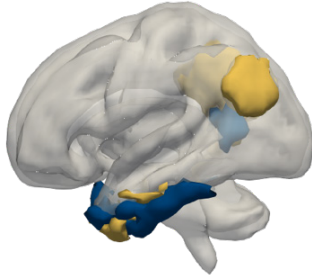
### S9.2.2: *Language* subnetwork axial slices



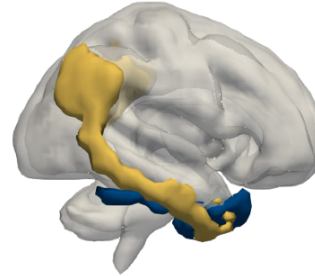
Axial slice visualisation of the functional grey matter network representing *language*, overlaid onto the standard MNI152 template. The labelled co-ordinates map to MNI space. The colours label functional subnetworks separated by neurotransmitter receptor distribution preponderance, here cannabinoid in yellow and glutamate in blue. This forms the basis upon which treatment effect heterogeneity is simulated, with hypothetical treatments selectively effective for lesions disrupting defined receptor territories.

### S9.3.1: *Introspection* subnetwork render

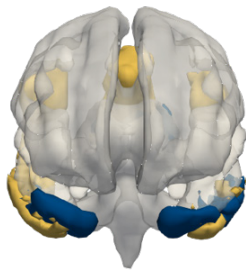
a



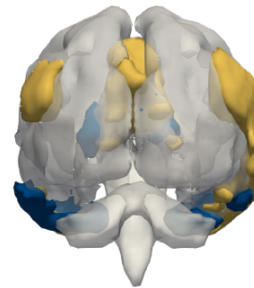
b



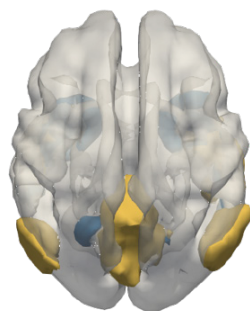
c



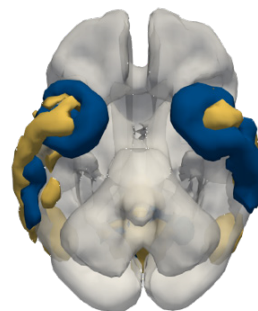
d



e

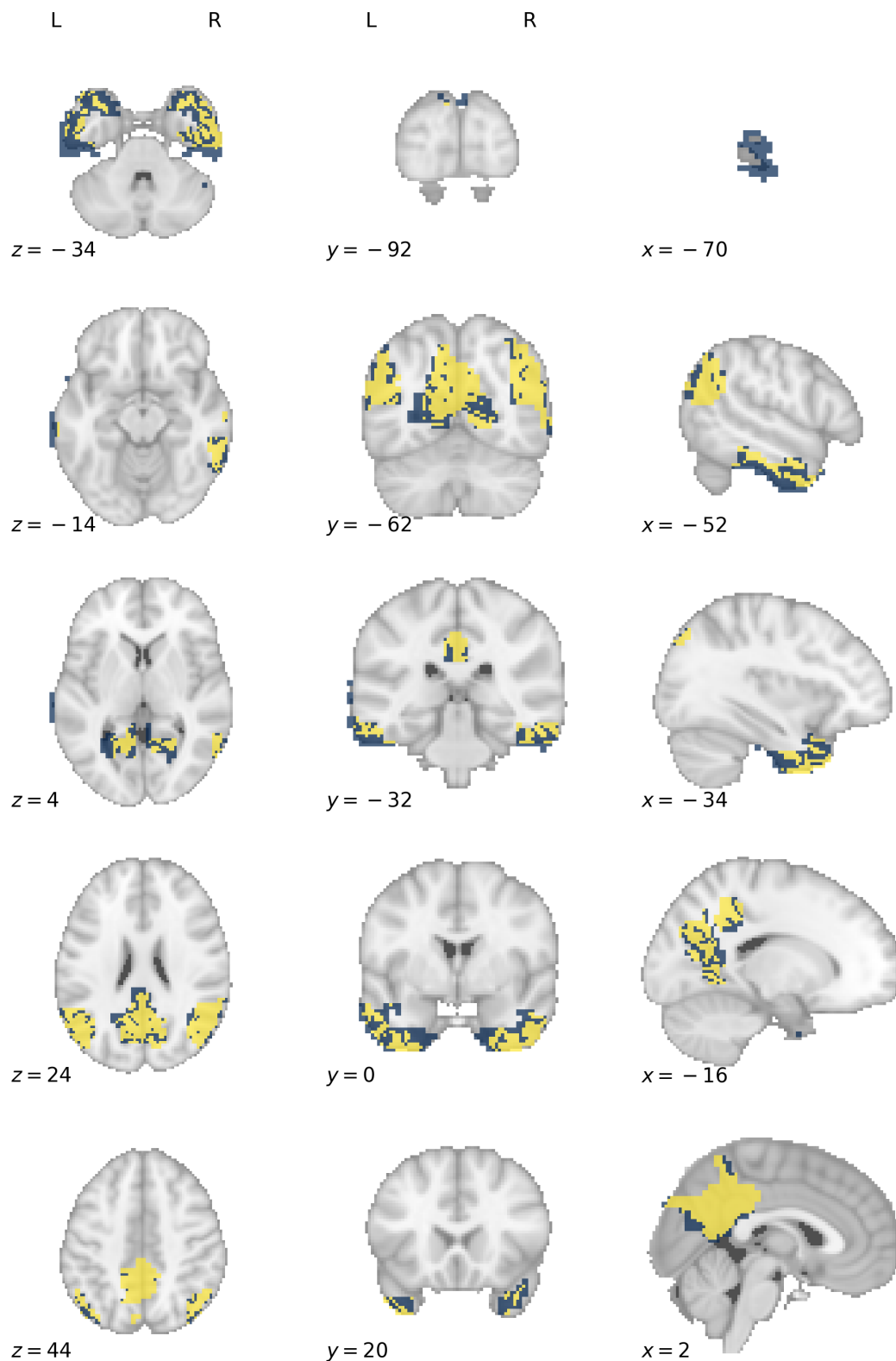


f



Three-dimensional rendering of the functional grey matter network representing *introspection*. The colours label functional subnetworks separated by neurotransmitter receptor distribution preponderance, here glutamate in yellow and 5HT in blue. This forms the basis upon which treatment effect heterogeneity is simulated, with hypothetical treatments selectively effective for lesions disrupting defined receptor territories. Each panel shows the same render from a different spatial perspective: **a**, left; **b**, right; **c**, anterior; **d**, posterior; **e**, superior; **f**, inferior. The underlay is a thresholded white matter template surface in MNI.

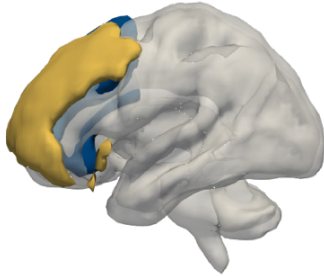
### S9.3.2: *Introspection* subnetwork axial slices



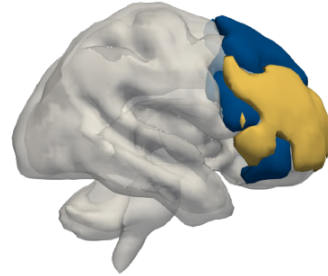
Axial slice visualisation of the functional grey matter network representing *introspection*, overlaid onto the standard MNI152 template. The labelled co-ordinates map to MNI space. The colours label functional subnetworks separated by neurotransmitter receptor distribution preponderance, here glutamate in yellow and 5HT in blue. This forms the basis upon which treatment effect heterogeneity is simulated, with hypothetical treatments selectively effective for lesions disrupting defined receptor territories.

### S9.4.1: *Cognition* subnetwork render

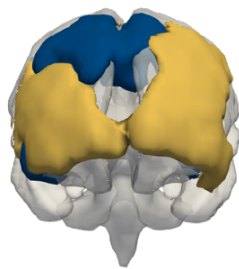
a



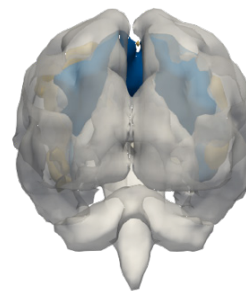
b



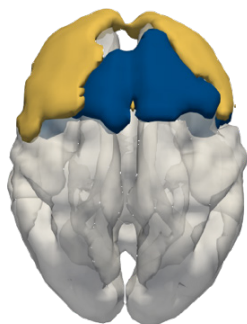
c



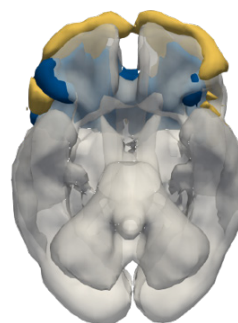
d



e

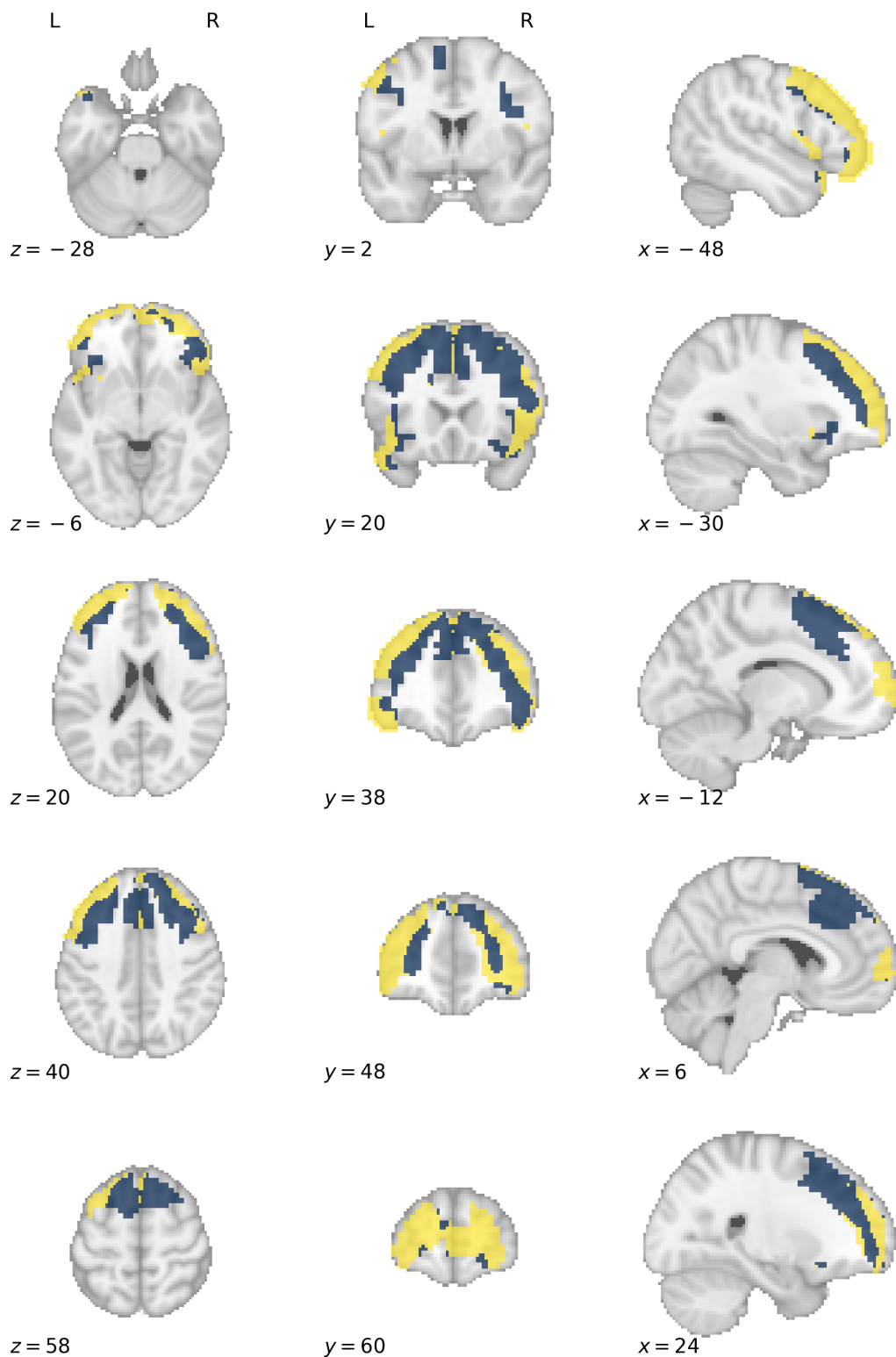


f



Three-dimensional rendering of the functional grey matter network representing *cognition*. The colours label functional subnetworks separated by neurotransmitter receptor distribution preponderance, here cannabinoid in yellow and opioid in blue. This forms the basis upon which treatment effect heterogeneity is simulated, with hypothetical treatments selectively effective for lesions disrupting defined receptor territories. Each panel shows the same render from a different spatial perspective: **a**, left; **b**, right; **c**, anterior; **d**, posterior, **e**, superior; **f**, inferior. The underlay is a thresholded white matter template surface in MNI.

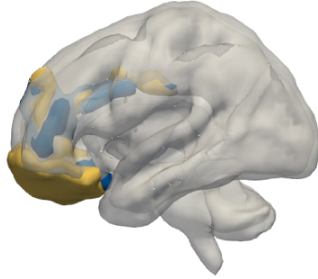
### S9.4.2: *Cognition* subnetwork axial slices



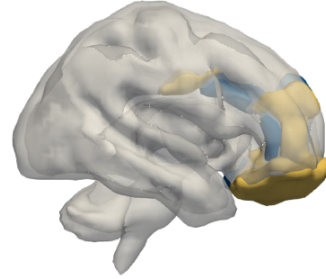
Axial slice visualisation of the functional grey matter network representing *cognition*, overlaid onto the standard MNI152 template. The labelled co-ordinates map to MNI space. The colours label functional subnetworks separated by neurotransmitter receptor distribution preponderance, here cannabinoid in yellow and opioid in blue. This forms the basis upon which treatment effect heterogeneity is simulated, with hypothetical treatments selectively effective for lesions disrupting defined receptor territories.

### S9.5.1: *Mood* subnetwork render

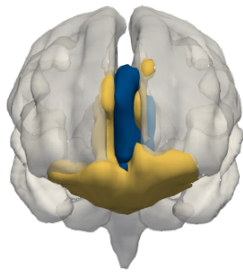
**a**



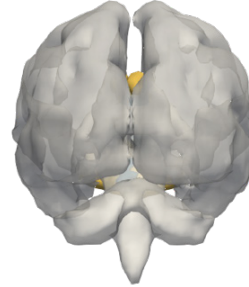
**b**



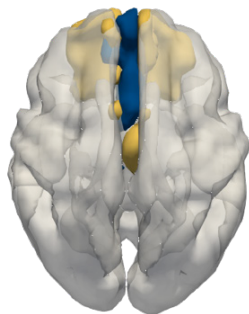
**c**



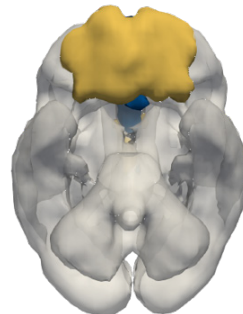
**d**



**e**

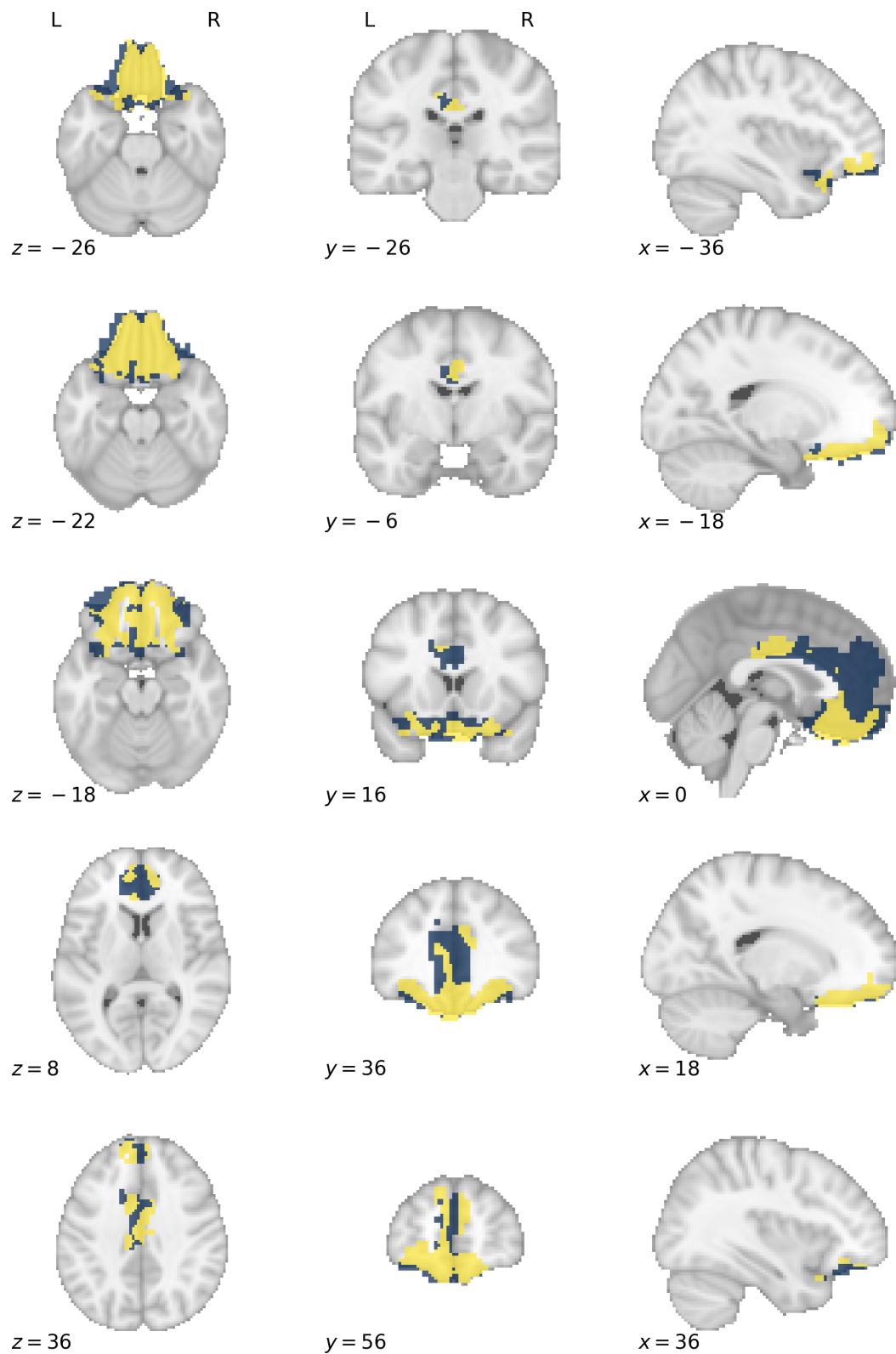


**f**



Three-dimensional rendering of the functional grey matter network representing *mood*. The colours label functional subnetworks separated by neurotransmitter receptor distribution preponderance, here opioid in yellow and histamine in blue. This forms the basis upon which treatment effect heterogeneity is simulated, with hypothetical treatments selectively effective for lesions disrupting defined receptor territories. Each panel shows the same render from a different spatial perspective: **a**, left; **b**, right; **c**, anterior; **d**, posterior; **e**, superior; **f**, inferior. The underlay is a thresholded white matter template surface in MNI.

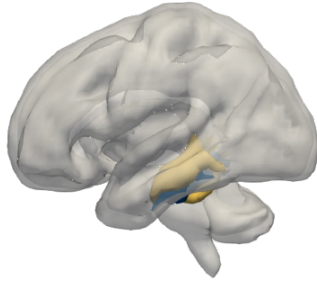
### S9.5.2: *Mood* subnetwork axial slices



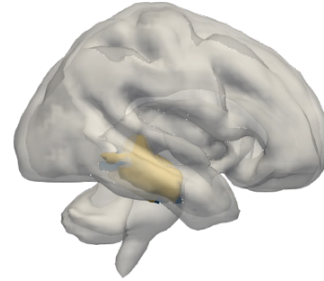
Axial slice visualisation of the functional grey matter network representing *mood*, overlaid onto the standard MNI152 template. The labelled co-ordinates map to MNI space. The colours label functional subnetworks separated by neurotransmitter receptor distribution preponderance, here opioid in yellow and histamine in blue. This forms the basis upon which treatment effect heterogeneity is simulated, with hypothetical treatments selectively effective for lesions disrupting defined receptor territories.

### S9.6.1: *Memory* subnetwork render

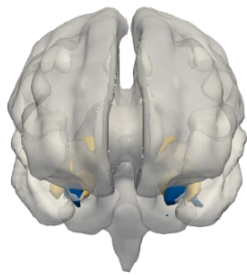
c



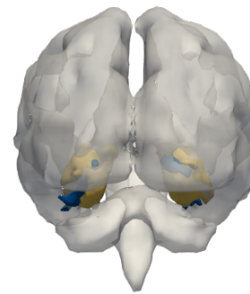
d



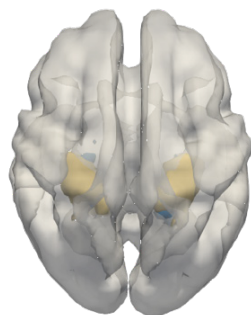
c



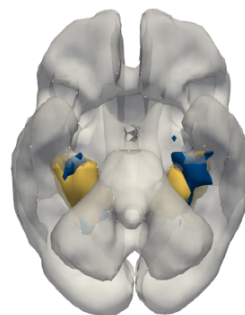
d



e

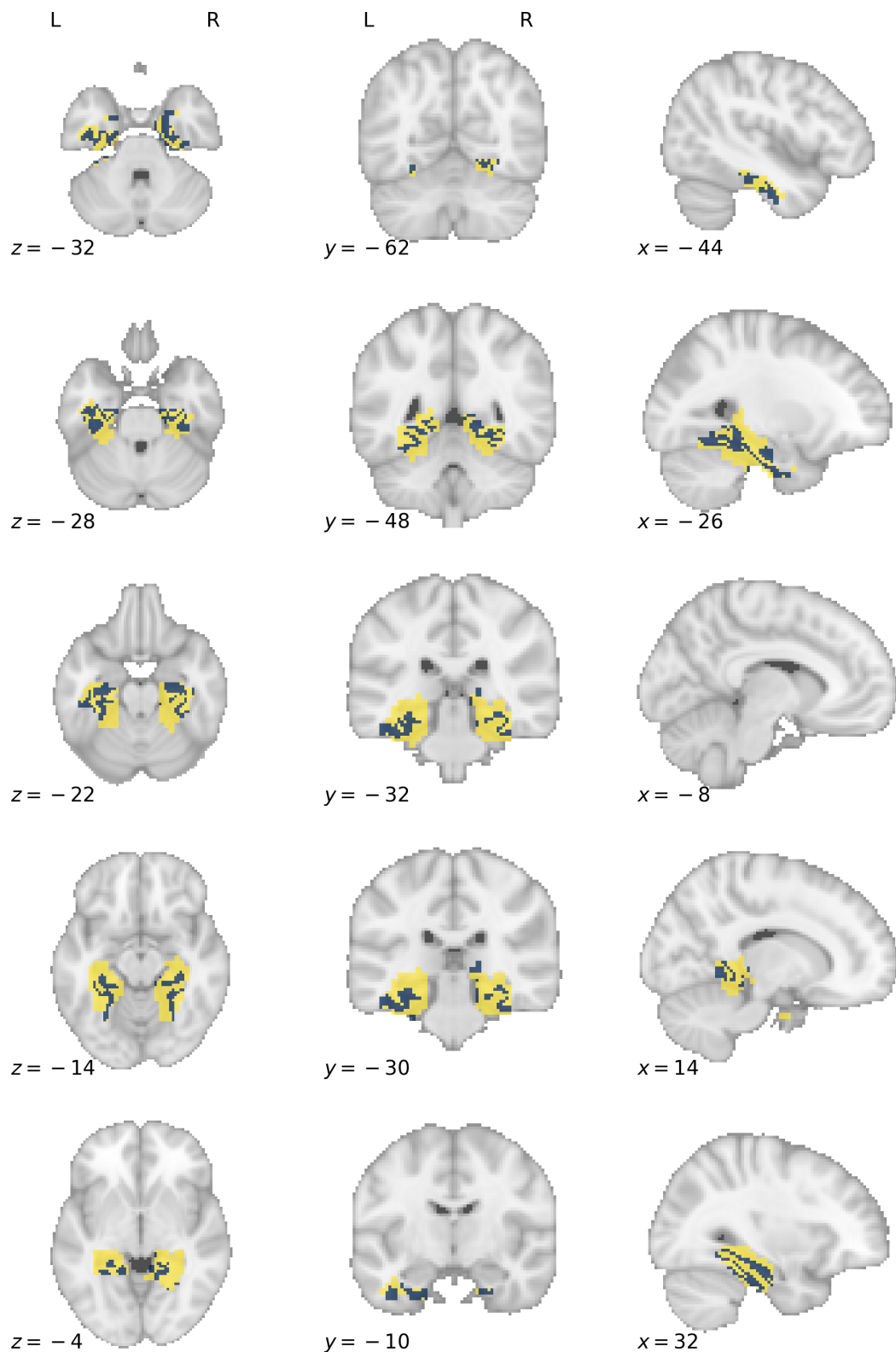


f



Three-dimensional rendering of the functional grey matter network representing *memory*. The colours label functional subnetworks separated by neurotransmitter receptor distribution preponderance, here dopamine in yellow and 5HT in blue. This forms the basis upon which treatment effect heterogeneity is simulated, with hypothetical treatments selectively effective for lesions disrupting defined receptor territories. Each panel shows the same render from a different spatial perspective: **a**, left; **b**, right; **c**, anterior; **d**, posterior, **e**, superior; **f**, inferior. The underlay is a thresholded white matter template surface in MNI.

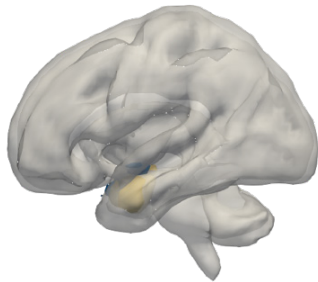
### S9.6.2: *Memory* subnetwork axial slices



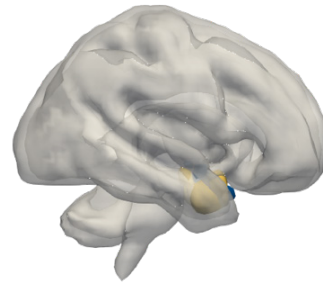
Axial slice visualisation of the functional grey matter network representing *memory*, overlaid onto the standard MNI152 template. The labelled co-ordinates map to MNI space. The colours label functional subnetworks separated by neurotransmitter receptor distribution preponderance, here dopamine in yellow and 5HT in blue. This forms the basis upon which treatment effect heterogeneity is simulated, with hypothetical treatments selectively effective for lesions disrupting defined receptor territories.

### S9.7.1: *Aversion* subnetwork render

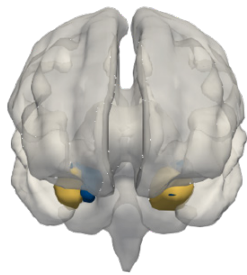
a



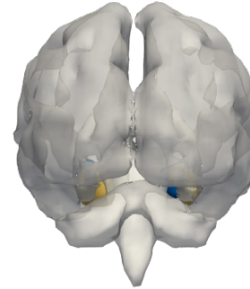
b



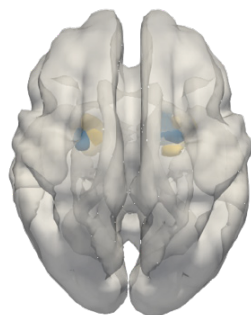
c



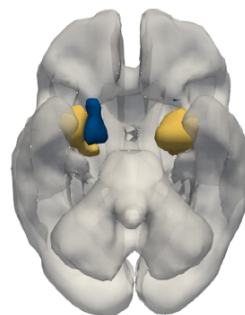
d



e

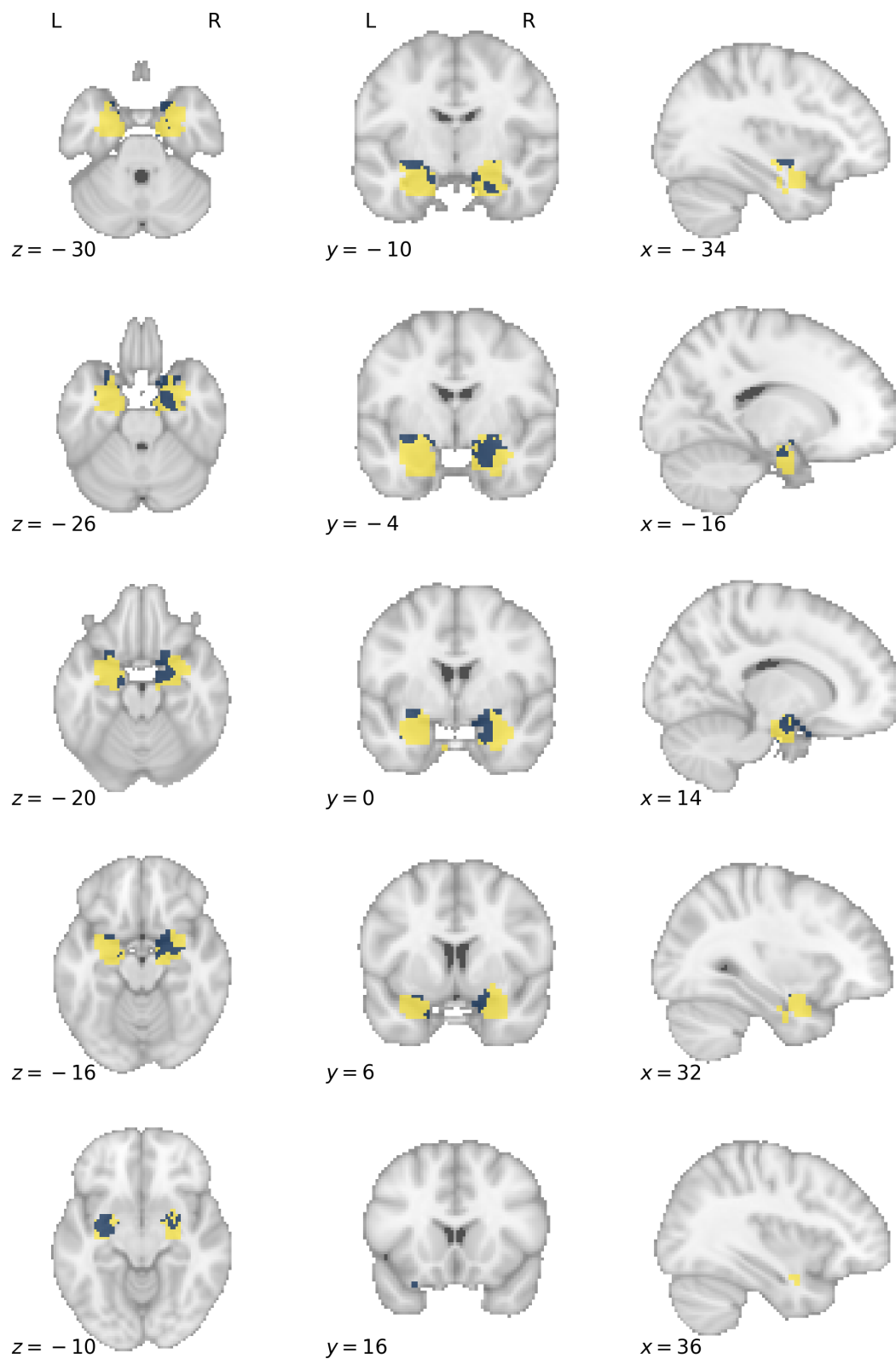


f



Three-dimensional rendering of the functional grey matter network representing *aversion*. The colours label functional subnetworks separated by neurotransmitter receptor distribution preponderance, here dopamine in yellow and histamine in blue. This forms the basis upon which treatment effect heterogeneity is simulated, with hypothetical treatments selectively effective for lesions disrupting defined receptor territories. Each panel shows the same render from a different spatial perspective: **a**, left; **b**, right; **c**, anterior; **d**, posterior, **e**, superior; **f**, inferior. The underlay is a thresholded white matter template surface in MNI.

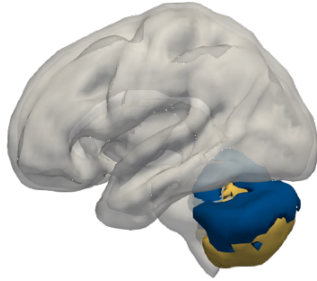
### S9.7.2: *Aversion* subnetwork axial slices



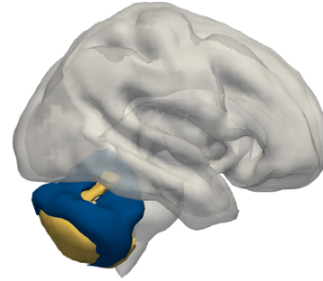
Axial slice visualisation of the functional grey matter network representing *aversion*, overlaid onto the standard MNI152 template. The labelled co-ordinates map to MNI space. The colours label functional subnetworks separated by neurotransmitter receptor distribution preponderance, here dopamine in yellow and histamine in blue. This forms the basis upon which treatment effect heterogeneity is simulated, with hypothetical treatments selectively effective for lesions disrupting defined receptor territories.

### S9.8.1: *Coordination* subnetwork render

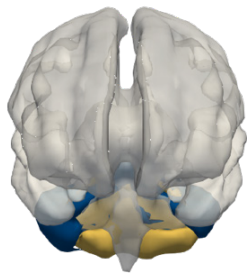
a



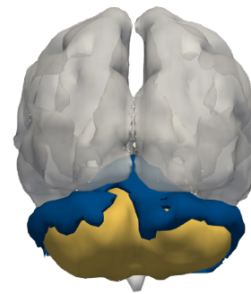
b



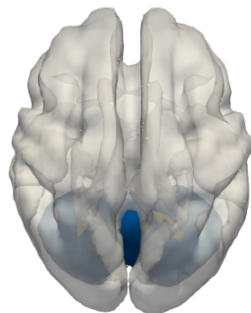
c



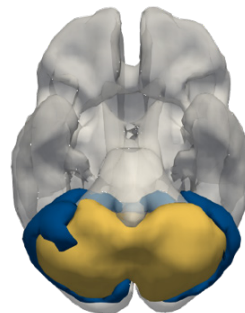
d



e

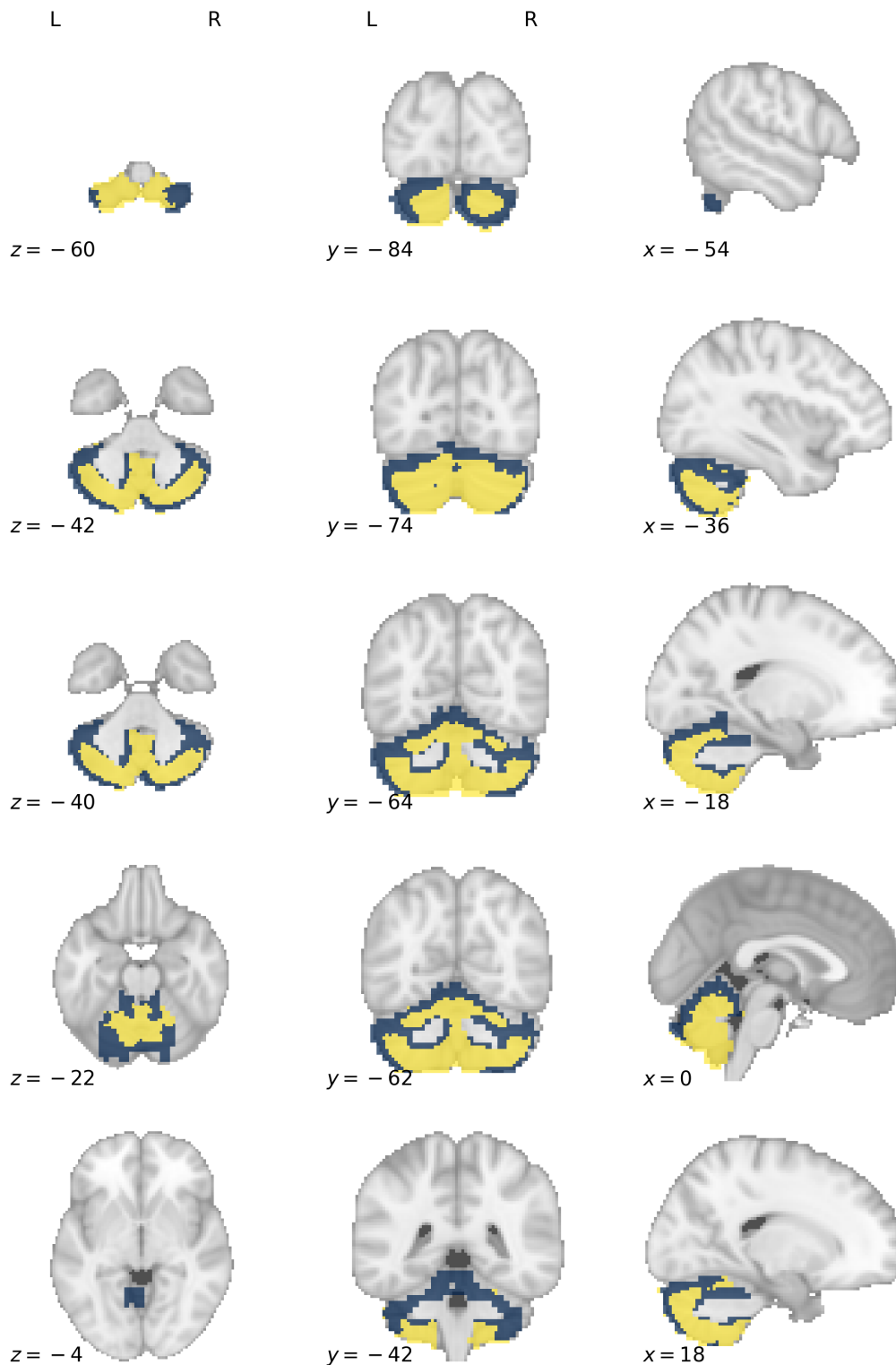


f



Three-dimensional rendering of the functional grey matter network representing *coordination*. The colours label functional subnetworks separated by neurotransmitter receptor distribution preponderance, here opioid in yellow and acetylcholine in blue. This forms the basis upon which treatment effect heterogeneity is simulated, with hypothetical treatments selectively effective for lesions disrupting defined receptor territories. Each panel shows the same render from a different spatial perspective: **a**, left; **b**, right; **c**, anterior; **d**, posterior, **e**, superior; **f**, inferior. The underlay is a thresholded white matter template surface in MNI.

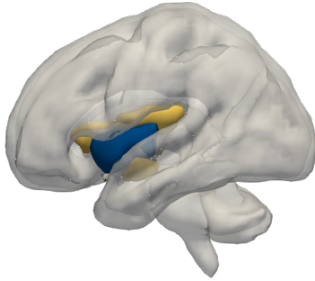
### S9.8.2: *Coordination* subnetwork axial slices



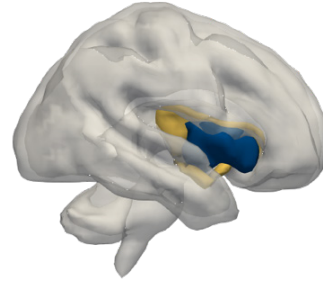
Axial slice visualisation of the functional grey matter network representing *coordination*, overlaid onto the standard MNI152 template. The labelled co-ordinates map to MNI space. The colours label functional subnetworks separated by neurotransmitter receptor distribution preponderance, here opioid in yellow and acetylcholine in blue. This forms the basis upon which treatment effect heterogeneity is simulated, with hypothetical treatments selectively effective for lesions disrupting defined receptor territories.

### S9.9.1: *Interoception* subnetwork render

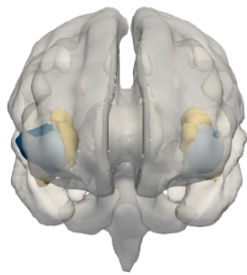
a



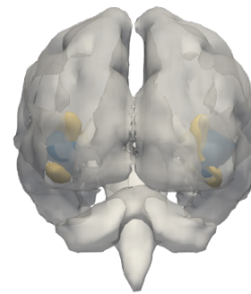
b



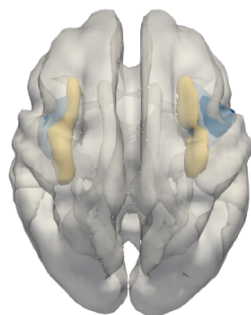
c



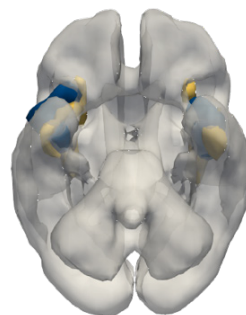
d



e

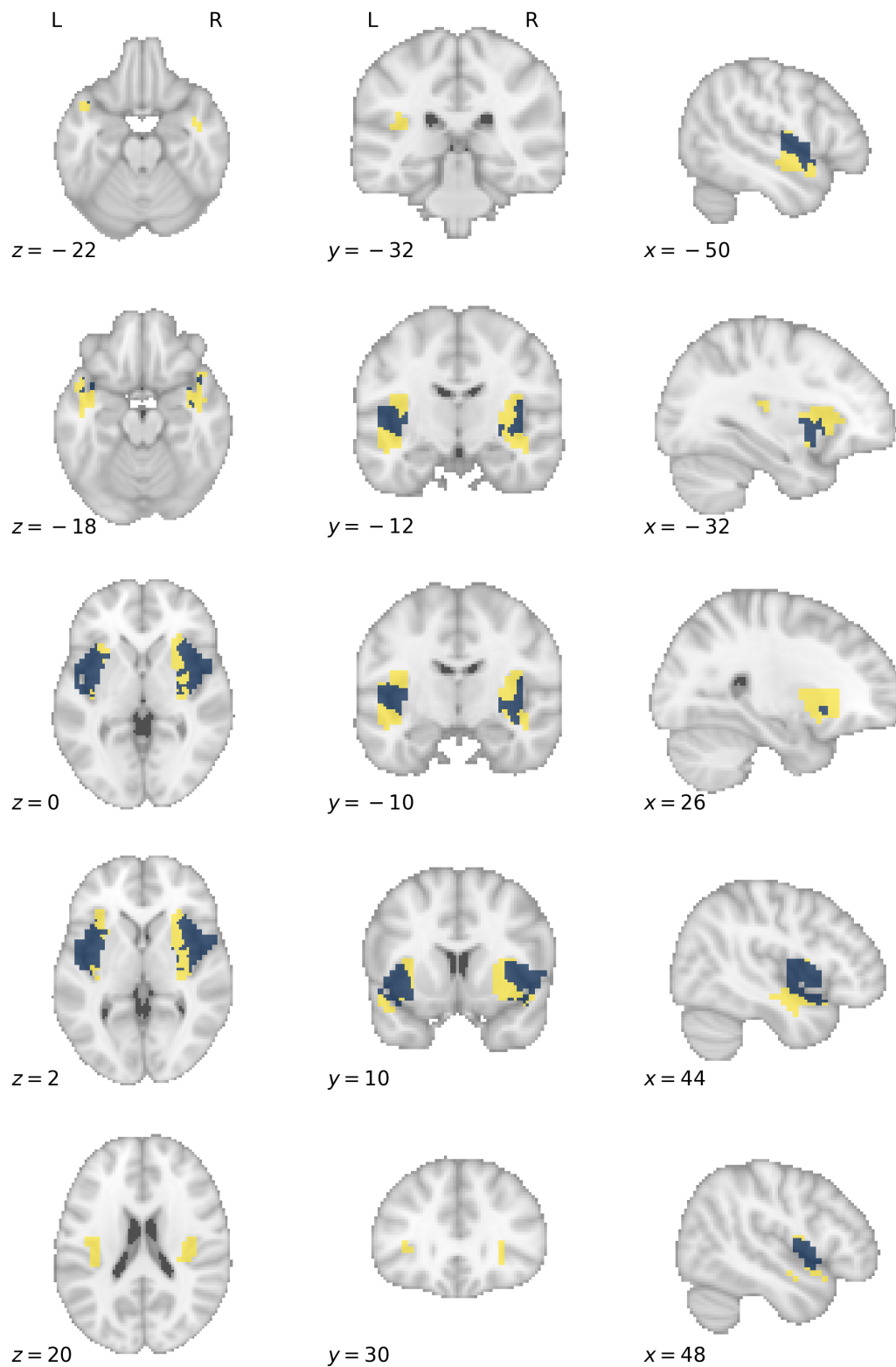


f



Three-dimensional rendering of the functional grey matter network representing *interoception*. The colours label functional subnetworks separated by neurotransmitter receptor distribution preponderance, here dopamine in yellow and histamine in blue. This forms the basis upon which treatment effect heterogeneity is simulated, with hypothetical treatments selectively effective for lesions disrupting defined receptor territories. Each panel shows the same render from a different spatial perspective: **a**, left; **b**, right; **c**, anterior; **d**, posterior, **e**, superior; **f**, inferior. The underlay is a thresholded white matter template surface in MNI.

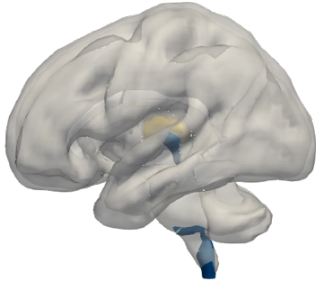
### S9.9.2: *Interoception* subnetwork axial slices



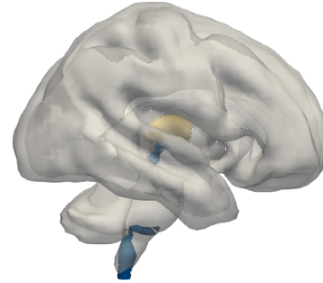
Axial slice visualisation of the functional grey matter network representing *interoception*, overlaid onto the standard MNI152 template. The labelled co-ordinates map to MNI space. The colours label functional subnetworks separated by neurotransmitter receptor distribution preponderance, here dopamine in yellow and histamine in blue. This forms the basis upon which treatment effect heterogeneity is simulated, with hypothetical treatments selectively effective for lesions disrupting defined receptor territories.

### S9.10.1: *Sleep* subnetwork render

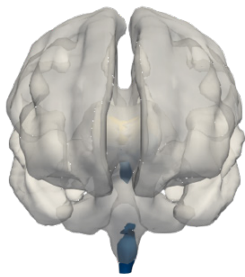
a



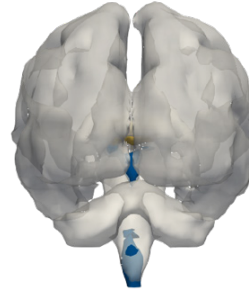
b



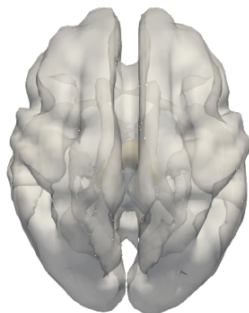
c



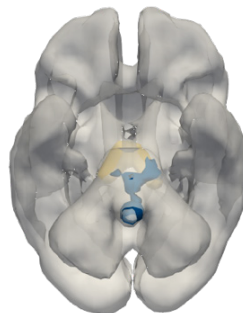
d



e

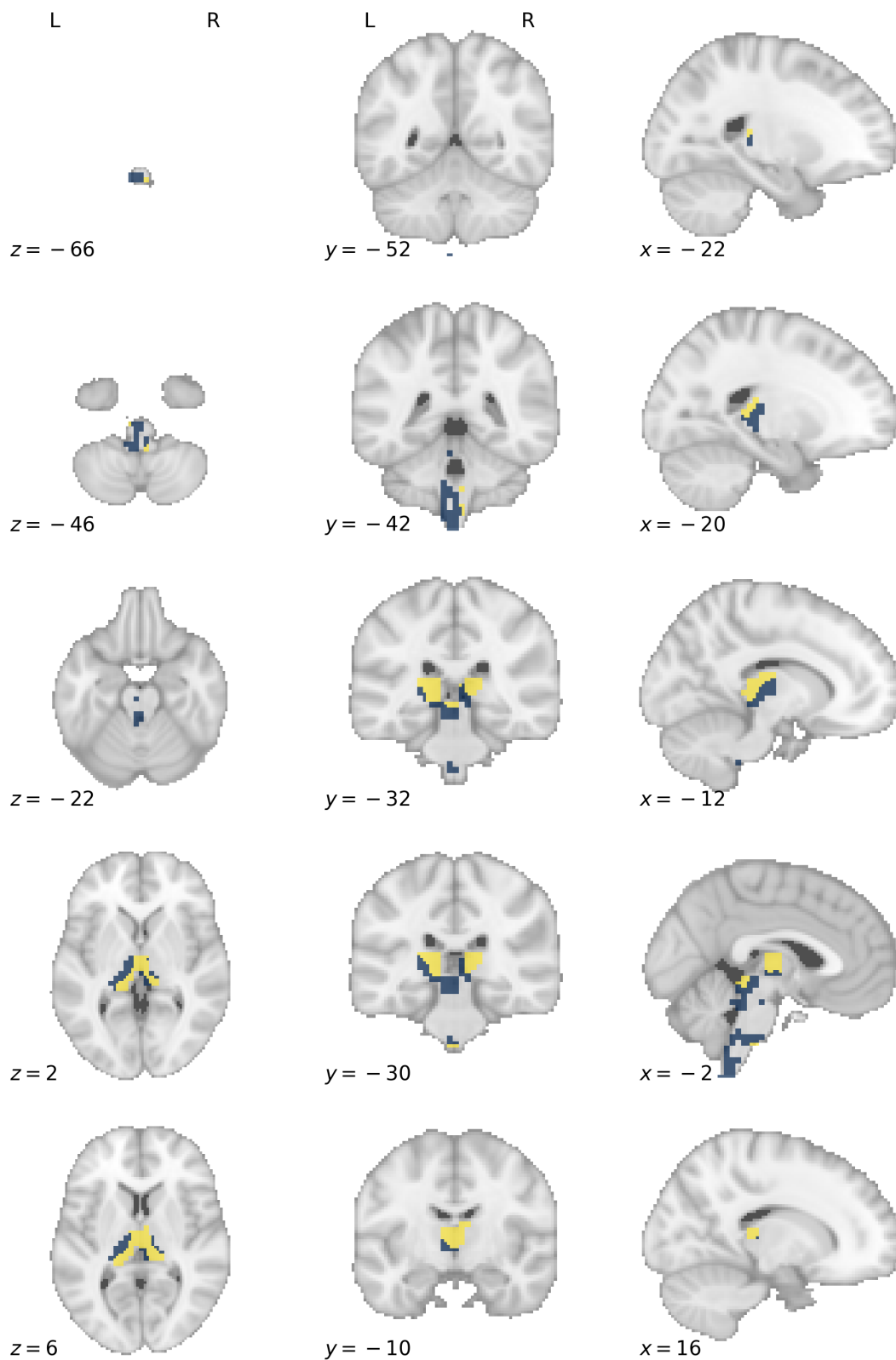


f



Three-dimensional rendering of the functional grey matter network representing *sleep*. The colours label functional subnetworks separated by neurotransmitter receptor distribution preponderance, here opioid in yellow and noradrenaline in blue. This forms the basis upon which treatment effect heterogeneity is simulated, with hypothetical treatments selectively effective for lesions disrupting defined receptor territories. Each panel shows the same render from a different spatial perspective: **a**, left; **b**, right; **c**, anterior; **d**, posterior, **e**, superior; **f**, inferior. The underlay is a thresholded white matter template surface in MNI.

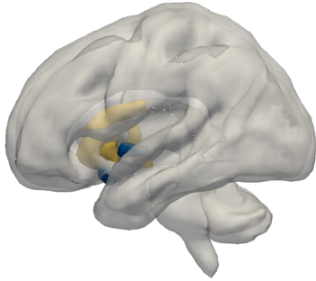
### S9.10.2: *Sleep* subnetwork axial slices



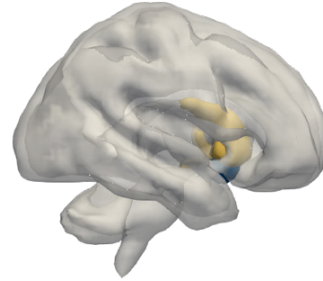
Axial slice visualisation of the functional grey matter network representing *sleep*, overlaid onto the standard MNI152 template. The labelled co-ordinates map to MNI space. The colours label functional subnetworks separated by neurotransmitter receptor distribution preponderance, here opioid in yellow and noradrenaline in blue. This forms the basis upon which treatment effect heterogeneity is simulated, with hypothetical treatments selectively effective for lesions disrupting defined receptor territories.

### S9.11.1: *Reward* subnetwork render

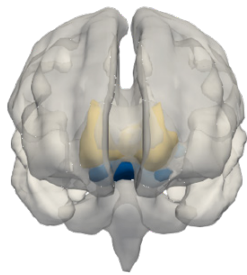
a



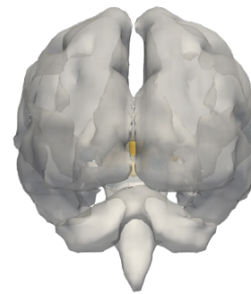
b



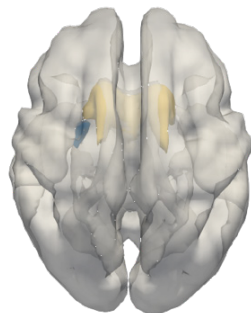
c



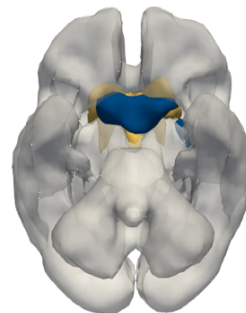
d



e

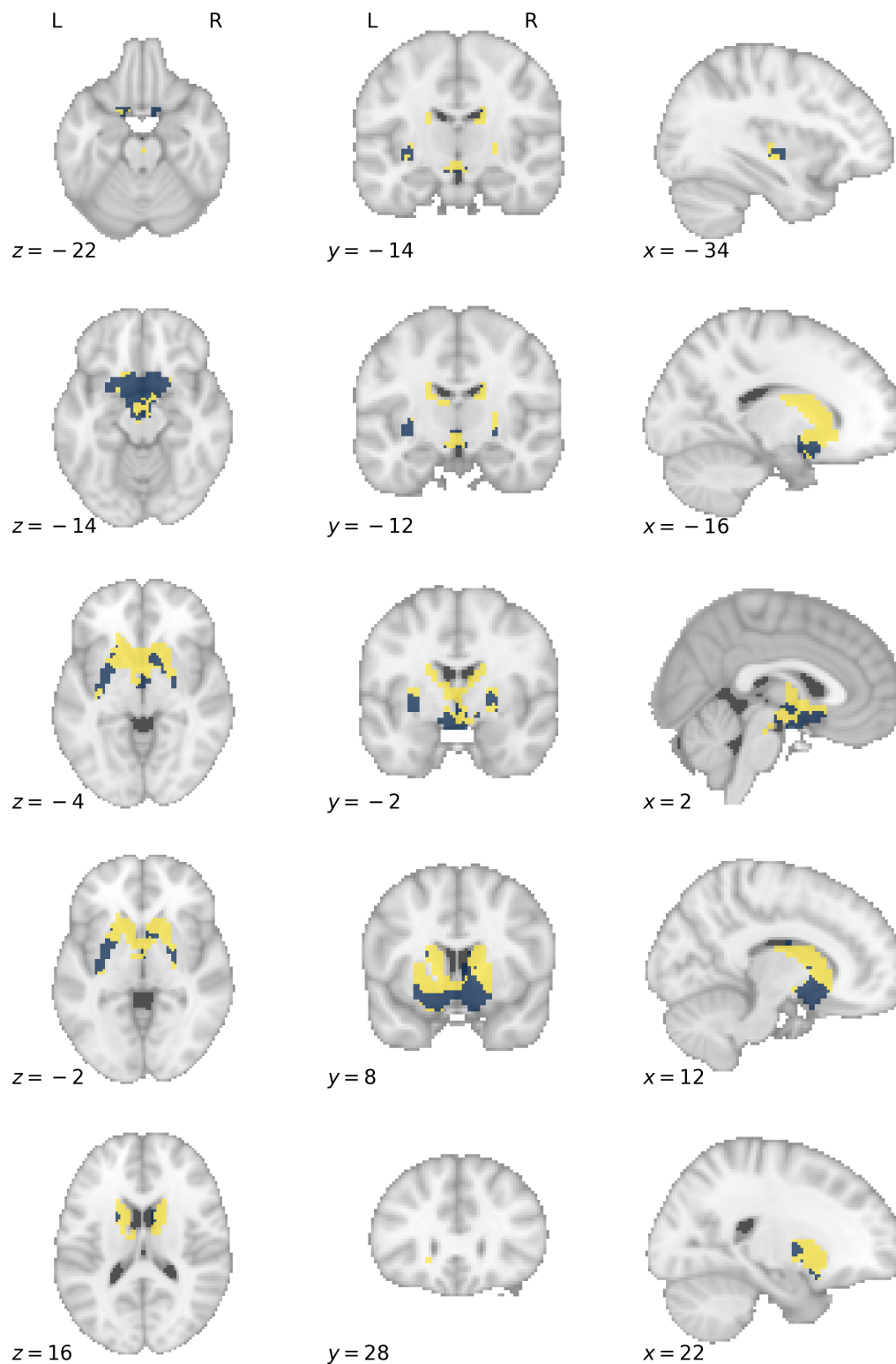


f



Three-dimensional rendering of the functional grey matter network representing *reward*. The colours label functional subnetworks separated by neurotransmitter receptor distribution preponderance, here dopamine in yellow and histamine in blue. This forms the basis upon which treatment effect heterogeneity is simulated, with hypothetical treatments selectively effective for lesions disrupting defined receptor territories. Each panel shows the same render from a different spatial perspective: **a**, left; **b**, right; **c**, anterior; **d**, posterior, **e**, superior; **f**, inferior. The underlay is a thresholded white matter template surface in MNI.

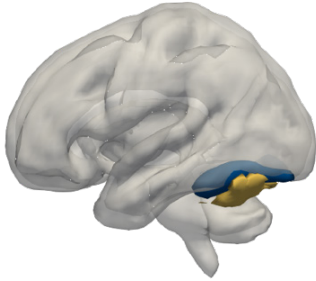
### S9.11.2: *Reward* subnetwork axial slices



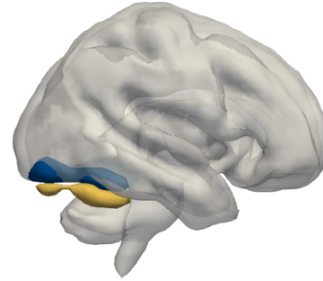
Axial slice visualisation of the functional grey matter network representing *reward*, overlaid onto the standard MNI152 template. The labelled co-ordinates map to MNI space. The colours label functional subnetworks separated by neurotransmitter receptor distribution preponderance, here dopamine in yellow and histamine in blue. This forms the basis upon which treatment effect heterogeneity is simulated, with hypothetical treatments selectively effective for lesions disrupting defined receptor territories.

### S9.12.1: *Visual Recognition* subnetwork render

a



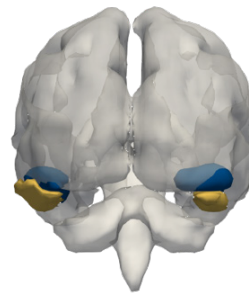
b



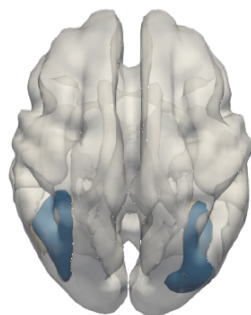
c



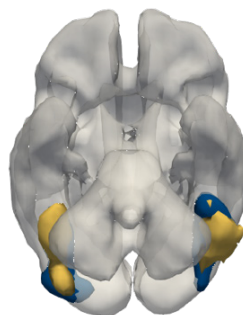
d



e

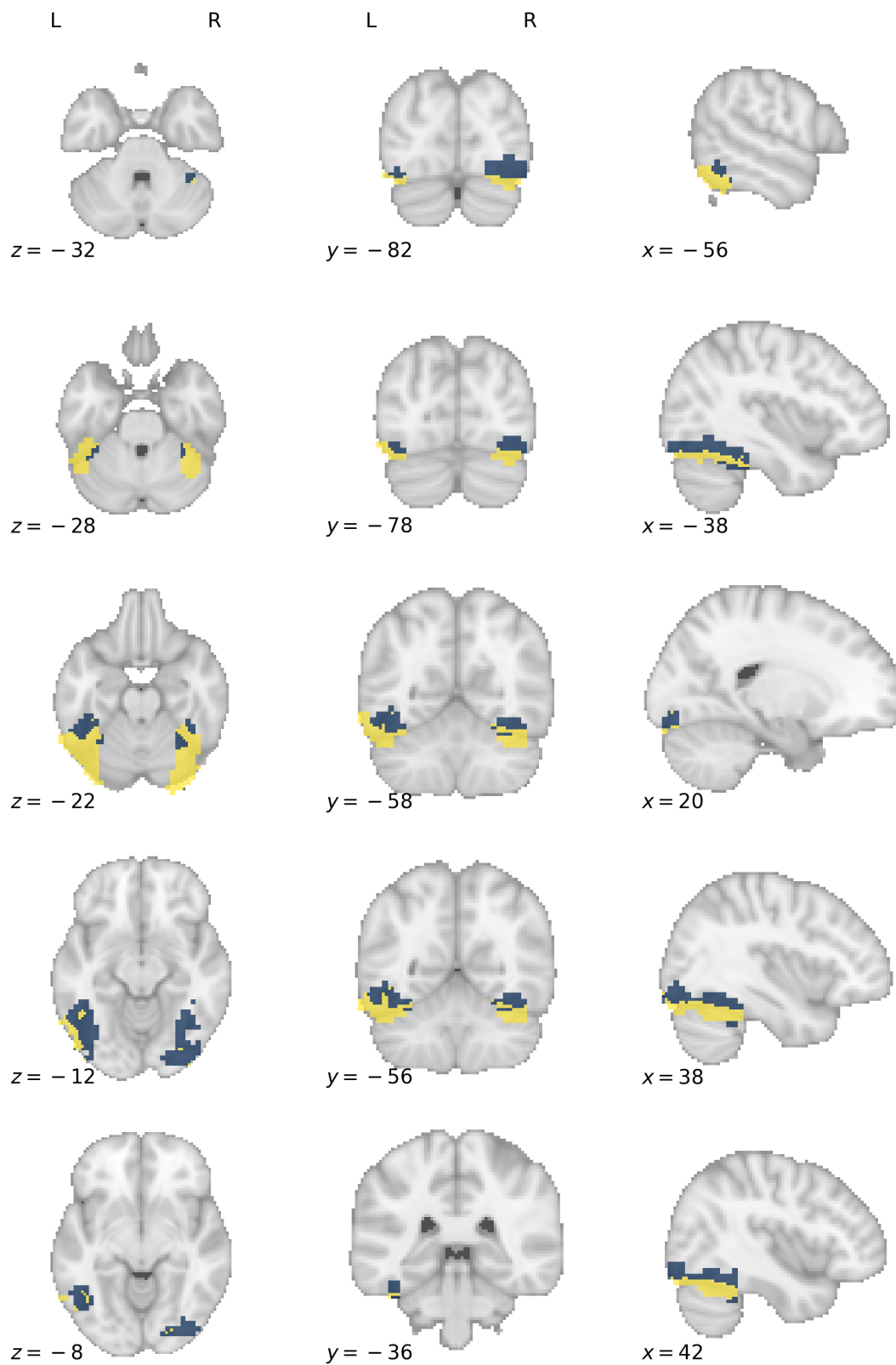


f



Three-dimensional rendering of the functional grey matter network representing *visual recognition*. The colours label functional subnetworks separated by neurotransmitter receptor distribution preponderance, here cannabinoid in yellow and GABA in blue. This forms the basis upon which treatment effect heterogeneity is simulated, with hypothetical treatments selectively effective for lesions disrupting defined receptor territories. Each panel shows the same render from a different spatial perspective: **a**, left; **b**, right; **c**, anterior; **d**, posterior, **e**, superior; **f**, inferior. The underlay is a thresholded white matter template surface in MNI.

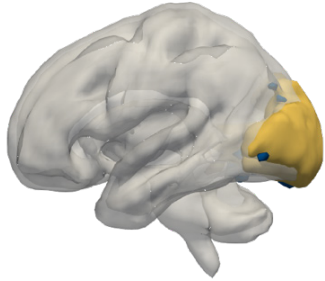
### S9.12.2: *Visual Recognition* subnetwork axial slices



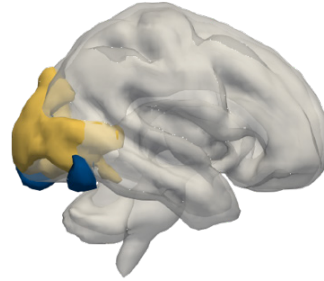
Axial slice visualisation of the functional grey matter network representing *visual recognition*, overlaid onto the standard MNI152 template. The labelled co-ordinates map to MNI space. The colours label functional subnetworks separated by neurotransmitter receptor distribution preponderance, here cannabinoid in yellow and GABA in blue. This forms the basis upon which treatment effect heterogeneity is simulated, with hypothetical treatments selectively effective for lesions disrupting defined receptor territories.

### S9.13.1: *Visual Perception* subnetwork render

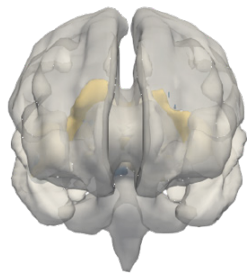
a



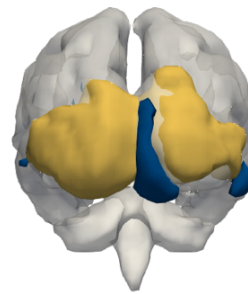
b



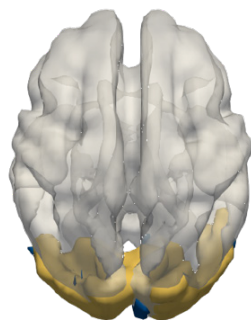
c



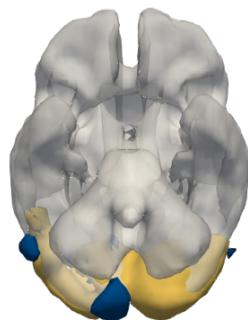
d



e

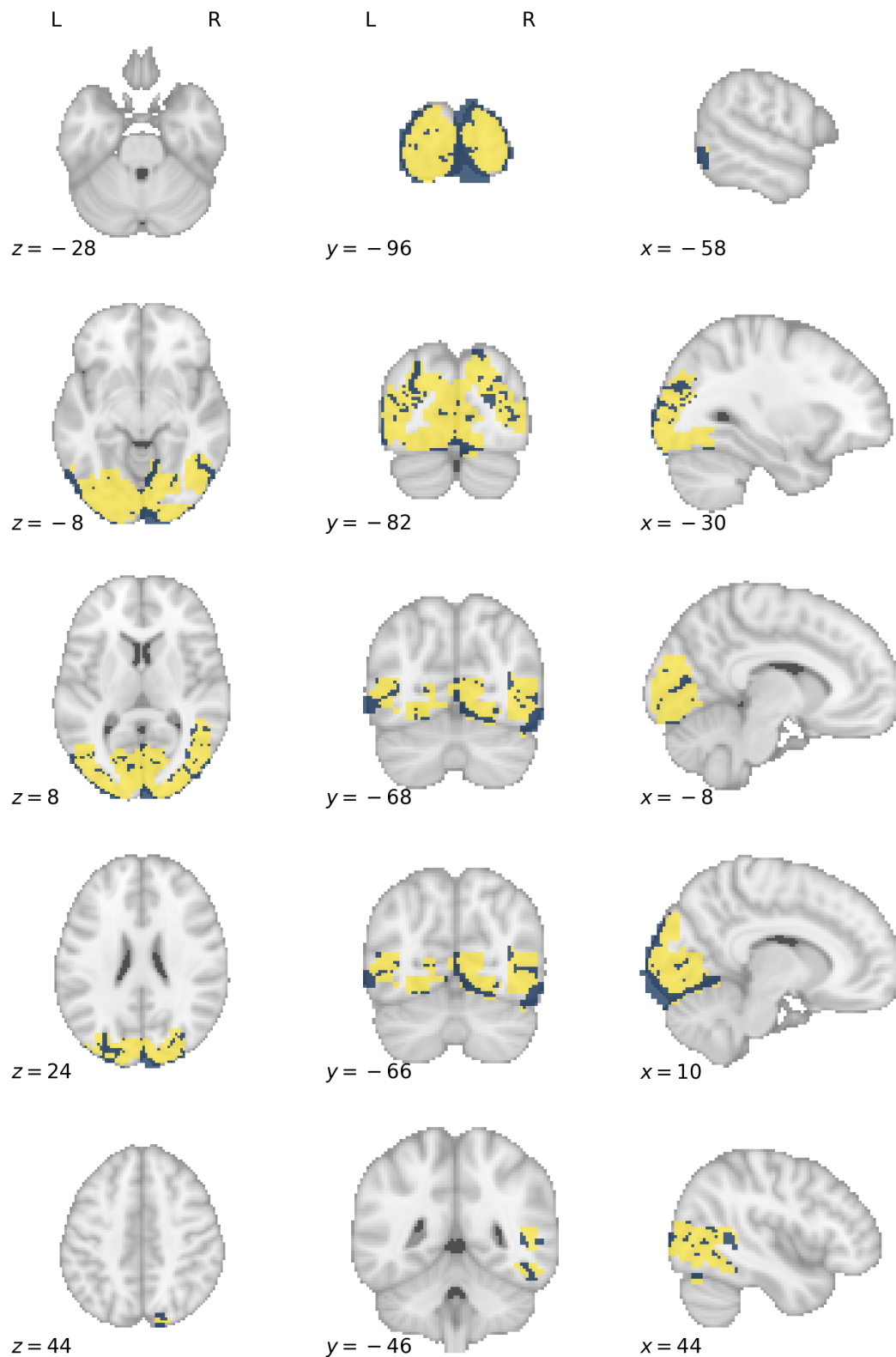


f



Three-dimensional rendering of the functional grey matter network representing *visual perception*. The colours label functional subnetworks separated by neurotransmitter receptor distribution preponderance, here GABA in yellow and 5HT in blue. This forms the basis upon which treatment effect heterogeneity is simulated, with hypothetical treatments selectively effective for lesions disrupting defined receptor territories. Each panel shows the same render from a different spatial perspective: **a**, left; **b**, right; **c**, anterior; **d**, posterior, **e**, superior; **f**, inferior. The underlay is a thresholded white matter template surface in MNI.

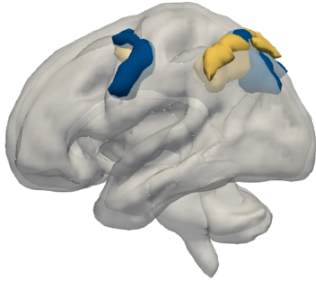
### S9.13.2: *Visual Perception* subnetwork axial slices



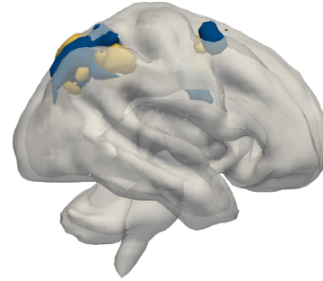
Axial slice visualisation of the functional grey matter network representing *visual perception*, overlaid onto the standard MNI152 template. The labelled co-ordinates map to MNI space. The colours label functional subnetworks separated by neurotransmitter receptor distribution preponderance, here GABA in yellow and 5HT in blue. This forms the basis upon which treatment effect heterogeneity is simulated, with hypothetical treatments selectively effective for lesions disrupting defined receptor territories.

### S9.14.1: *Spatial Reasoning* subnetwork render

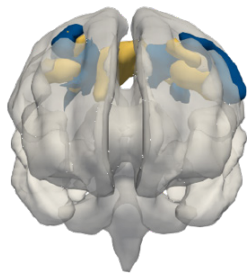
a



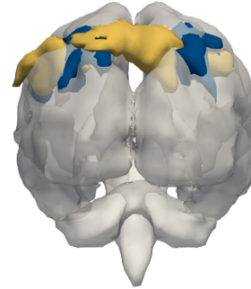
b



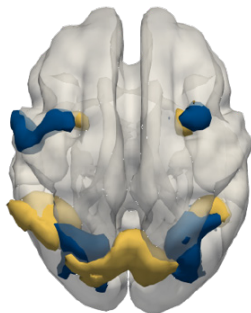
c



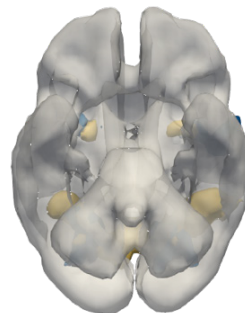
d



e

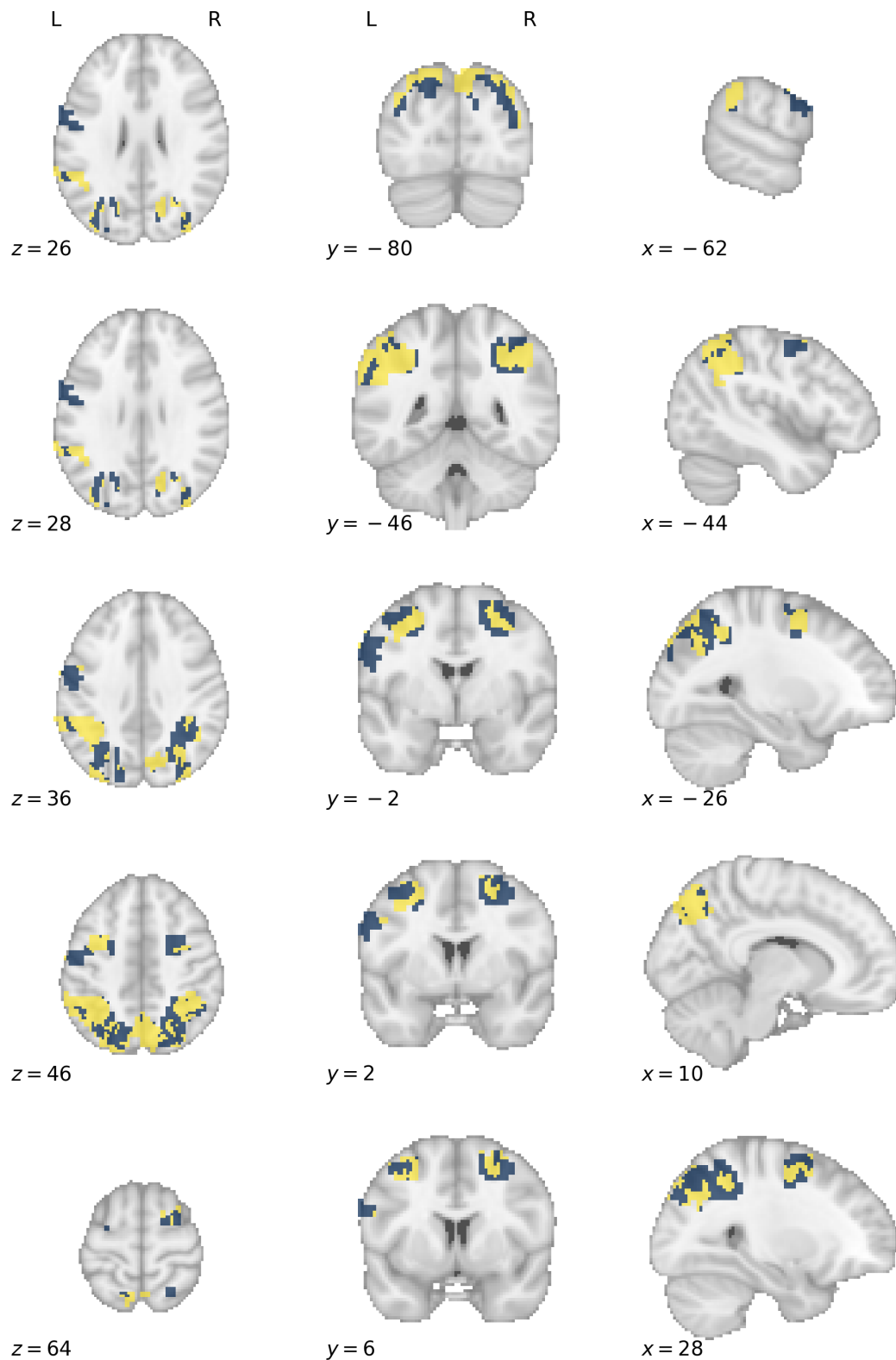


f



Three-dimensional rendering of the functional grey matter network representing *spatial reasoning*. The colours label functional subnetworks separated by neurotransmitter receptor distribution preponderance, here glutamate in yellow and noradrenaline in blue. This forms the basis upon which treatment effect heterogeneity is simulated, with hypothetical treatments selectively effective for lesions disrupting defined receptor territories. Each panel shows the same render from a different spatial perspective: **a**, left; **b**, right; **c**, anterior; **d**, posterior, **e**, superior; **f**, inferior. The underlay is a thresholded white matter template surface in MNI.

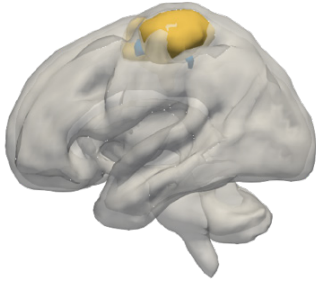
### S9.14.2: *Spatial Reasoning* subnetwork axial slices



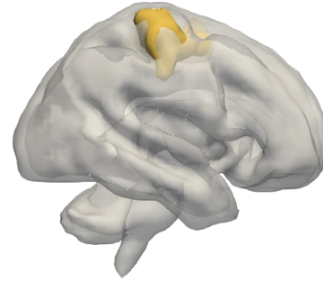
Axial slice visualisation of the functional grey matter network representing *spatial reasoning*, overlaid onto the standard MNI152 template. The labelled co-ordinates map to MNI space. The colours label functional subnetworks separated by neurotransmitter receptor distribution preponderance, here glutamate in yellow and noradrenaline in blue. This forms the basis upon which treatment effect heterogeneity is simulated, with hypothetical treatments selectively effective for lesions disrupting defined receptor territories.

### S9.15.1: *Motor* subnetwork render

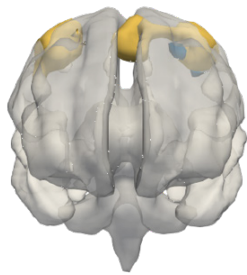
**a**



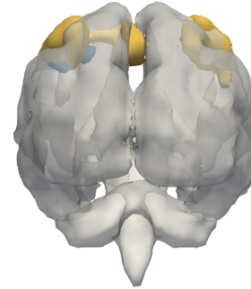
**b**



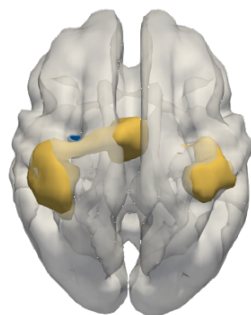
**c**



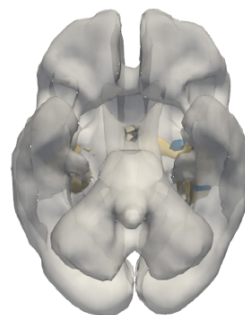
**d**



**e**

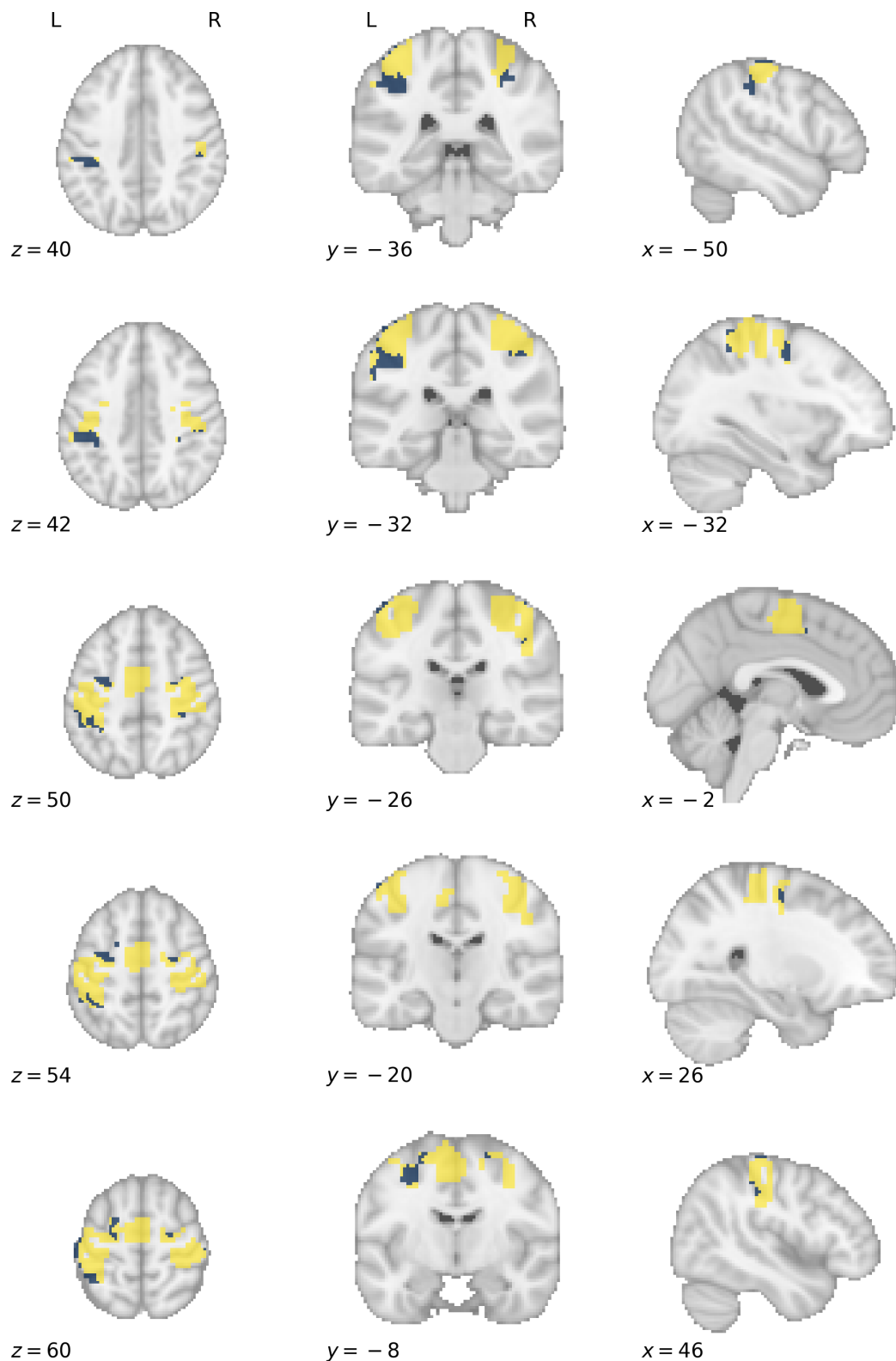


**f**



Three-dimensional rendering of the functional grey matter network representing *motor behaviour*. The colours label functional subnetworks separated by neurotransmitter receptor distribution preponderance, here noradrenaline in yellow and glutamate in blue. This forms the basis upon which treatment effect heterogeneity is simulated, with hypothetical treatments selectively effective for lesions disrupting defined receptor territories. Each panel shows the same render from a different spatial perspective: **a**, left; **b**, right; **c**, anterior; **d**, posterior; **e**, superior; **f**, inferior. The underlay is a thresholded white matter template surface in MNI.

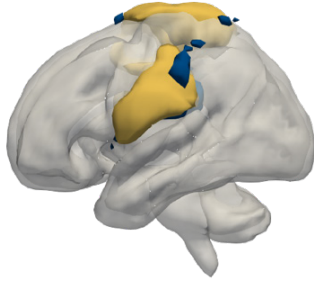
### S9.15.2: *Motor* subnetwork axial slices



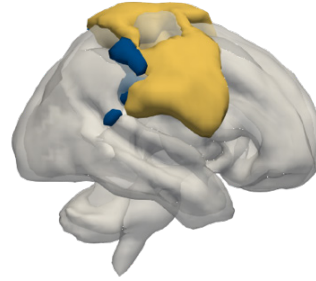
Axial slice visualisation of the functional grey matter network representing *motor behaviour*, overlaid onto the standard MNI152 template. The labelled co-ordinates map to MNI space. The colours label functional subnetworks separated by neurotransmitter receptor distribution preponderance, here noradrenaline in yellow and glutamate in blue. This forms the basis upon which treatment effect heterogeneity is simulated, with hypothetical treatments selectively effective for lesions disrupting defined receptor territories.

### S9.16.1: *Somatosensory* subnetwork render

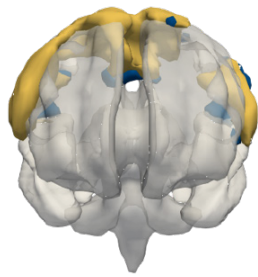
a



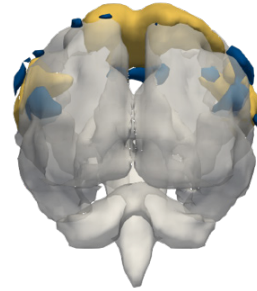
b



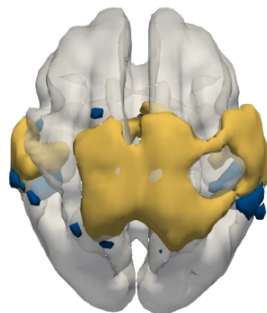
c



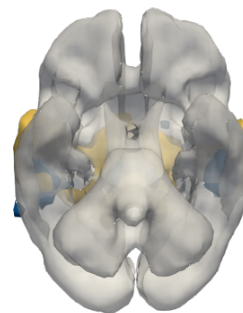
d



e

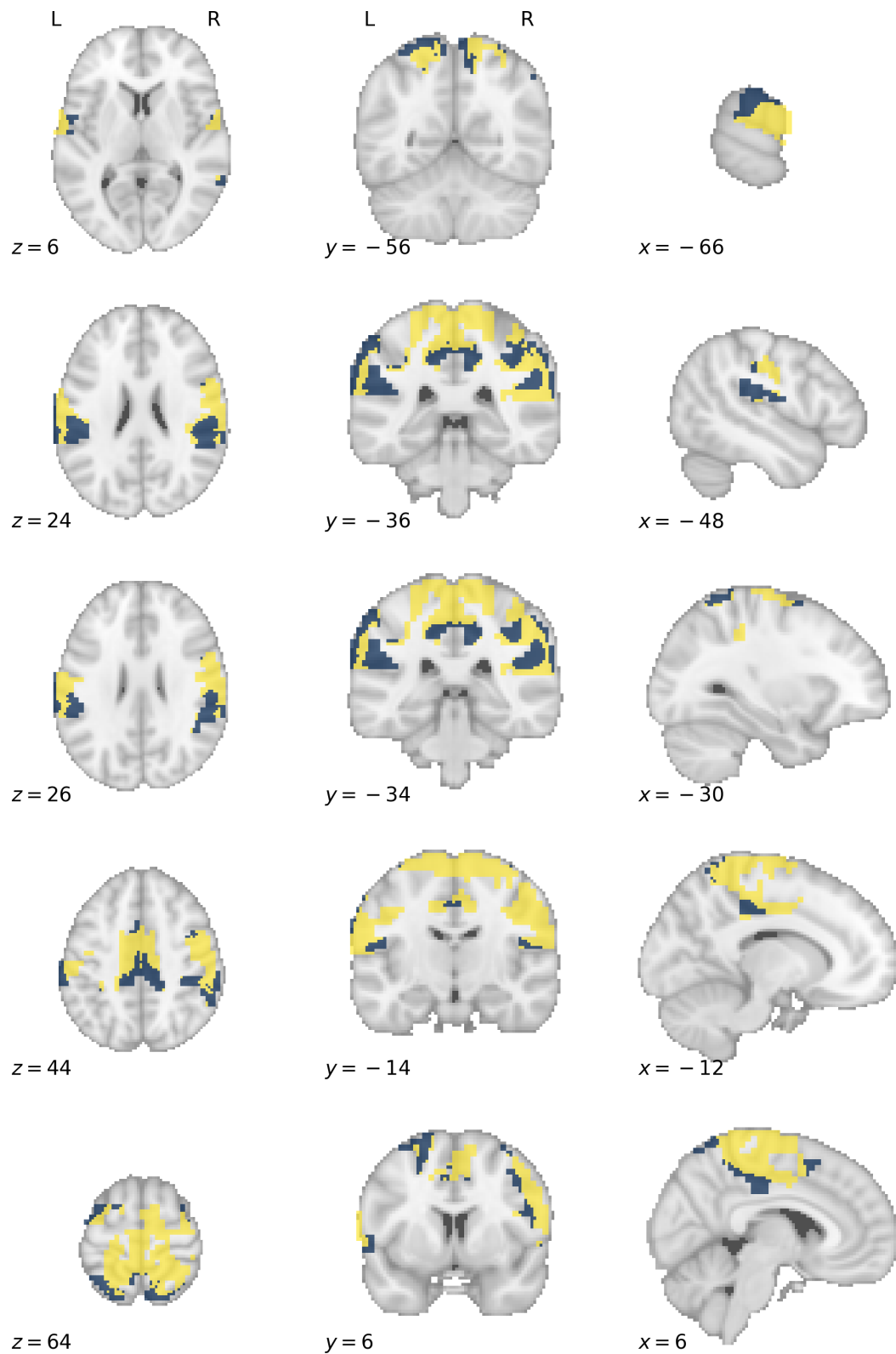


f



Three-dimensional rendering of the functional grey matter network representing *somatosensory function*. The colours label functional subnetworks separated by neurotransmitter receptor distribution preponderance, here noradrenaline in yellow and glutamate in blue. This forms the basis upon which treatment effect heterogeneity is simulated, with hypothetical treatments selectively effective for lesions disrupting defined receptor territories. Each panel shows the same render from a different spatial perspective: **a**, left; **b**, right; **c**, anterior; **d**, posterior, **e**, superior; **f**, inferior. The underlay is a thresholded white matter template surface in MNI.

### S9.16.2: Somatosensory subnetwork axial slices



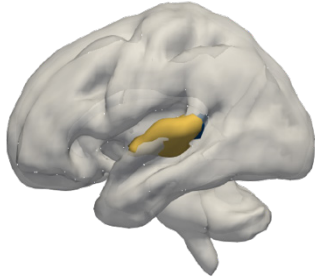
Axial slice visualisation of the functional grey matter network representing *somatosensory function*, overlaid onto the standard MNI152 template. The labelled co-ordinates map to MNI space. The colours label functional subnetworks separated by neurotransmitter receptor distribution preponderance, here noradrenaline in yellow and glutamate in blue. This forms the basis upon which treatment effect heterogeneity is simulated, with hypothetical treatments selectively effective for lesions disrupting defined receptor territories.

## S10: Transcriptome subnetworks

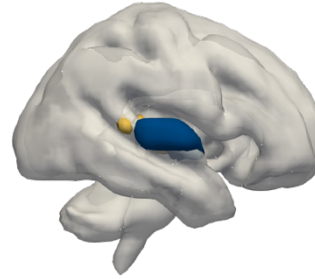
The following figures show, for each functional network, divisions into two subnetworks based on agglomerative clustering of microarray gene expression data (Hawrylycz et al., 2012). The assignment of unlabelled voxels was guided by the three-dimensional Gaussian distributions of the labelled voxels as described in the Methods section of the paper.

### S10.1.1: *Hearing* subnetwork render

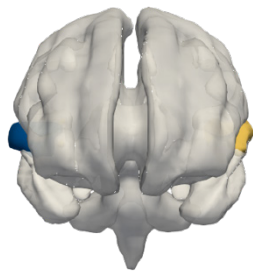
a



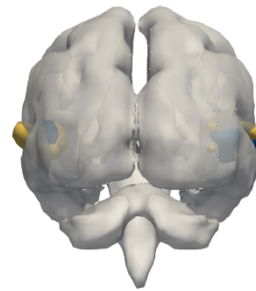
b



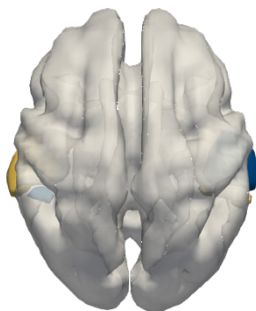
c



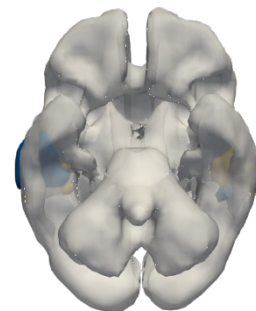
d



e

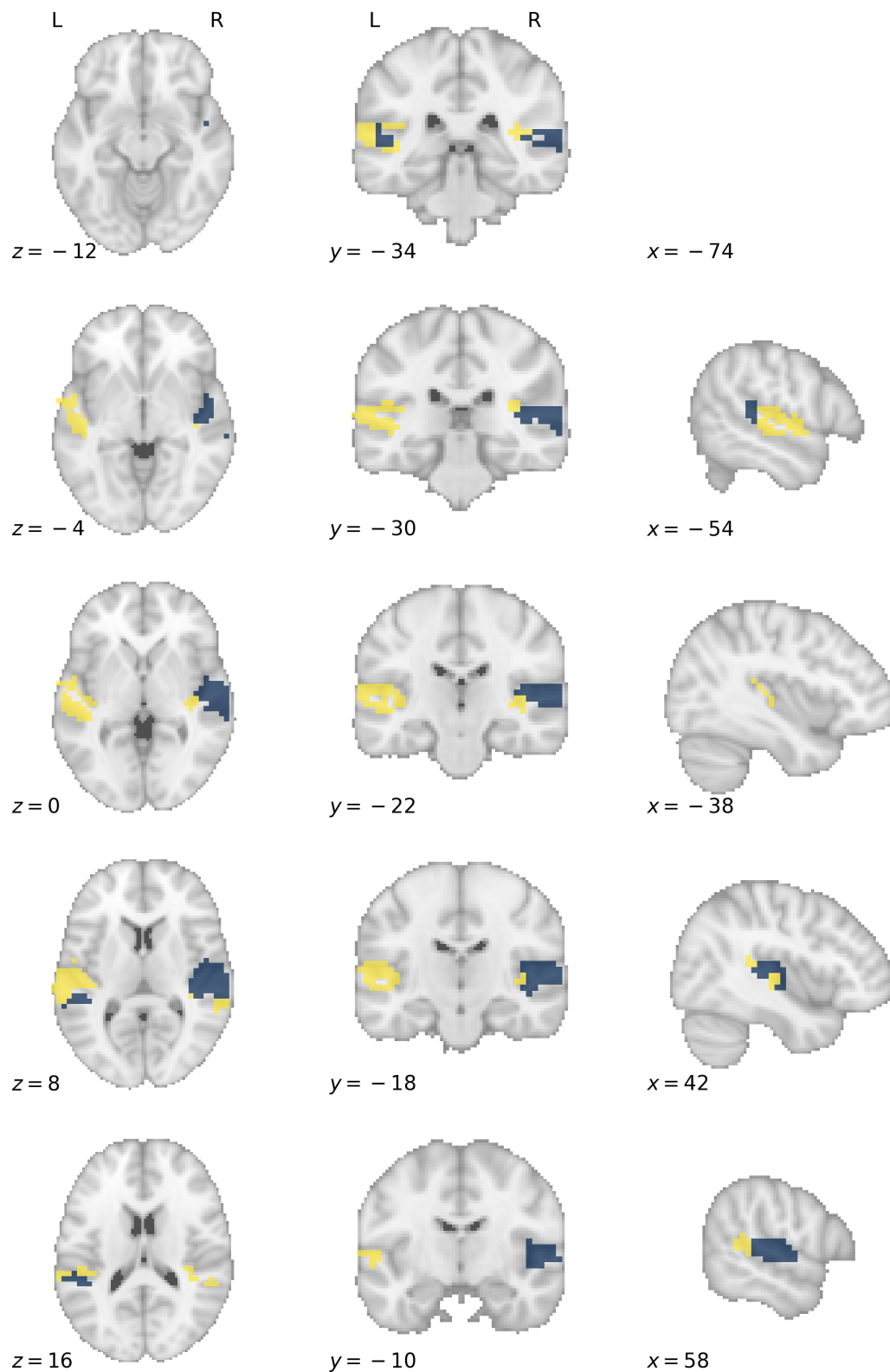


f



Three-dimensional rendering of the functional grey matter network representing *hearing*. The colours label functional subnetworks separated by microarray gene expression data, here represented in yellow and blue. This forms the basis upon which treatment effect heterogeneity is simulated, with hypothetical treatments selectively effective for lesions disrupting defined subnetworks. Each panel shows the same render from a different spatial perspective: **a**, left; **b**, right; **c**, anterior; **d**, posterior, **e**, superior; **f**, inferior.

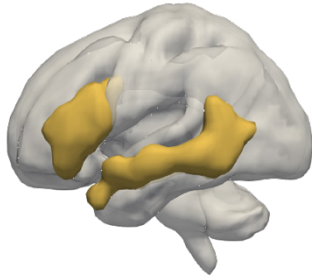
### S10.1.2: *Hearing* subnetwork axial slices



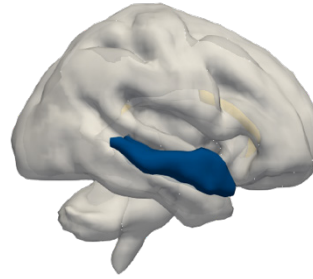
Axial slice visualisation of the functional grey matter network representing *hearing*, overlaid onto the standard MNI152 template. The labelled co-ordinates map to MNI space. The colours label functional subnetworks separated by microarray gene expression, here represented in yellow and blue. This forms the basis upon which treatment effect heterogeneity is simulated, with hypothetical treatments selectively effective for lesions disrupting defined subnetworks.

### S10.2.1: *Language* subnetwork render

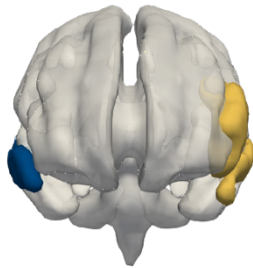
a



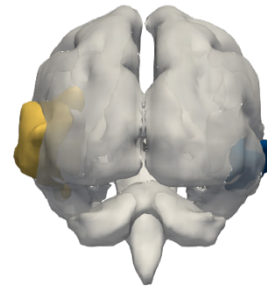
b



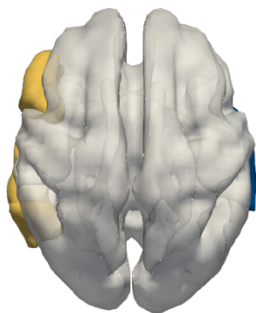
c



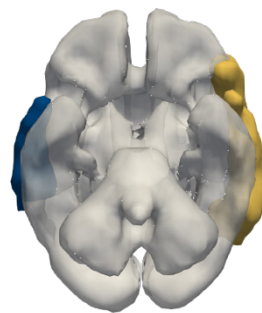
d



e

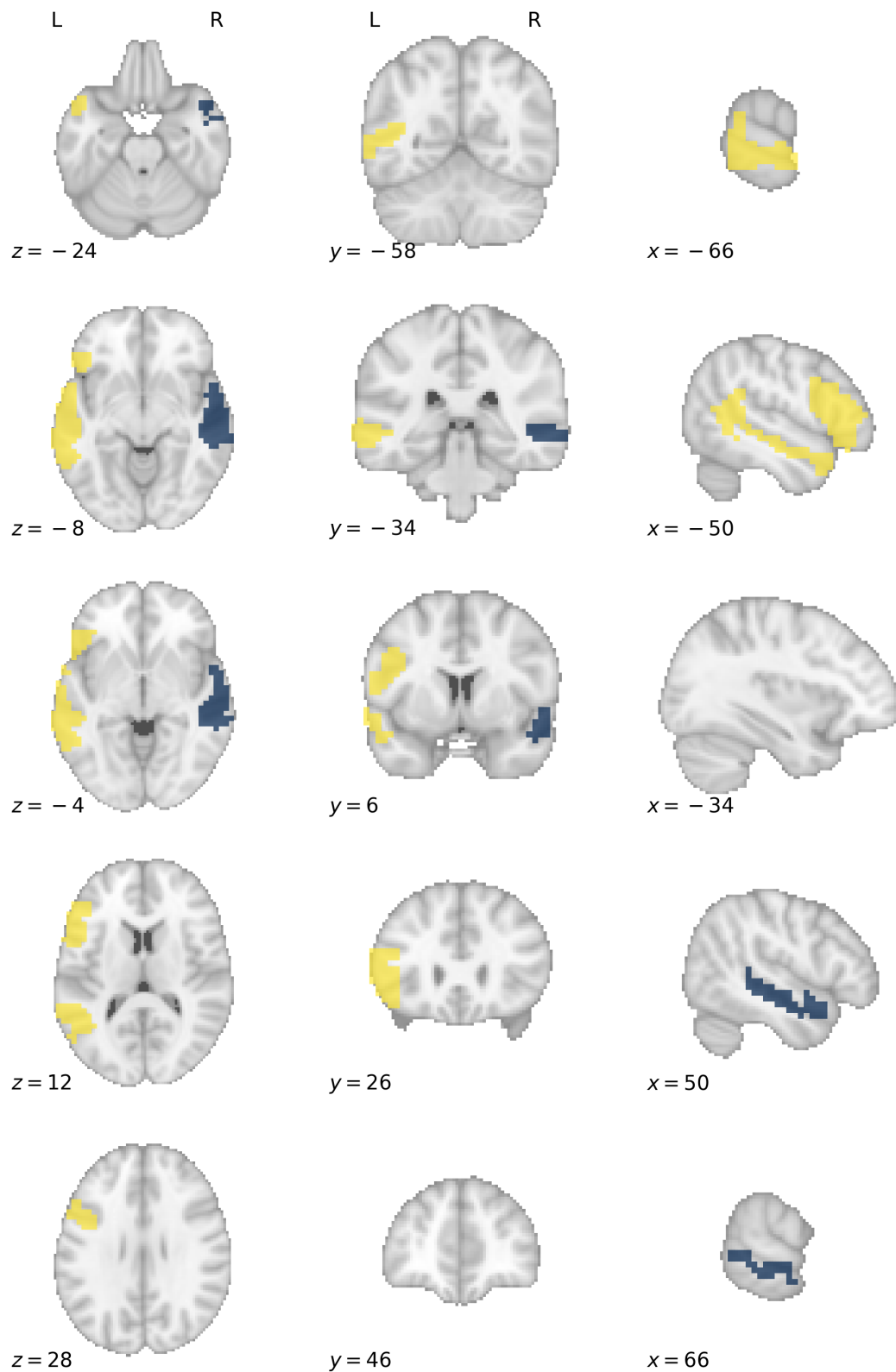


f



Three-dimensional rendering of the functional grey matter network representing *language*. The colours label functional subnetworks separated by microarray gene expression data, here represented in yellow and blue. This forms the basis upon which treatment effect heterogeneity is simulated, with hypothetical treatments selectively effective for lesions disrupting defined subnetworks. Each panel shows the same render from a different spatial perspective: **a**, left; **b**, right; **c**, anterior; **d**, posterior, **e**, superior; **f**, inferior.

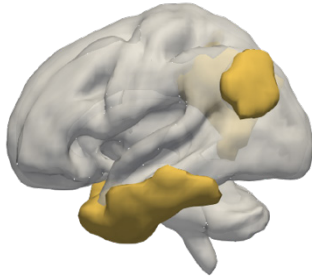
### S10.2.2: *Language* subnetwork axial slices



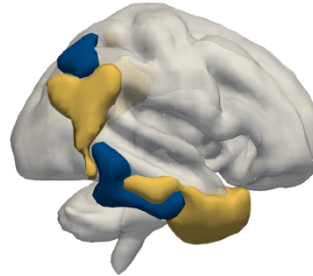
Axial slice visualisation of the functional grey matter network representing *language*, overlaid onto the standard MNI152 template. The labelled co-ordinates map to MNI space. The colours label functional subnetworks separated by microarray gene expression, here represented in yellow and blue. This forms the basis upon which treatment effect heterogeneity is simulated, with hypothetical treatments selectively effective for lesions disrupting defined subnetworks.

### S10.3.1: *Introspection* subnetwork render

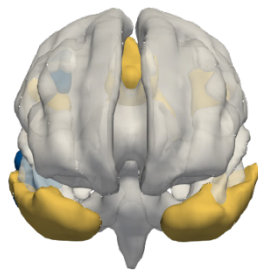
a



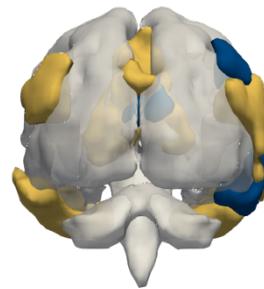
b



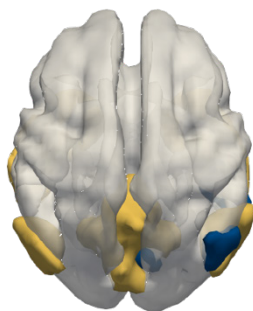
c



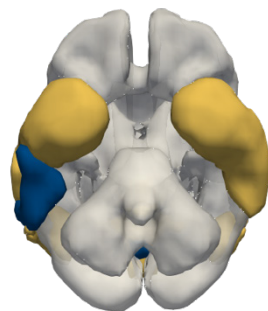
d



e

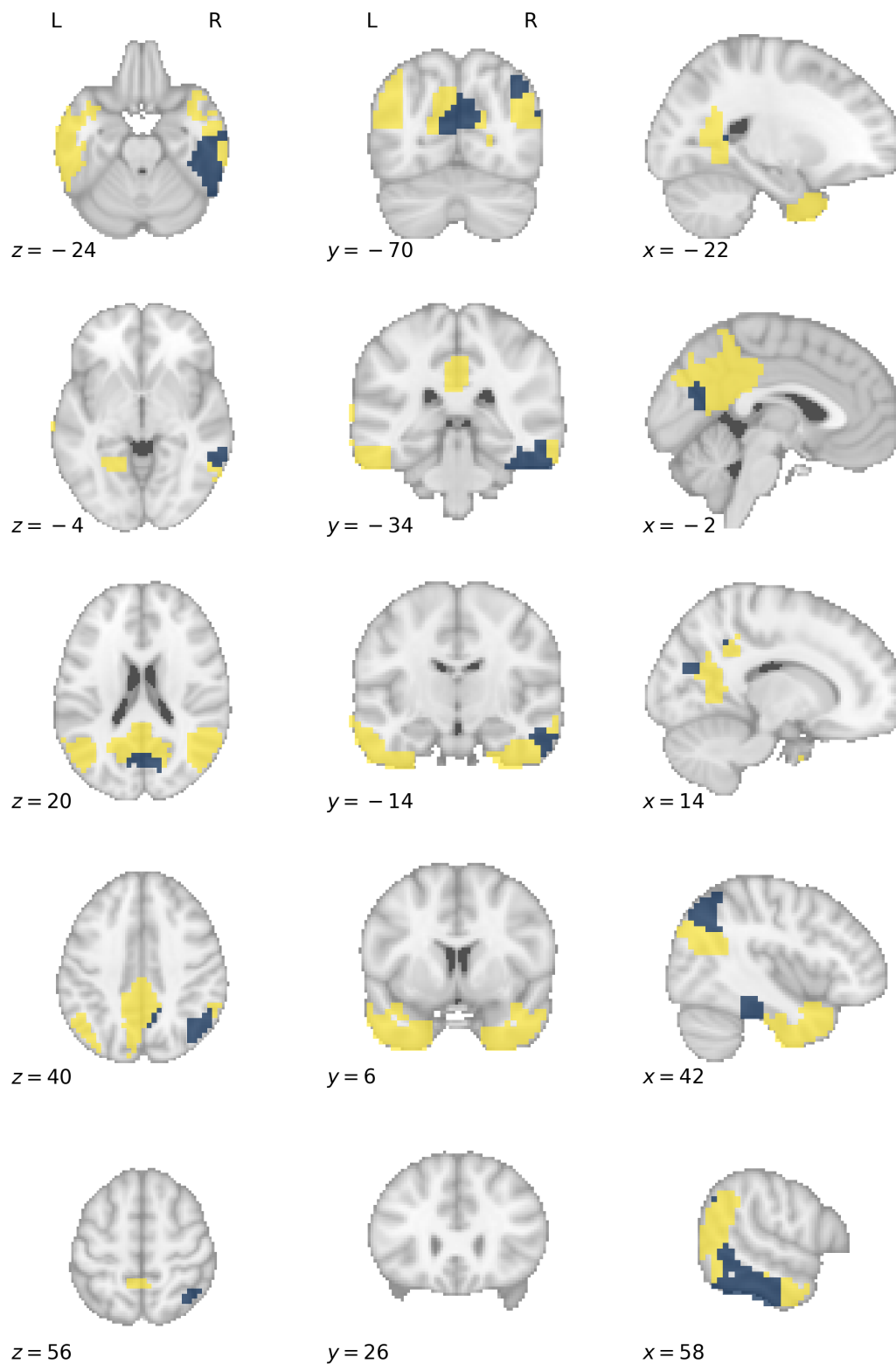


f



Three-dimensional rendering of the functional grey matter network representing *introspection*. The colours label functional subnetworks separated by microarray gene expression data, here represented in yellow and blue. This forms the basis upon which treatment effect heterogeneity is simulated, with hypothetical treatments selectively effective for lesions disrupting defined subnetworks. Each panel shows the same render from a different spatial perspective: **a**, left; **b**, right; **c**, anterior; **d**, posterior, **e**, superior; **f**, inferior.

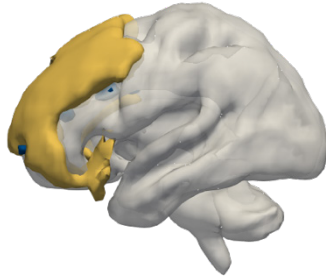
### S10.3.2: *Introspection* subnetwork axial slices



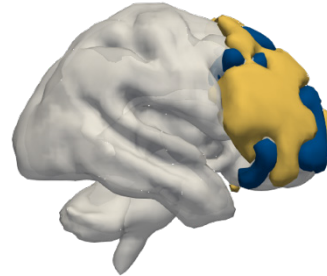
Axial slice visualisation of the functional grey matter network representing *introspection*, overlaid onto the standard MNI152 template. The labelled co-ordinates map to MNI space. The colours label functional subnetworks separated by microarray gene expression, here represented in yellow and blue. This forms the basis upon which treatment effect heterogeneity is simulated, with hypothetical treatments selectively effective for lesions disrupting defined subnetworks.

### S10.4.1: *Cognition* subnetwork render

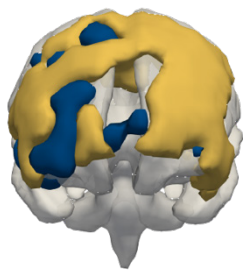
a



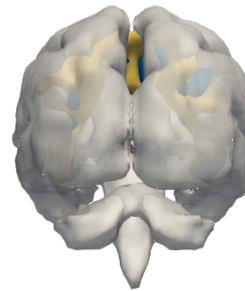
b



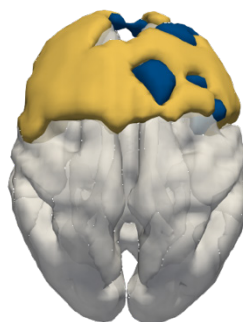
c



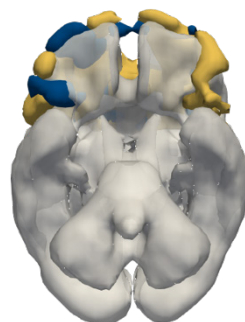
d



e

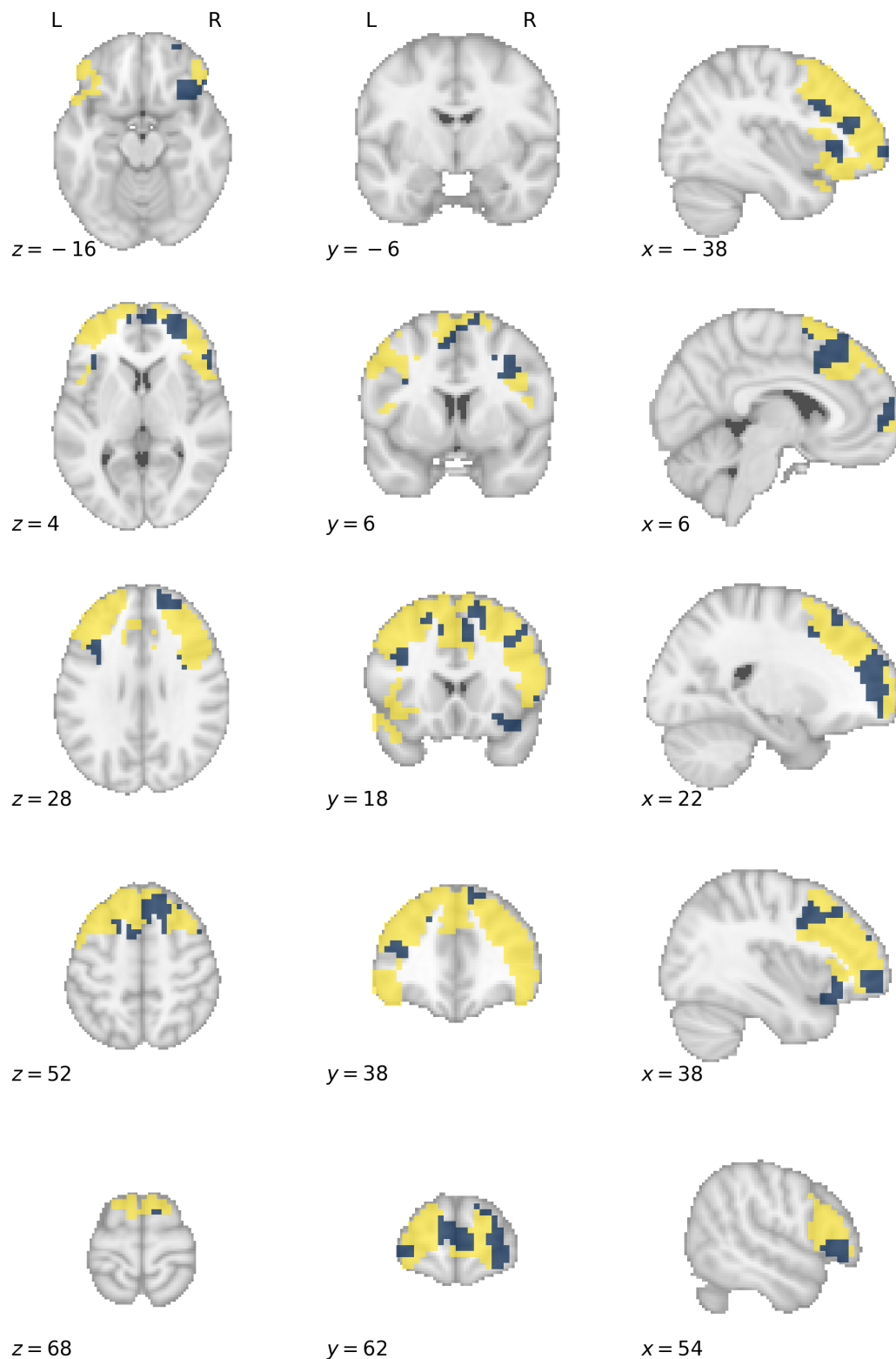


f



Three-dimensional rendering of the functional grey matter network representing *cognition*. The colours label functional subnetworks separated by microarray gene expression data, here represented in yellow and blue. This forms the basis upon which treatment effect heterogeneity is simulated, with hypothetical treatments selectively effective for lesions disrupting defined subnetworks. Each panel shows the same render from a different spatial perspective: **a**, left; **b**, right; **c**, anterior; **d**, posterior, **e**, superior; **f**, inferior.

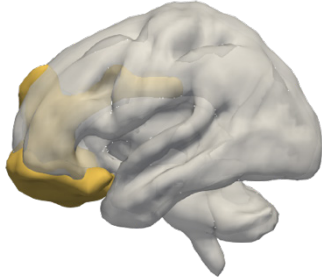
### S10.4.2: *Cognition* subnetwork axial slices



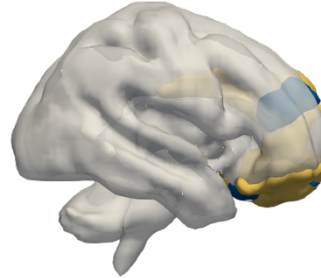
Axial slice visualisation of the functional grey matter network representing *cognition*, overlaid onto the standard MNI152 template. The labelled co-ordinates map to MNI space. The colours label functional subnetworks separated by microarray gene expression, here represented in yellow and blue. This forms the basis upon which treatment effect heterogeneity is simulated, with hypothetical treatments selectively effective for lesions disrupting defined subnetworks.

### S10.5.1: *Mood* subnetwork render

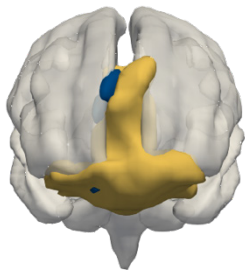
a



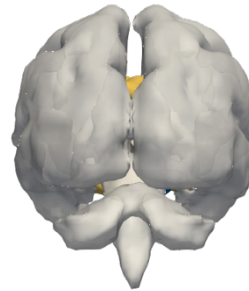
b



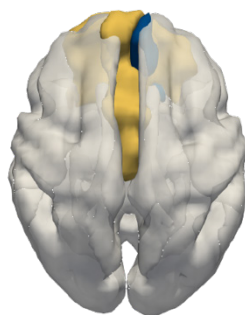
c



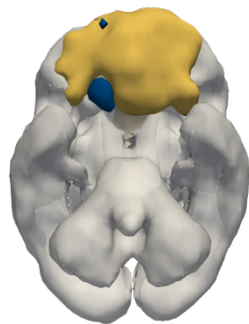
d



e

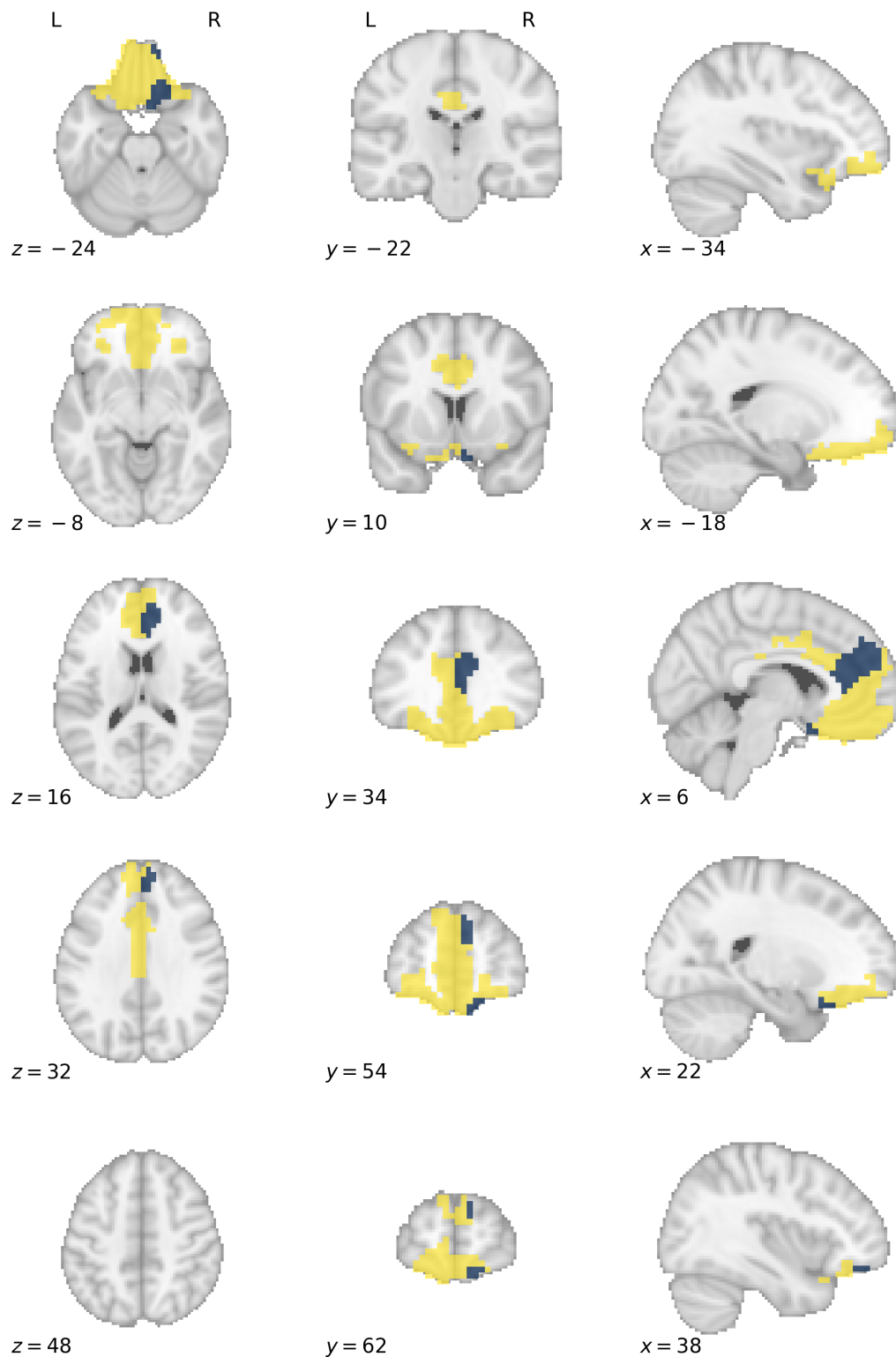


f



Three-dimensional rendering of the functional grey matter network representing *mood*. The colours label functional subnetworks separated by microarray gene expression data, here represented in yellow and blue. This forms the basis upon which treatment effect heterogeneity is simulated, with hypothetical treatments selectively effective for lesions disrupting defined subnetworks. Each panel shows the same render from a different spatial perspective: **a**, left; **b**, right; **c**, anterior; **d**, posterior, **e**, superior; **f**, inferior.

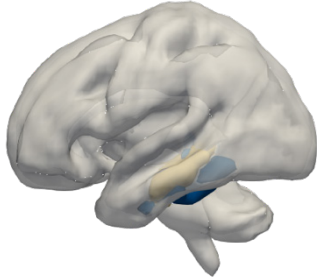
### S10.5.2: *Mood* subnetwork axial slices



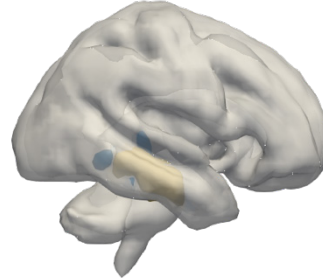
Axial slice visualisation of the functional grey matter network representing *mood*, overlaid onto the standard MNI152 template. The labelled co-ordinates map to MNI space. The colours label functional subnetworks separated by microarray gene expression, here represented in yellow and blue. This forms the basis upon which treatment effect heterogeneity is simulated, with hypothetical treatments selectively effective for lesions disrupting defined subnetworks.

### S10.6.1: *Memory* subnetwork render

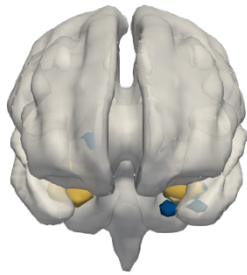
**a**



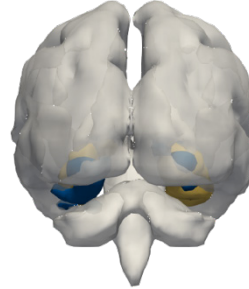
**b**



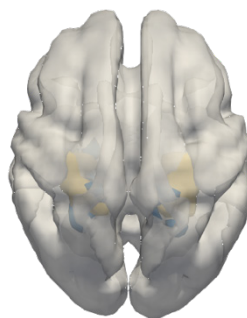
**c**



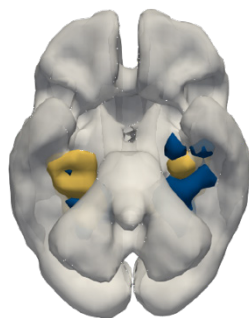
**d**



**e**

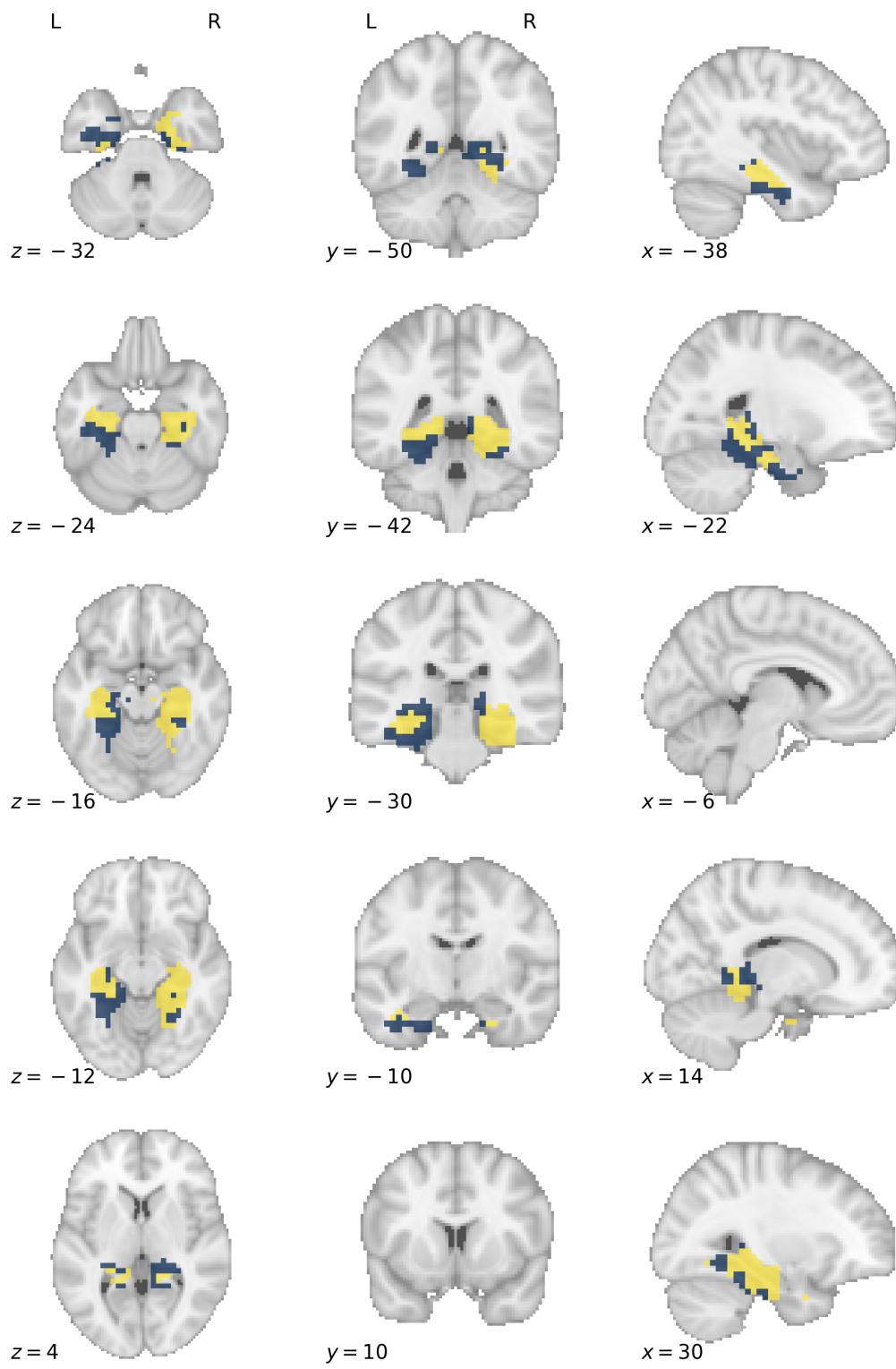


**f**



Three-dimensional rendering of the functional grey matter network representing *memory*. The colours label functional subnetworks separated by microarray gene expression data, here represented in yellow and blue. This forms the basis upon which treatment effect heterogeneity is simulated, with hypothetical treatments selectively effective for lesions disrupting defined subnetworks. Each panel shows the same render from a different spatial perspective: **a**, left; **b**, right; **c**, anterior; **d**, posterior; **e**, superior; **f**, inferior.

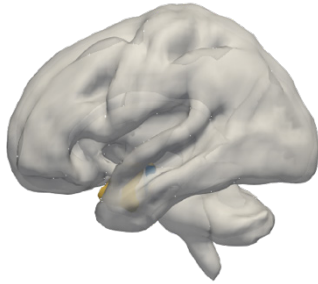
### S10.6.2: *Memory* subnetwork axial slices



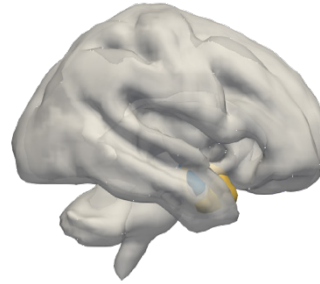
Axial slice visualisation of the functional grey matter network representing *memory*, overlaid onto the standard MNI152 template. The labelled co-ordinates map to MNI space. The colours label functional subnetworks separated by microarray gene expression, here represented in yellow and blue. This forms the basis upon which treatment effect heterogeneity is simulated, with hypothetical treatments selectively effective for lesions disrupting defined subnetworks.

### S10.7.1: *Aversion* subnetwork render

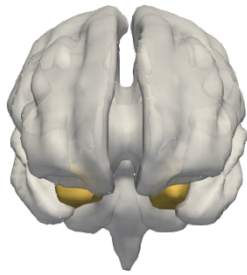
**a**



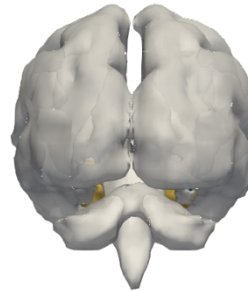
**b**



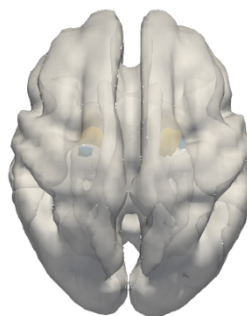
**c**



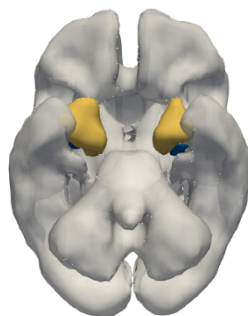
**d**



**e**

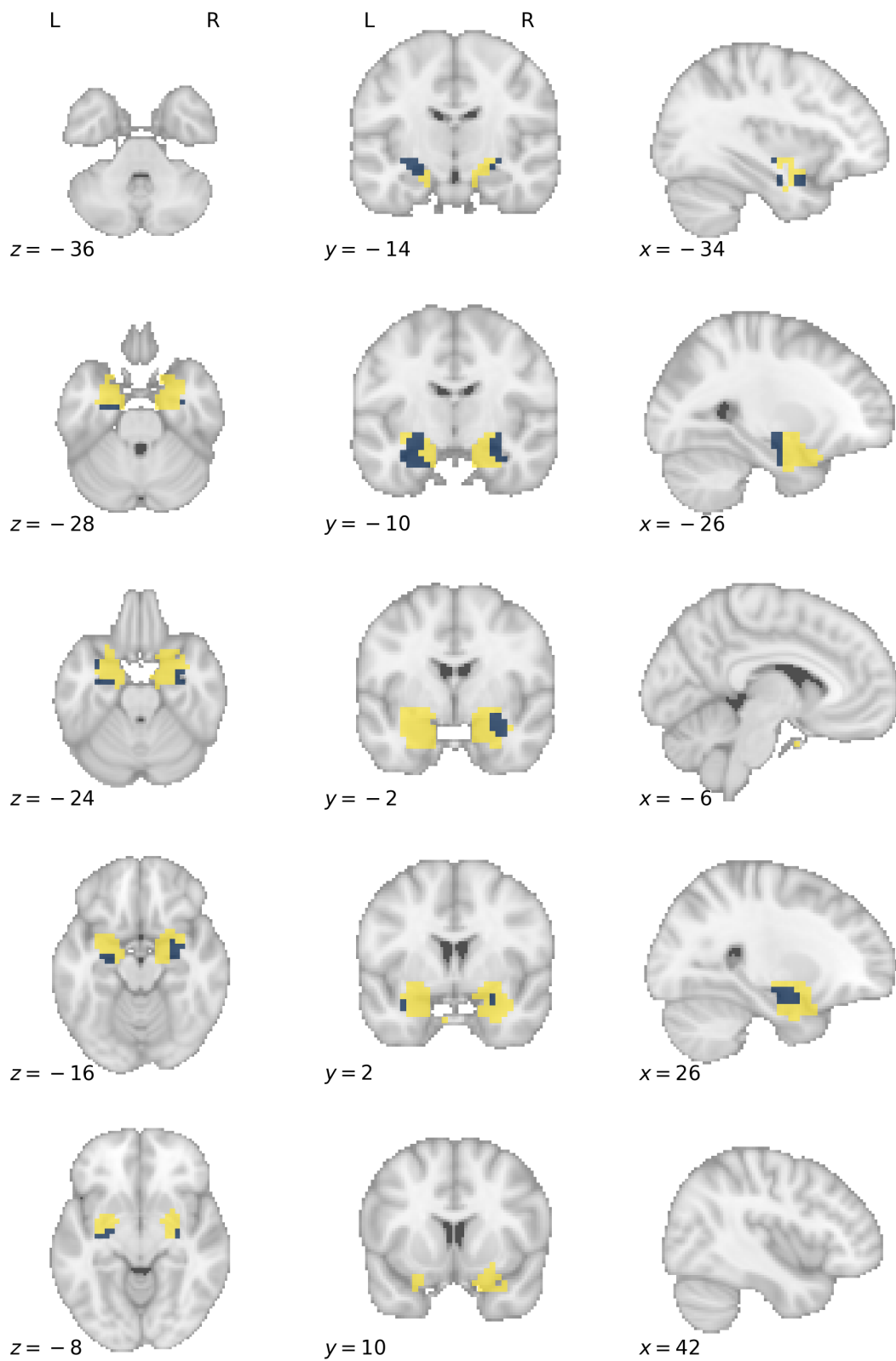


**f**



Three-dimensional rendering of the functional grey matter network representing *aversion*. The colours label functional subnetworks separated by microarray gene expression data, here represented in yellow and blue. This forms the basis upon which treatment effect heterogeneity is simulated, with hypothetical treatments selectively effective for lesions disrupting defined subnetworks. Each panel shows the same render from a different spatial perspective: **a**, left; **b**, right; **c**, anterior; **d**, posterior; **e**, superior; **f**, inferior.

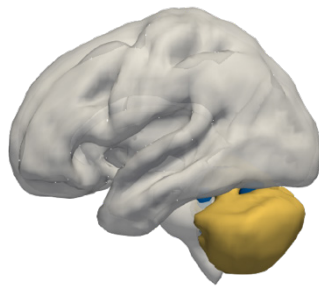
### S10.7.2: *Aversion* subnetwork axial slices



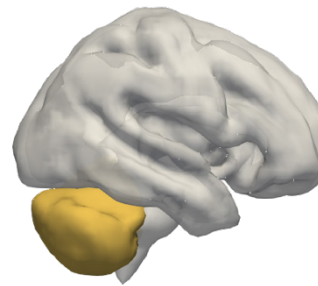
Axial slice visualisation of the functional grey matter network representing *aversion*, overlaid onto the standard MNI152 template. The labelled co-ordinates map to MNI space. The colours label functional subnetworks separated by microarray gene expression, here represented in yellow and blue. This forms the basis upon which treatment effect heterogeneity is simulated, with hypothetical treatments selectively effective for lesions disrupting defined subnetworks.

### S10.8.1: *Coordination* subnetwork render

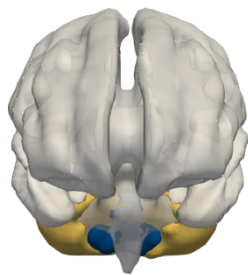
a



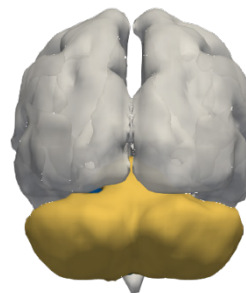
b



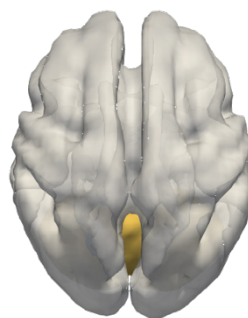
c



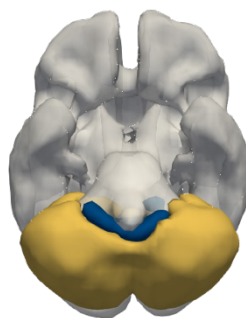
d



e

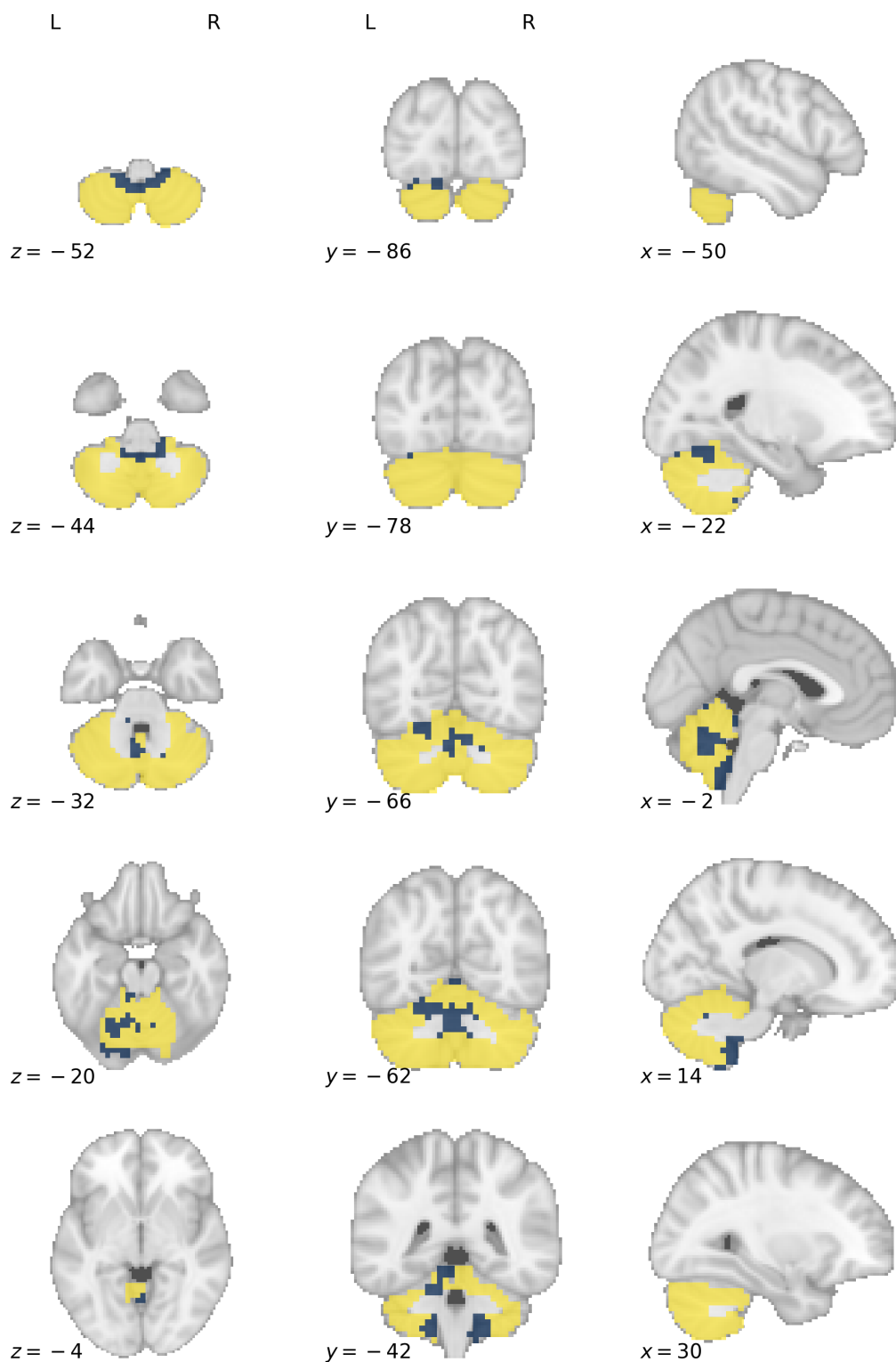


f



Three-dimensional rendering of the functional grey matter network representing *coordination*. The colours label functional subnetworks separated by microarray gene expression data, here represented in yellow and blue. This forms the basis upon which treatment effect heterogeneity is simulated, with hypothetical treatments selectively effective for lesions disrupting defined subnetworks. Each panel shows the same render from a different spatial perspective: **a**, left; **b**, right; **c**, anterior; **d**, posterior; **e**, superior; **f**, inferior.

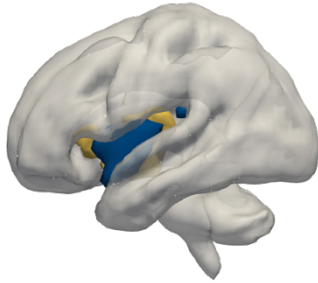
## S10.8.2: *Coordination* subnetwork axial slices



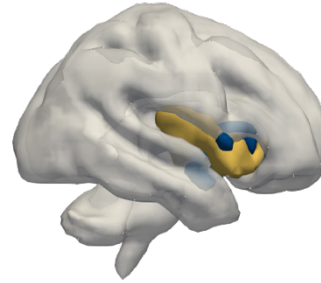
Axial slice visualisation of the functional grey matter network representing *coordination*, overlaid onto the standard MNI152 template. The labelled co-ordinates map to MNI space. The colours label functional subnetworks separated by microarray gene expression, here represented in yellow and blue. This forms the basis upon which treatment effect heterogeneity is simulated, with hypothetical treatments selectively effective for lesions disrupting defined subnetworks.

### S10.9.1: *Interoception* subnetwork render

a



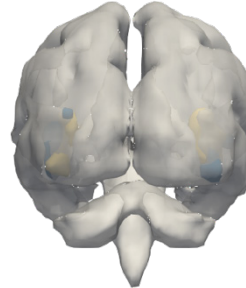
b



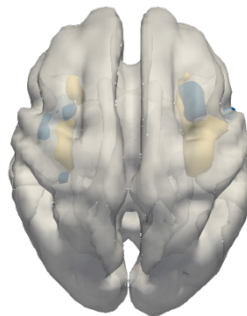
c



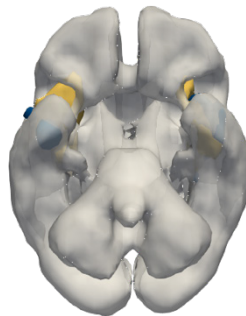
d



e

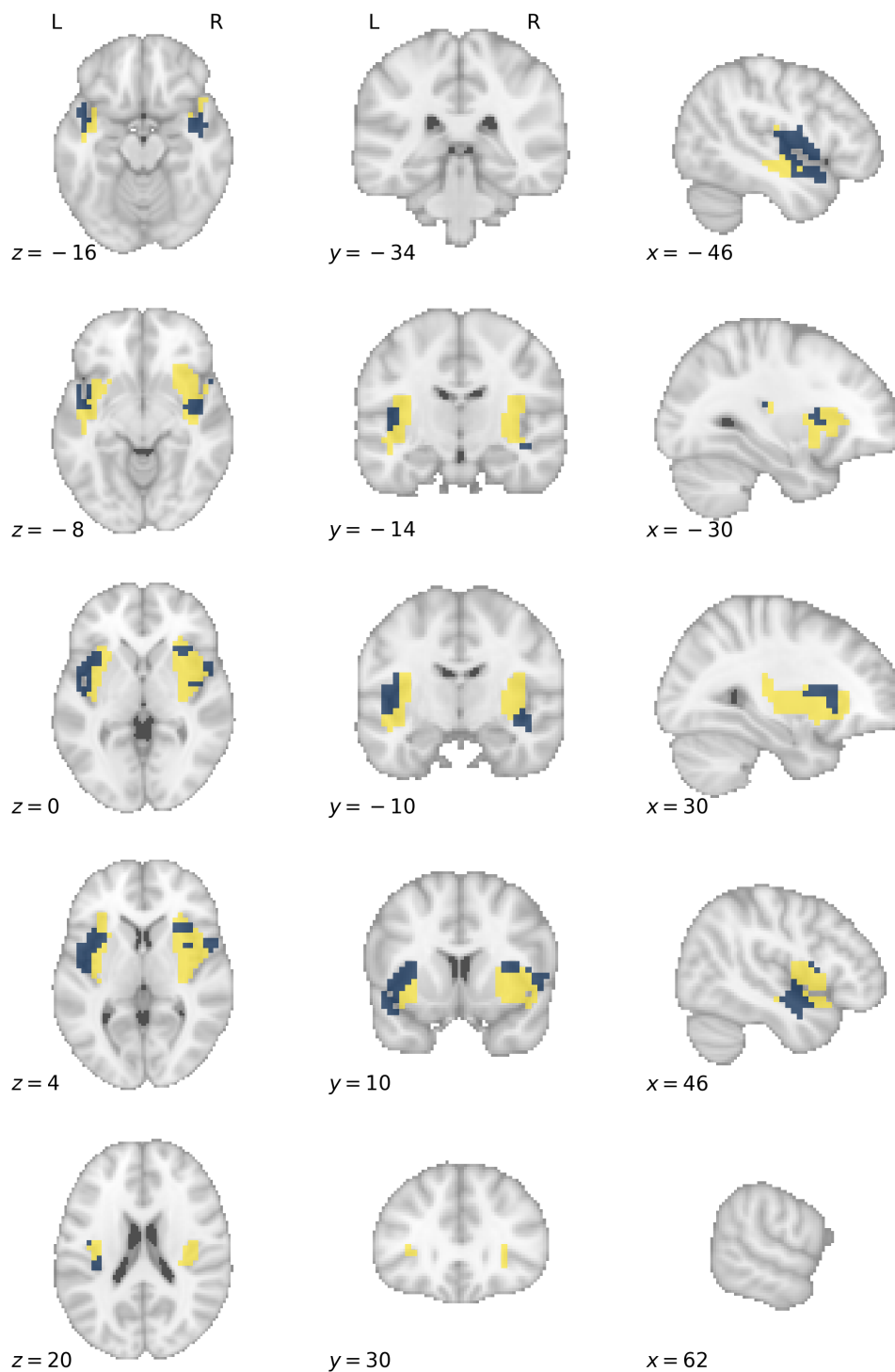


f



Three-dimensional rendering of the functional grey matter network representing *interoception*. The colours label functional subnetworks separated by microarray gene expression data, here represented in yellow and blue. This forms the basis upon which treatment effect heterogeneity is simulated, with hypothetical treatments selectively effective for lesions disrupting defined subnetworks. Each panel shows the same render from a different spatial perspective: **a**, left; **b**, right; **c**, anterior; **d**, posterior; **e**, superior; **f**, inferior.

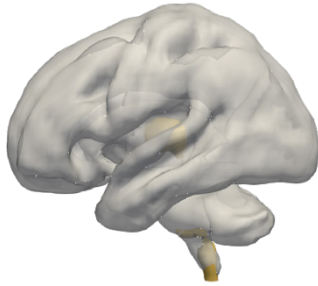
### S10.9.2: *Interoception* subnetwork axial slices



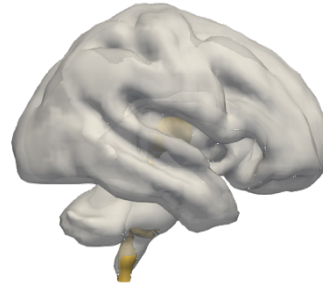
Axial slice visualisation of the functional grey matter network representing *interoception*, overlaid onto the standard MNI152 template. The labelled co-ordinates map to MNI space. The colours label functional subnetworks separated by microarray gene expression, here represented in yellow and blue. This forms the basis upon which treatment effect heterogeneity is simulated, with hypothetical treatments selectively effective for lesions disrupting defined subnetworks.

### S10.10.1: *Sleep* subnetwork render

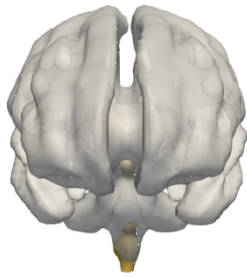
**a**



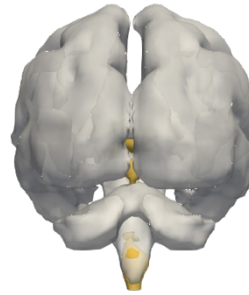
**b**



**c**



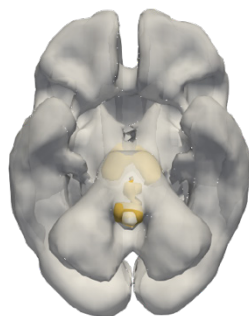
**d**



**e**

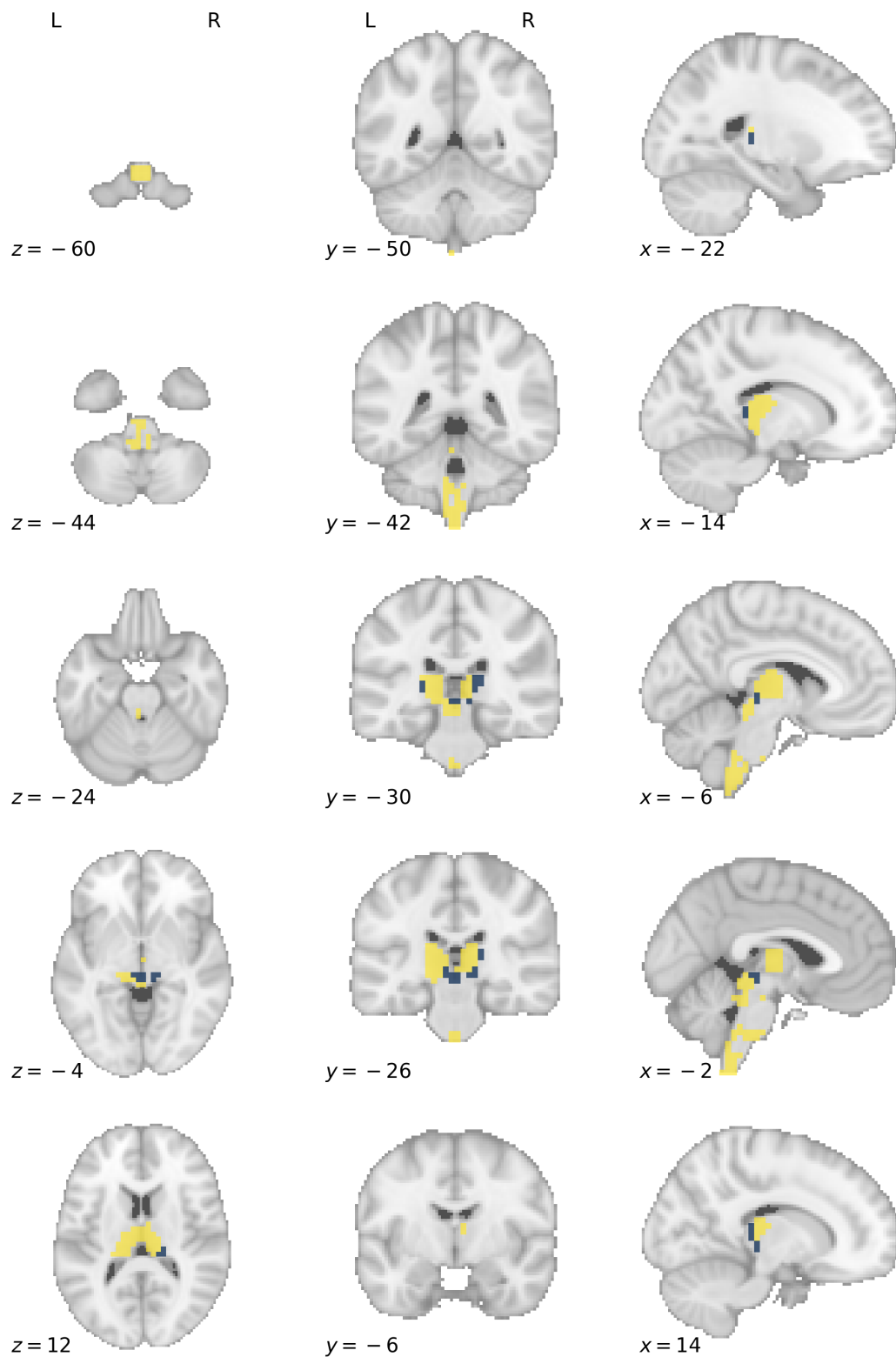


**f**



Three-dimensional rendering of the functional grey matter network representing *sleep*. The colours label functional subnetworks separated by microarray gene expression data, here represented in yellow and blue. This forms the basis upon which treatment effect heterogeneity is simulated, with hypothetical treatments selectively effective for lesions disrupting defined subnetworks. Each panel shows the same render from a different spatial perspective: **a**, left; **b**, right; **c**, anterior; **d**, posterior; **e**, superior; **f**, inferior.

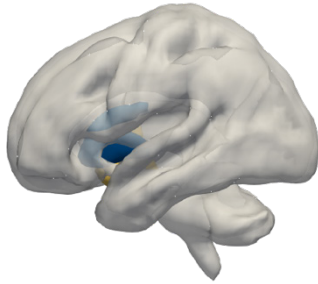
### S10.10.2: *Sleep* subnetwork axial slices



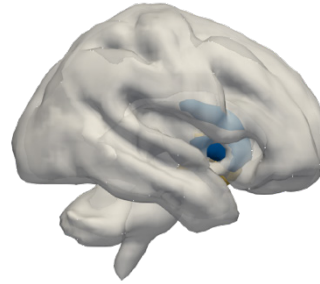
Axial slice visualisation of the functional grey matter network representing *sleep*, overlaid onto the standard MNI152 template. The labelled co-ordinates map to MNI space. The colours label functional subnetworks separated by microarray gene expression, here represented in yellow and blue. This forms the basis upon which treatment effect heterogeneity is simulated, with hypothetical treatments selectively effective for lesions disrupting defined subnetworks.

### S10.11.1: *Reward* subnetwork render

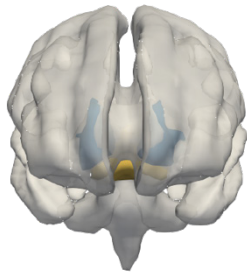
**a**



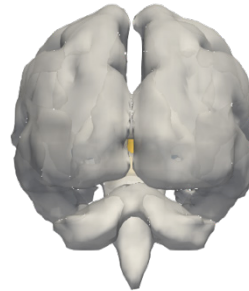
**b**



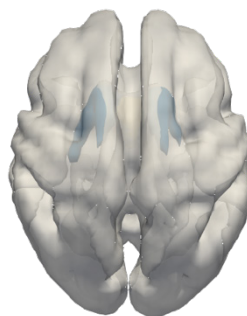
**c**



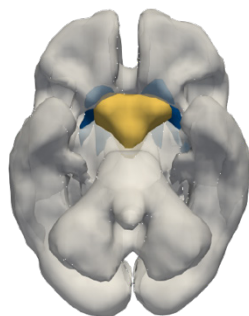
**d**



**e**

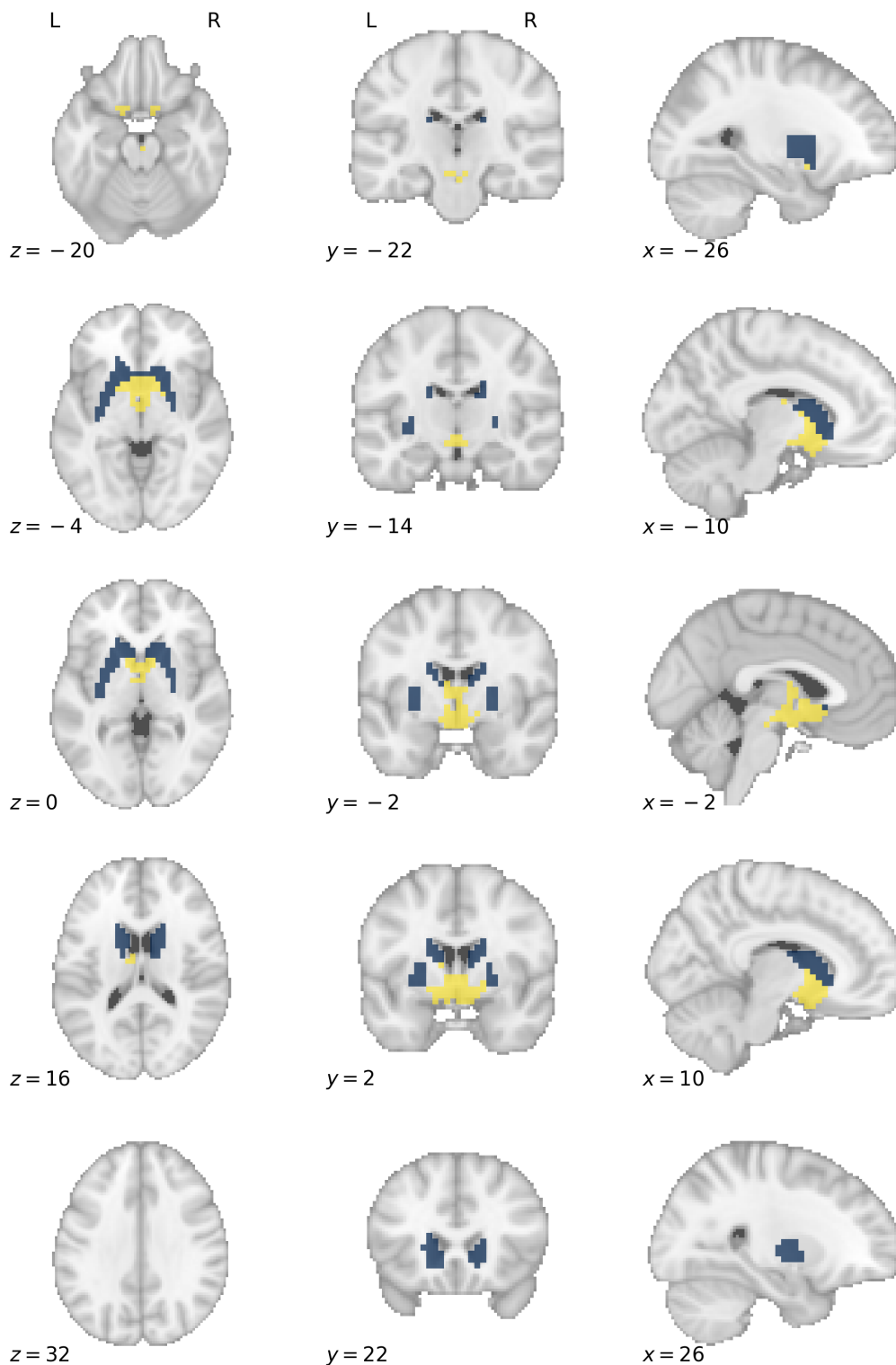


**f**



Three-dimensional rendering of the functional grey matter network representing *reward*. The colours label functional subnetworks separated by microarray gene expression data, here represented in yellow and blue. This forms the basis upon which treatment effect heterogeneity is simulated, with hypothetical treatments selectively effective for lesions disrupting defined subnetworks. Each panel shows the same render from a different spatial perspective: **a**, left; **b**, right; **c**, anterior; **d**, posterior; **e**, superior; **f**, inferior.

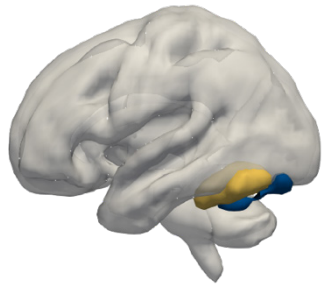
### S10.11.2: *Reward* subnetwork axial slices



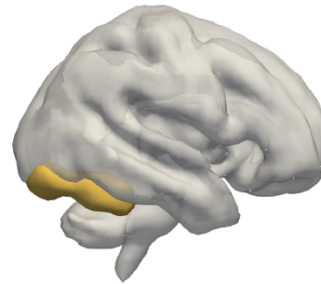
Axial slice visualisation of the functional grey matter network representing *reward*, overlaid onto the standard MNI152 template. The labelled co-ordinates map to MNI space. The colours label functional subnetworks separated by microarray gene expression, here represented in yellow and blue. This forms the basis upon which treatment effect heterogeneity is simulated, with hypothetical treatments selectively effective for lesions disrupting defined subnetworks.

### S10.12.1: *Visual Recognition* subnetwork render

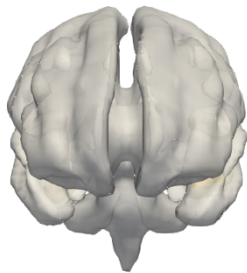
a



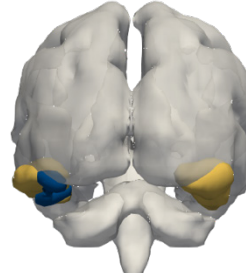
b



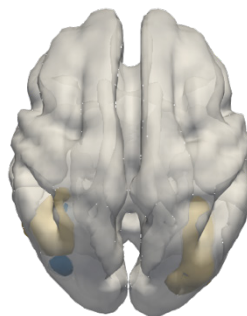
c



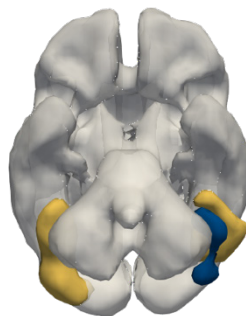
d



e

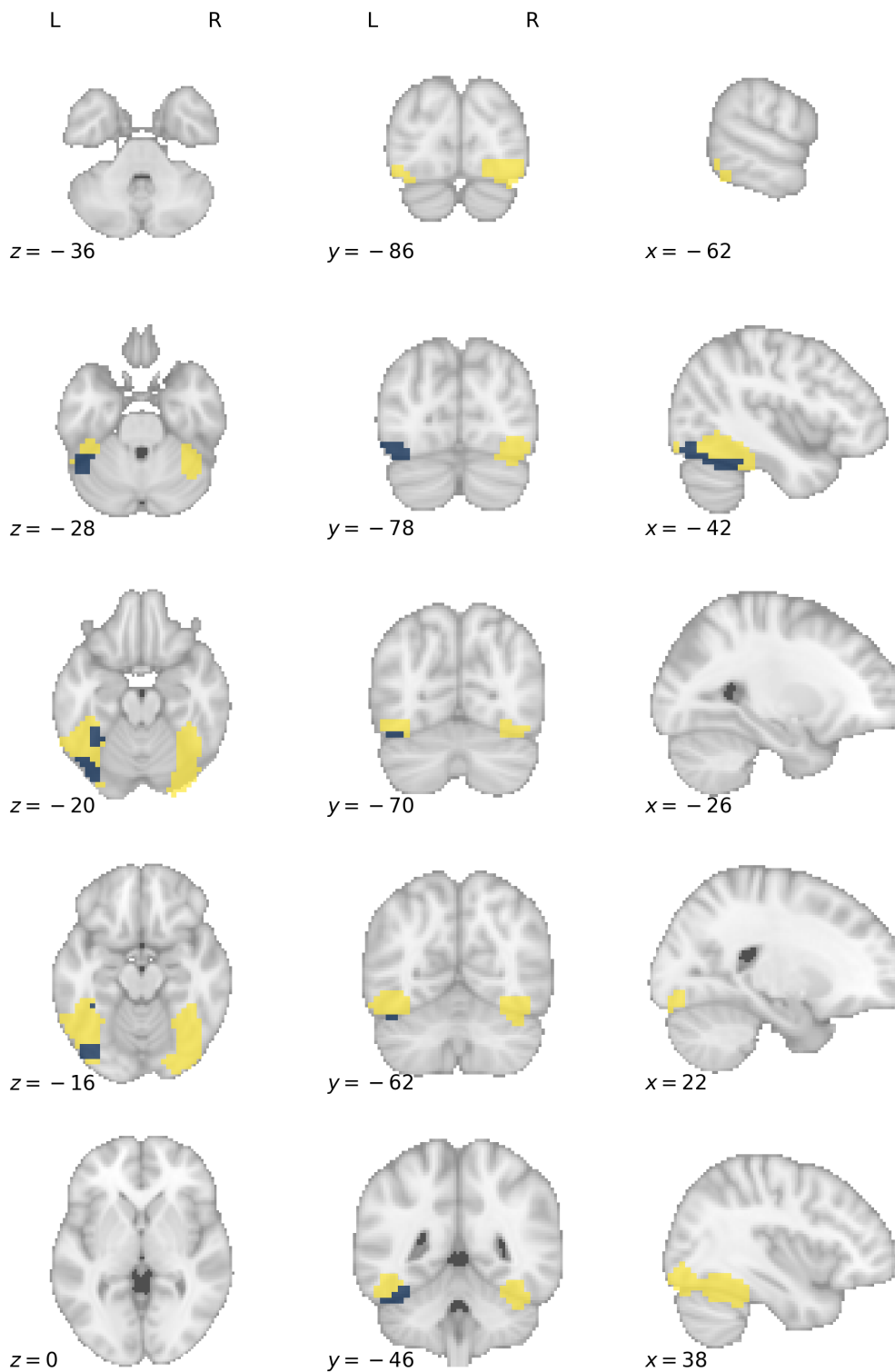


f



Three-dimensional rendering of the functional grey matter network representing *visual recognition*. The colours label functional subnetworks separated by microarray gene expression data, here represented in yellow and blue. This forms the basis upon which treatment effect heterogeneity is simulated, with hypothetical treatments selectively effective for lesions disrupting defined subnetworks. Each panel shows the same render from a different spatial perspective: **a**, left; **b**, right; **c**, anterior; **d**, posterior; **e**, superior; **f**, inferior.

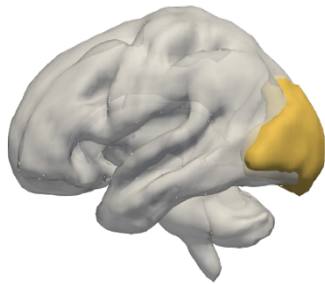
## S10.12.2: *Visual Recognition* subnetwork axial slices



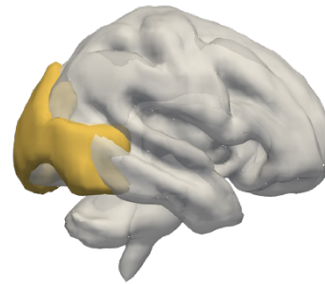
Axial slice visualisation of the functional grey matter network representing *visual recognition*, overlaid onto the standard MNI152 template. The labelled co-ordinates map to MNI space. The colours label functional subnetworks separated by microarray gene expression, here represented in yellow and blue. This forms the basis upon which treatment effect heterogeneity is simulated, with hypothetical treatments selectively effective for lesions disrupting defined subnetworks.

### S10.13.1: *Visual Perception* subnetwork render

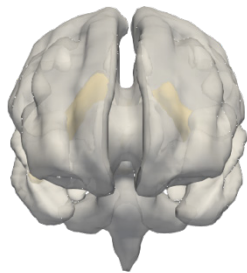
a



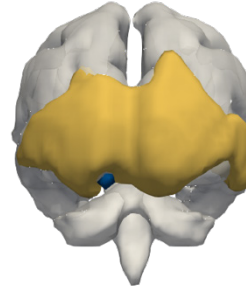
b



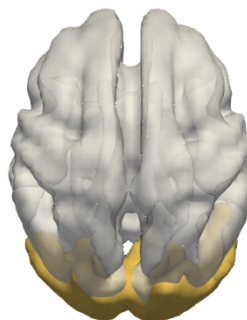
c



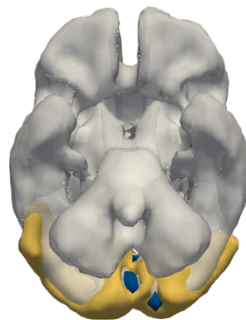
d



e

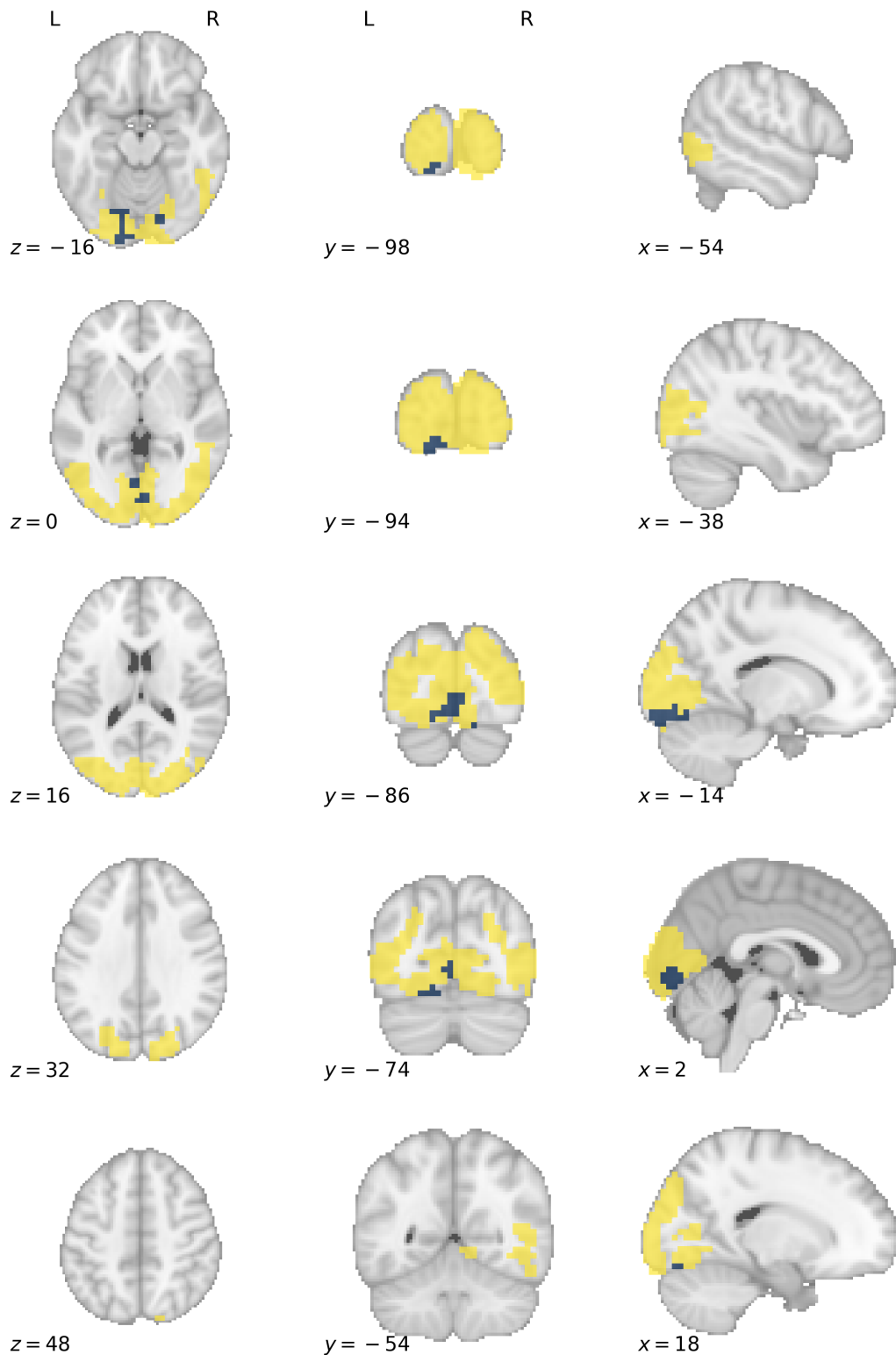


f



Three-dimensional rendering of the functional grey matter network representing *visual perception*. The colours label functional subnetworks separated by microarray gene expression data, here represented in yellow and blue. This forms the basis upon which treatment effect heterogeneity is simulated, with hypothetical treatments selectively effective for lesions disrupting defined subnetworks. Each panel shows the same render from a different spatial perspective: **a**, left; **b**, right; **c**, anterior; **d**, posterior; **e**, superior; **f**, inferior.

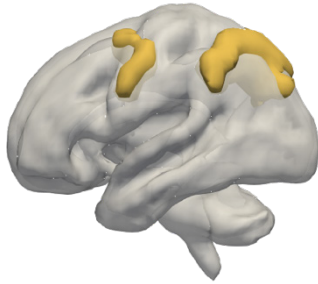
### S10.13.2: *Visual Perception* subnetwork axial slices



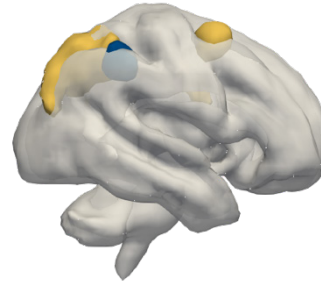
Axial slice visualisation of the functional grey matter network representing *visual perception*, overlaid onto the standard MNI152 template. The labelled co-ordinates map to MNI space. The colours label functional subnetworks separated by microarray gene expression, here represented in yellow and blue. This forms the basis upon which treatment effect heterogeneity is simulated, with hypothetical treatments selectively effective for lesions disrupting defined subnetworks.

### S10.14.1: *Spatial Reasoning* subnetwork render

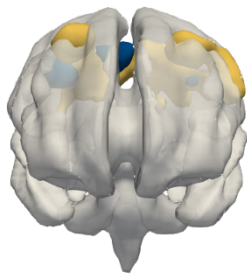
a



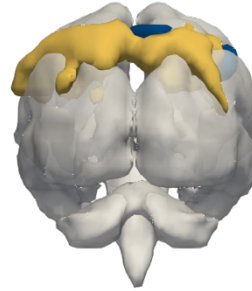
b



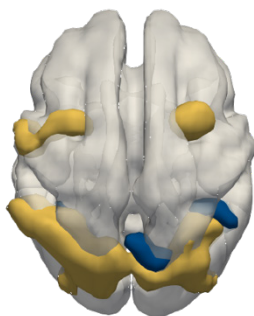
c



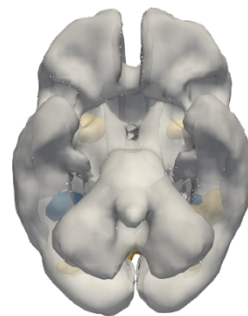
d



e

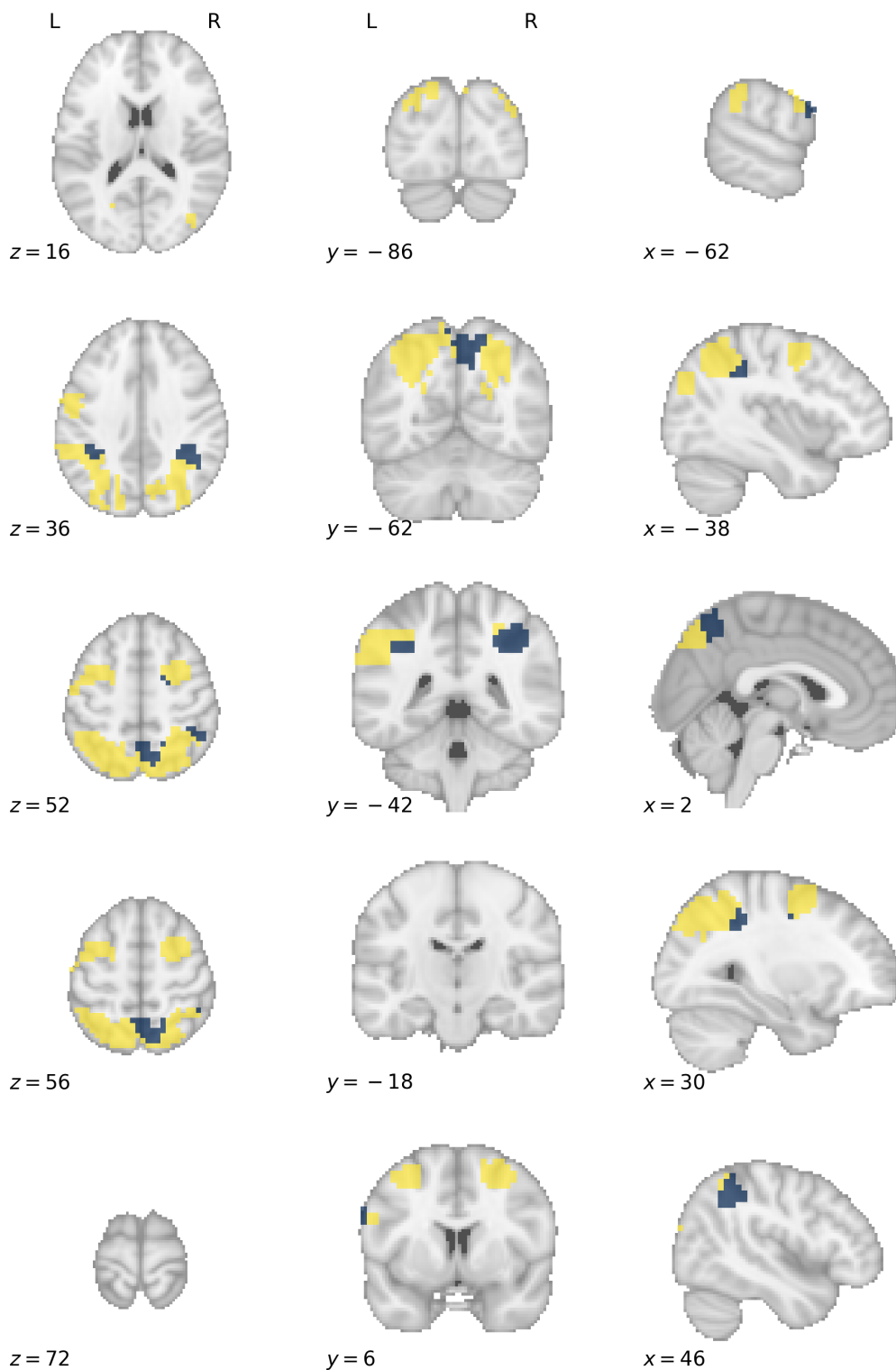


f



Three-dimensional rendering of the functional grey matter network representing *spatial reasoning*. The colours label functional subnetworks separated by microarray gene expression data, here represented in yellow and blue. This forms the basis upon which treatment effect heterogeneity is simulated, with hypothetical treatments selectively effective for lesions disrupting defined subnetworks. Each panel shows the same render from a different spatial perspective: **a**, left; **b**, right; **c**, anterior; **d**, posterior; **e**, superior; **f**, inferior.

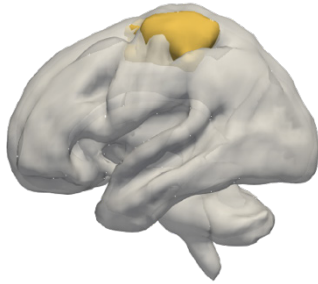
### S10.14.2: *Spatial Reasoning* subnetwork axial slices



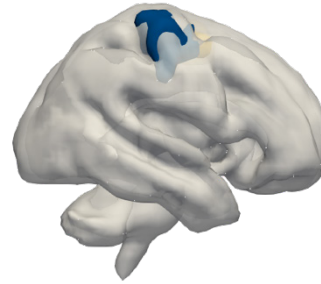
Axial slice visualisation of the functional grey matter network representing *spatial reasoning*, overlaid onto the standard MNI152 template. The labelled co-ordinates map to MNI space. The colours label functional subnetworks separated by microarray gene expression, here represented in yellow and blue. This forms the basis upon which treatment effect heterogeneity is simulated, with hypothetical treatments selectively effective for lesions disrupting defined subnetworks.

### S10.15.1: *Motor* subnetwork render

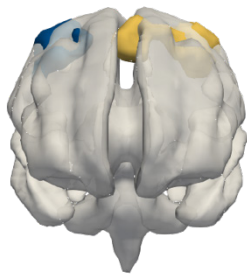
a



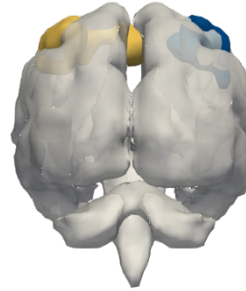
b



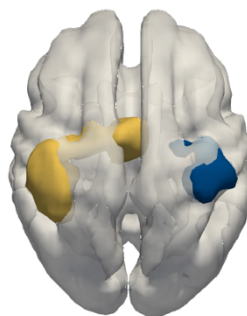
c



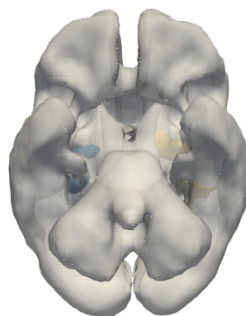
d



e

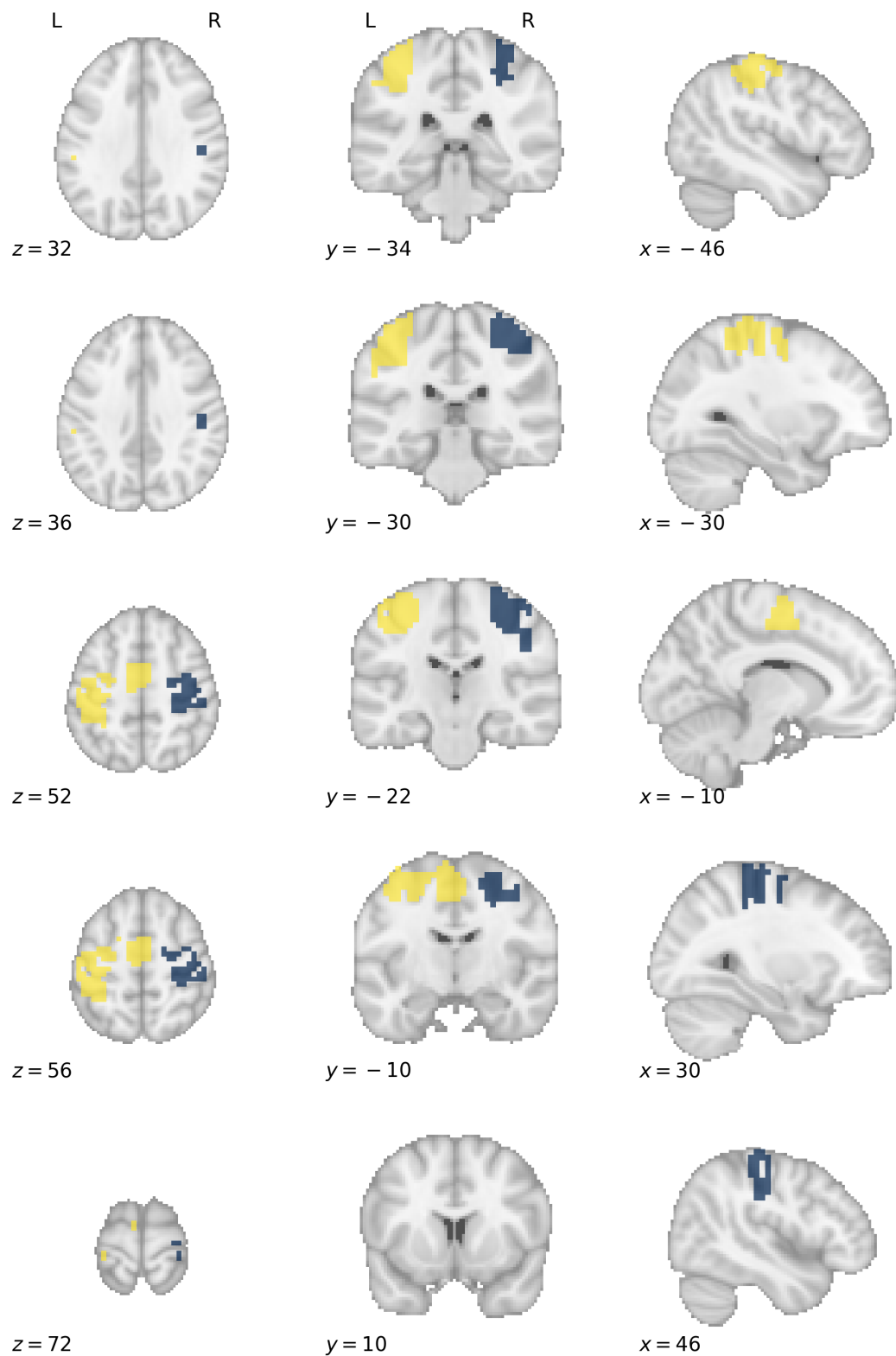


f



Three-dimensional rendering of the functional grey matter network representing *motor behaviour*. The colours label functional subnetworks separated by microarray gene expression data, here represented in yellow and blue. This forms the basis upon which treatment effect heterogeneity is simulated, with hypothetical treatments selectively effective for lesions disrupting defined subnetworks. Each panel shows the same render from a different spatial perspective: **a**, left; **b**, right; **c**, anterior; **d**, posterior; **e**, superior; **f**, inferior.

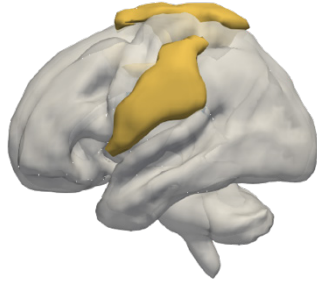
## S10.15.2: *Motor* subnetwork axial slices



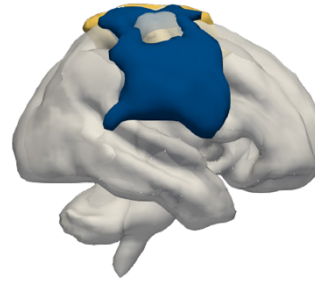
Axial slice visualisation of the functional grey matter network representing *motor behaviour*, overlaid onto the standard MNI152 template. The labelled co-ordinates map to MNI space. The colours label functional subnetworks separated by microarray gene expression, here represented in yellow and blue. This forms the basis upon which treatment effect heterogeneity is simulated, with hypothetical treatments selectively effective for lesions disrupting defined subnetworks.

### S10.16.1: *Somatosensory* subnetwork render

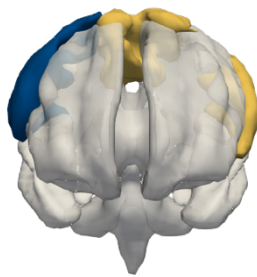
a



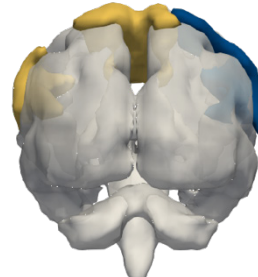
b



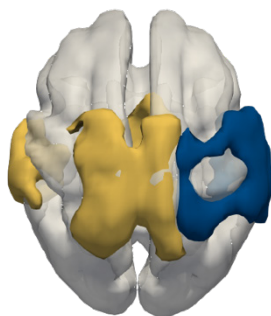
c



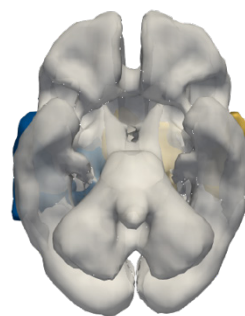
d



e

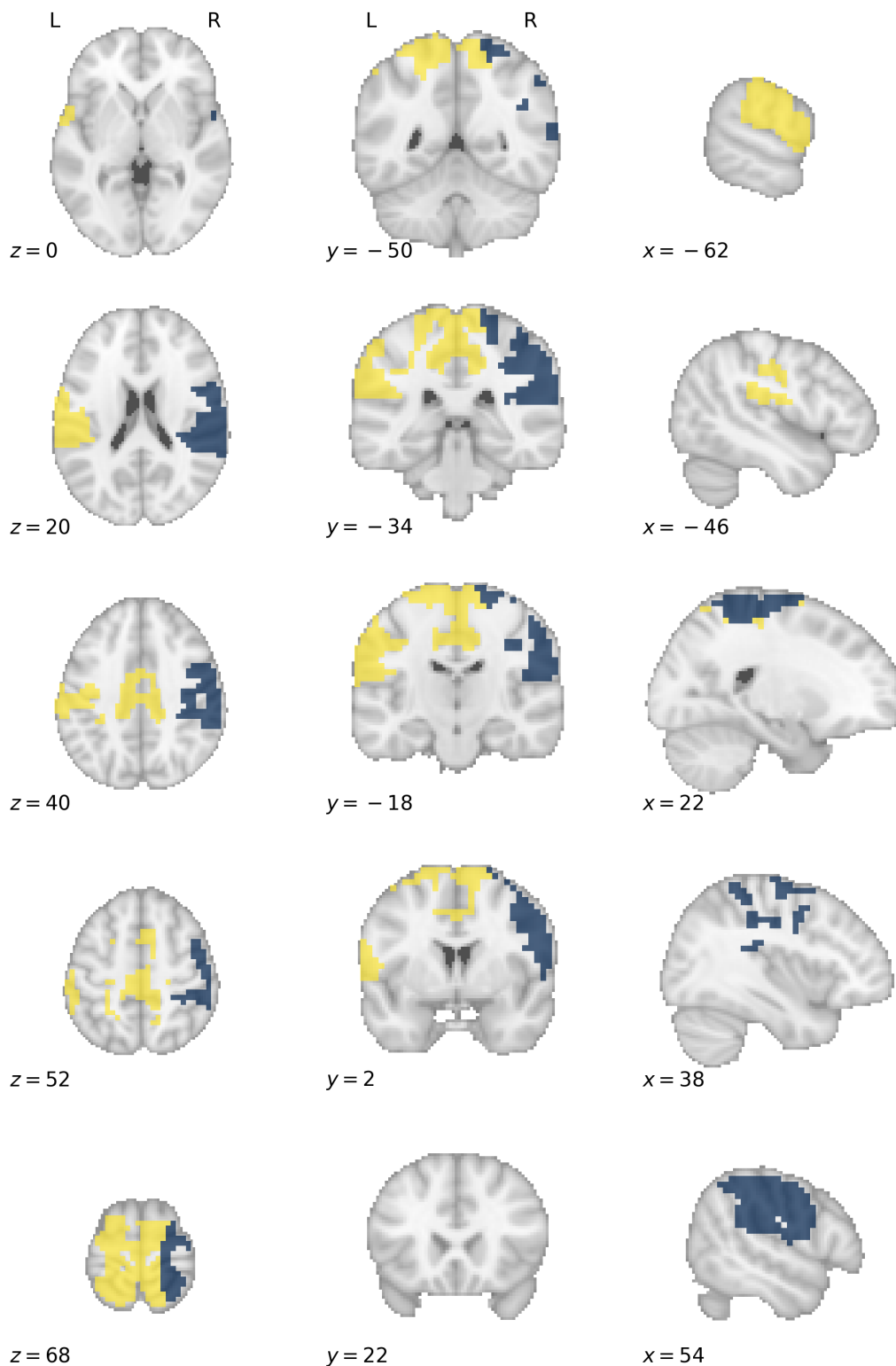


f



Three-dimensional rendering of the functional grey matter network representing *somatosensory function*. The colours label functional subnetworks separated by microarray gene expression data, here represented in yellow and blue. This forms the basis upon which treatment effect heterogeneity is simulated, with hypothetical treatments selectively effective for lesions disrupting defined subnetworks. Each panel shows the same render from a different spatial perspective: **a**, left; **b**, right; **c**, anterior; **d**, posterior; **e**, superior; **f**, inferior.

## S10.16.2: Somatosensory subnetwork axial slices



Axial slice visualisation of the functional grey matter network representing *somatosensory function*, overlaid onto the standard MNI152 template. The labelled co-ordinates map to MNI space. The colours label functional subnetworks separated by microarray gene expression, here represented in yellow and blue. This forms the basis upon which treatment effect heterogeneity is simulated, with hypothetical treatments selectively effective for lesions disrupting defined subnetworks.

## S11: Lesion representations & location bias results

### S11.1: Full results table

Representation	Model	Configuration	Prescriptive balanced accuracy	Observed PEHE
VAE	ExtraTrees	Two	<i>0.638095</i>	<i>0.670712</i>
VAE	Logistic regression	Two	0.632575	0.706211
VAE	Random forest	Two	0.632377	0.673765
AE	Logistic regression	Two	0.630802	0.711604
AE	ExtraTrees	Two	0.630651	0.676929
PCA	ExtraTrees	Two	0.627552	0.680252
PCA	Random forest	Two	0.625893	0.676612
AE	Random forest	Two	0.624254	0.678743
VAE	ExtraTrees	One	0.620283	0.695618
VAE	XGBoost	Two	0.620071	0.712113
PCA	XGBoost	Two	0.618296	0.714805
AE	XGBoost	Two	0.615551	0.715816
AE	ExtraTrees	One	0.614499	0.697340
PCA	ExtraTrees	One	0.613021	0.694528
PCA	Logistic regression	Two	0.612483	0.731578
NMF	ExtraTrees	Two	0.604669	0.705303
NMF	ExtraTrees	One	0.603761	0.705476
NMF	Random forest	Two	0.600153	0.700542
NMF	Random forest	One	0.580878	0.725727
VAE	Random forest	One	0.578627	0.730461
AE	Random forest	One	0.576798	0.729762
PCA	Random forest	One	0.575839	0.730990
NMF	XGBoost	Two	0.570808	0.756893
AE	XGBoost	One	0.560585	0.715964
VAE	XGBoost	One	0.559008	0.716564
PCA	XGBoost	One	0.555964	0.715761
VAE	Gaussian process	One	0.553557	0.759963
NMF	XGBoost	One	0.553063	0.720112
VAE	Gaussian process	Two	0.550553	0.758173
NMF	Gaussian process	Two	0.532766	0.712642
NMF	Logistic regression	Two	0.531445	0.709866
NMF	Gaussian process	One	0.528550	0.713111
AE	Gaussian process	One	0.527859	0.760956
PCA	Gaussian process	One	0.527066	0.757244
PCA	Gaussian process	Two	0.526727	0.755334
AE	Gaussian process	Two	0.525933	0.759227
PCA	Logistic regression	One	0.484691	0.726026
AE	Logistic regression	One	0.484600	0.726624
VAE	Logistic regression	One	0.484444	0.725735
NMF	Logistic regression	One	0.484085	0.724560

## S11.2: Optimal model by prescriptive balanced accuracy: VAE, two-model ExtraTrees

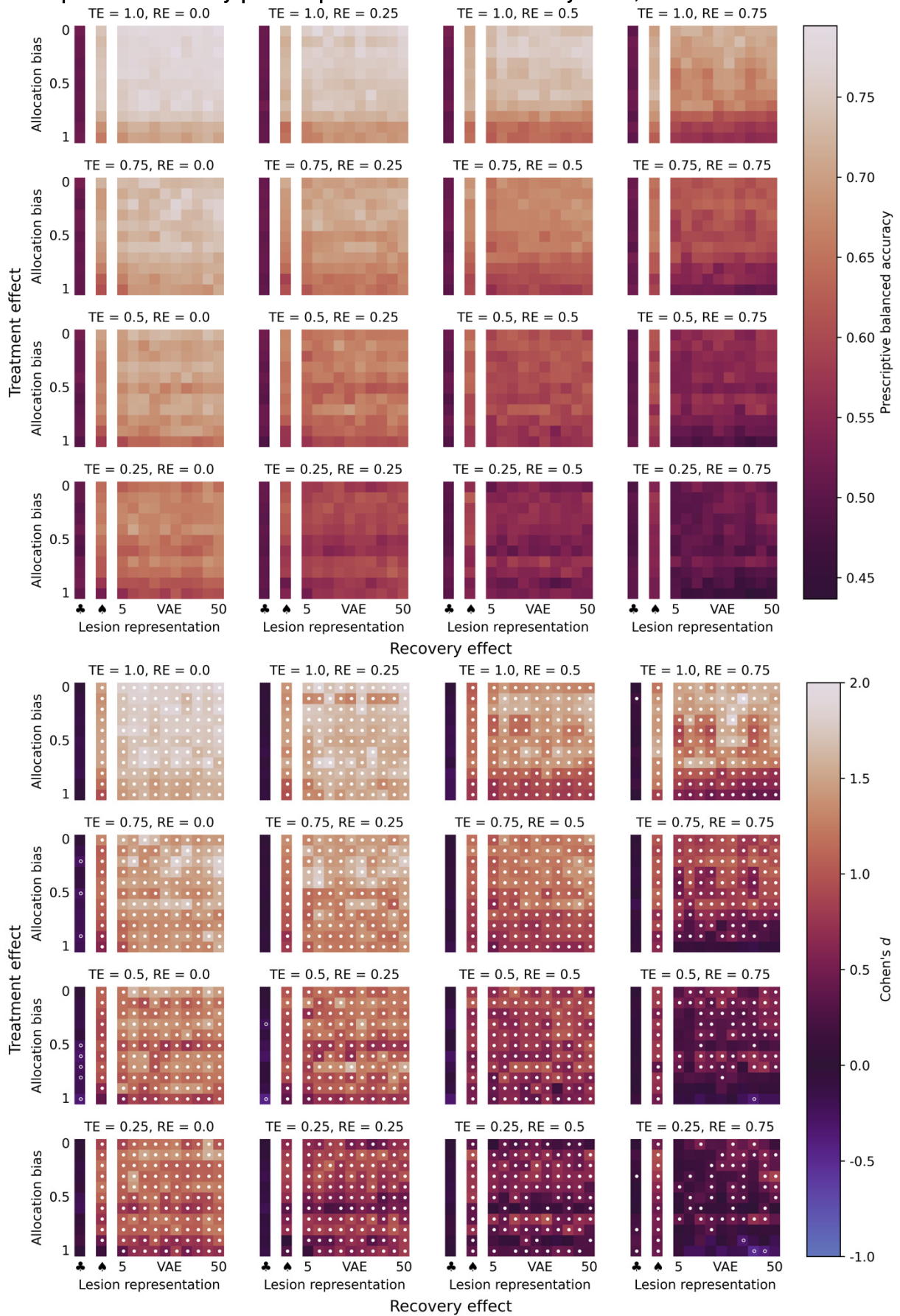


**Figure S11.2. Performance comparison of models with lesion representations: balanced accuracy (upper panel) and statistical analysis (lower panel).** Prescriptive performance of an optimized, extremely randomized trees-based treatment recommendation system, given binary lesion representations, across the range of response noise (major axes) and allocation bias (minor  $y$ -axes), at various levels of expressivity of the individualized representation quantified by embedding length (minor  $x$ -axes). The columns to the left of each minor axis show prescriptive performance when individual phenotypes are represented by classification of major affected arterial territory: anterior or posterior circulation (♣) and ACA/MCA/posterior cerebral artery/VB (♠). The upper left subplot shows performance under zero response noise and the lower right subplot shows performance under the conditions of extremely high response noise. The top row of each subplot shows perfect randomization, with zero allocation bias. The upper panel shows prescriptive performance measured by balanced accuracy—the mean proportion of patients allocated to the treatment for which they are truly susceptible—for patients that are exclusively susceptible to one treatment.

The lower panel shows Cohen's  $d$ -effect sizes, by colour, when comparing the prescriptive performance (measured by balanced accuracy, as shown in the upper panel) against a randomized trial based upon individualized information consisting of the major vascular supply (anterior or posterior circulation), at each respective TE/RE pair. Warm colours show performance greater than the comparative randomized trial, while cool colours show the converse. White shows equivalent performance. Trials marked with a circle indicate an effect size exceeding the critical  $p$ -value 0.0423 (as adjusted for multiple comparisons at the 0.05 significance level, according to the Benjamini-Hochberg procedure), corresponding to the  $t$ -value in a two-sided independent sample  $t$ -test. Filled circles show superiority of the prescriptive model from observational data; unfilled circles show superiority of the randomized trial.

TE: treatment effect; RE: recovery effect; VAE: variational auto-encoder representation; ACA: anterior cerebral artery; MCA: middle cerebral artery; VB: vertebrobasilar artery

### S11.3: Best-performing by PEHE: VAE, two-model ExtraTrees

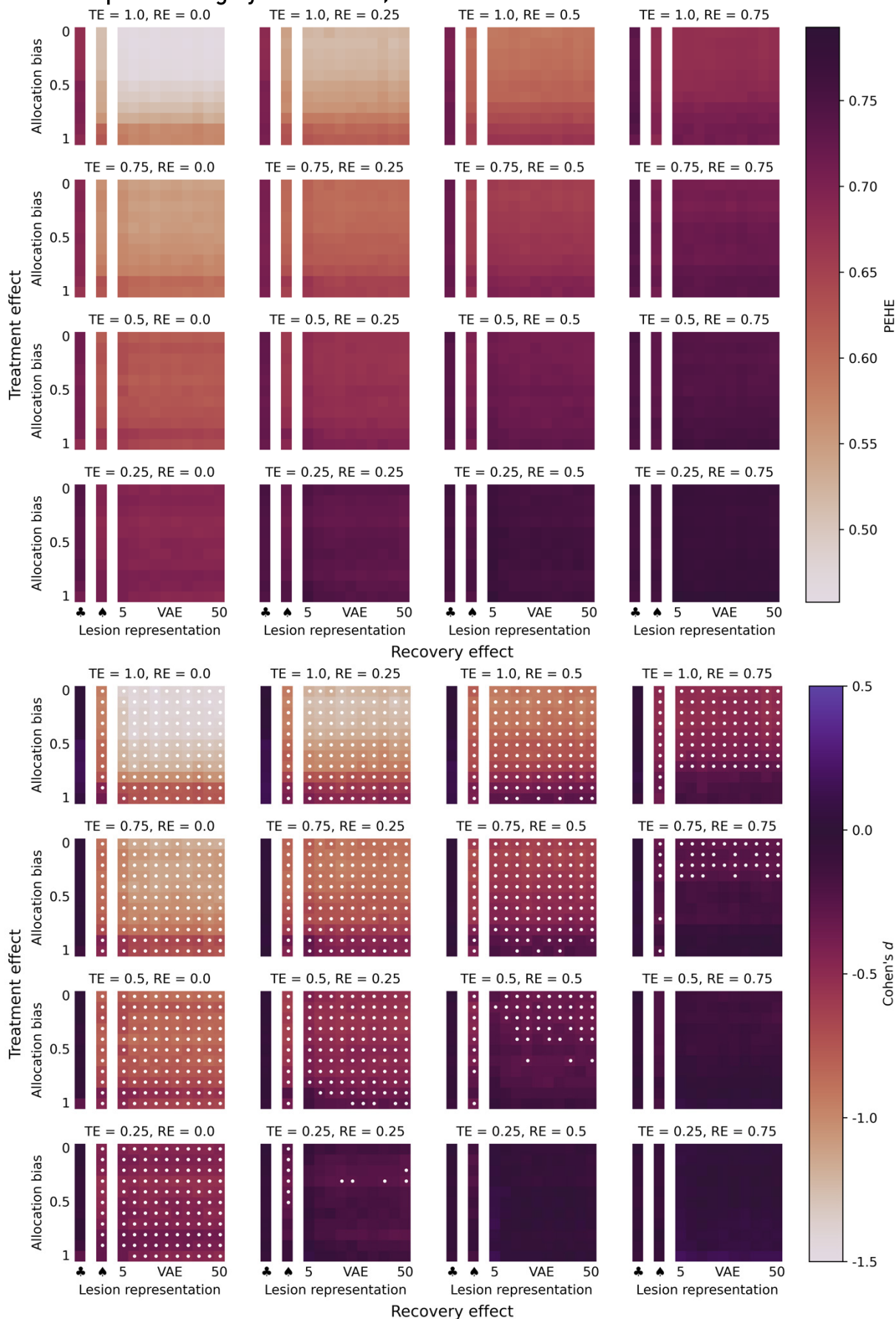


**Figure S11.3. Performance comparison of models with lesion representations: PEHE (upper panel) and statistical analysis (lower panel).** Prescriptive performance of an optimized, extremely randomized trees-based treatment recommendation system, given binary lesion representations, across the range of response noise (major axes) and allocation bias (minor y-axes), at various levels of expressivity of the individualized representation quantified by embedding length (minor x-axes). The columns to the left of each minor axis show prescriptive performance when individual phenotypes are represented by classification of major affected arterial territory: anterior or posterior circulation (♣) and ACA/MCA/posterior cerebral artery/VB (♠). The upper left subplot shows performance under zero response noise and the lower right subplot shows performance under the conditions of extremely high response noise. The top row of each subplot shows perfect randomization, with zero allocation bias. The upper panel shows prescriptive performance measured by PEHE the root-mean-squared-error in estimation of the true individualized treatment effect (lower is better).

The lower panel shows Cohen's  $d$ -effect sizes, by colour, when comparing the prescriptive performance (measured by PEHE, as shown in the upper panel) against a randomized trial based upon individualized information consisting of the major vascular supply (anterior or posterior circulation), at each respective TE/RE pair. Warm colours show performance greater than the comparative randomized trial, while cool colours show the converse. White shows equivalent performance. Trials marked with a circle indicate an effect size exceeding the critical  $p$ -value 0.0285 (as adjusted for multiple comparisons at the 0.05 significance level, according to the Benjamini-Hochberg procedure), corresponding to the  $t$ -value in a two-sided independent sample  $t$ -test. Filled circles show superiority of the prescriptive model from observational data; unfilled circles show superiority of the randomized trial.

TE: treatment effect; RE: recovery effect; VAE: variational auto-encoder representation; ACA: anterior cerebral artery; MCA: middle cerebral artery; VB: vertebrobasilar artery

## S12: Disconnectome representations & location bias results

### S12.1: Full results table

Representation	Model	Configuration	Prescriptive balanced accuracy	Observed PEHE
AE	ExtraTrees	Two	<b>0.718161</b>	0.573161
VAE	ExtraTrees	Two	0.712637	0.576710
AE	Logistic regression	Two	0.711435	<b>0.564923</b>
AE	Random forest	Two	0.708890	0.574772
PCA	ExtraTrees	Two	0.707576	0.579157
VAE	Logistic regression	Two	0.705775	0.568535
AE	ExtraTrees	One	0.705127	0.593895
VAE	Random forest	Two	0.704094	0.578082
VAE	ExtraTrees	One	0.699950	0.596088
AE	XGBoost	Two	0.699258	0.611886
VAE	XGBoost	Two	0.695058	0.616278
PCA	Random forest	Two	0.694213	0.581038
PCA	ExtraTrees	One	0.694118	0.596600
PCA	Logistic regression	Two	0.691628	0.590505
PCA	XGBoost	Two	0.687607	0.617454
NMF	Gaussian process	Two	0.686881	0.617289
NMF	Gaussian process	One	0.682916	0.617831
NMF	ExtraTrees	Two	0.680377	0.597582
NMF	Logistic regression	Two	0.669639	0.583176
NMF	ExtraTrees	One	0.666861	0.614481
AE	Random forest	One	0.661850	0.629989
VAE	Random forest	One	0.658928	0.631005
AE	XGBoost	One	0.653617	0.608419
VAE	XGBoost	One	0.650446	0.610225
NMF	Random forest	Two	0.648854	0.620553
NMF	XGBoost	Two	0.648703	0.646442
PCA	Random forest	One	0.647613	0.631801
PCA	XGBoost	One	0.638673	0.611830
NMF	XGBoost	One	0.629108	0.617982
NMF	Random forest	One	0.612928	0.646711
AE	Gaussian process	One	0.612842	0.679290
AE	Gaussian process	Two	0.610761	0.679116
VAE	Gaussian process	One	0.609586	0.676570
VAE	Gaussian process	Two	0.607783	0.676405
PCA	Gaussian process	Two	0.515168	0.684232
PCA	Gaussian process	One	0.514813	0.684112
PCA	Logistic regression	One	0.500099	0.633768
VAE	Logistic regression	One	0.500000	0.634573
AE	Logistic regression	One	0.500000	0.634102
NMF	Logistic regression	One	0.500000	0.634233

## S12.2: Optimal model by prescriptive balanced accuracy: AE, two-model ExtraTrees

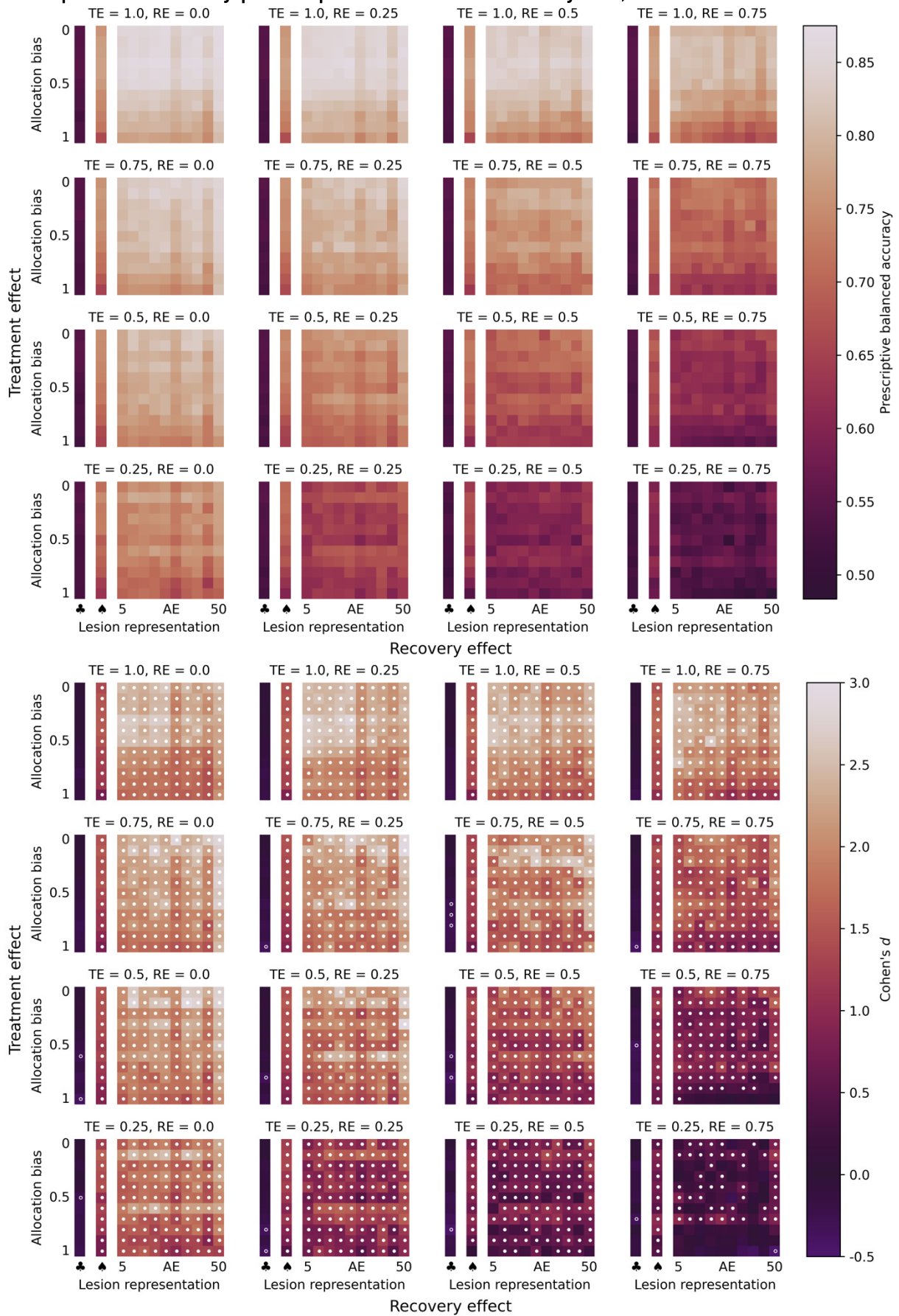


**Figure S12.2. Performance comparison of models with disconnectome representations: balanced accuracy (upper panel) and statistical analysis (lower panel).** Prescriptive performance of an optimized, extremely randomized trees-based treatment recommendation system, given lesion disconnectome representations, across the range of response noise (major axes) and allocation bias (minor  $y$ -axes), at various levels of expressivity of the individualized representation quantified by embedding length (minor  $x$ -axes). The columns to the left of each minor axis show prescriptive performance when individual phenotypes are represented by classification of major affected arterial territory: anterior or posterior circulation (♣) and ACA/MCA/posterior cerebral artery/VB (♠). The upper left subplot shows performance under zero response noise and the lower right subplot shows performance under the conditions of extremely high response noise. The top row of each subplot shows perfect randomization, with zero allocation bias. The upper panel shows prescriptive performance measured by balanced accuracy—the mean proportion of patients allocated to the treatment for which they are truly susceptible—for patients that are exclusively susceptible to one treatment.

The lower panel shows Cohen's  $d$ -effect sizes, by colour, when comparing the prescriptive performance (measured by balanced accuracy, as shown in the upper panel) against a randomized trial based upon individualized information consisting of the major vascular supply (anterior or posterior circulation), at each respective TE/RE pair. Warm colours show performance greater than the comparative randomized trial, while cool colours show the converse. White shows equivalent performance. Trials marked with a circle indicate an effect size exceeding the critical  $p$ -value 0.0439 (as adjusted for multiple comparisons at the 0.05 significance level, according to the Benjamini-Hochberg procedure), corresponding to the  $t$ -value in a two-sided independent sample  $t$ -test. Filled circles show superiority of the prescriptive model from observational data; unfilled circles show superiority of the randomized trial.

TE: treatment effect; RE: recovery effect; AE: auto-encoder representation; ACA: anterior cerebral artery; MCA: middle cerebral artery; VB: vertebrobasilar artery

### S12.3 Optimal model by PEHE: AE, two-model logistic regression

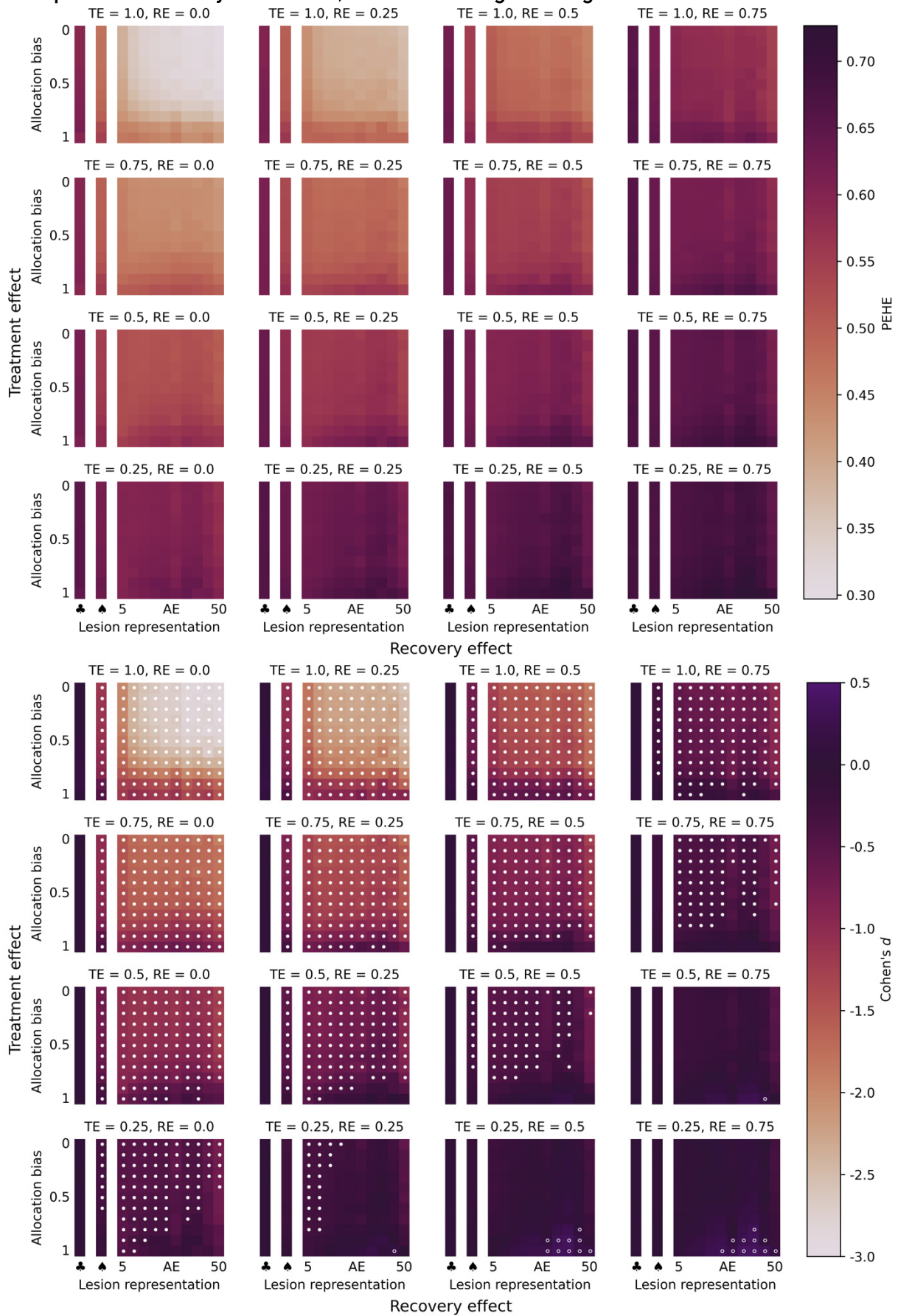


**Figure S12.3. Performance comparison of models with disconnectome representations: PEHE (upper panel) and statistical analysis (lower panel).** Prescriptive performance of an optimized, logistic regression-based treatment recommendation system, given lesion disconnectome representations, across the range of response noise (major axes) and allocation bias (minor  $y$ -axes), at various levels of expressivity of the individualized representation quantified by embedding length (minor  $x$ -axes). The columns to the left of each minor axis show prescriptive performance when individual phenotypes are represented by classification of major affected arterial territory: anterior or posterior circulation (♣) and ACA/MCA/posterior cerebral artery/VB (♠). The upper left subplot shows performance under zero response noise and the lower right subplot shows performance under the conditions of extremely high response noise. The top row of each subplot shows perfect randomization, with zero allocation bias. The upper panel shows prescriptive performance measured by PEHE the root-mean-squared-error in estimation of the true individualized treatment effect (lower is better).

The lower panel shows Cohen's  $d$ -effect sizes, by colour, when comparing the prescriptive performance (measured by PEHE, as shown in the upper panel) against a randomized trial based upon individualized information consisting of the major vascular supply (anterior or posterior circulation), at each respective TE/RE pair. Warm colours show performance greater than the comparative randomized trial, while cool colours show the converse. White shows equivalent performance. Trials marked with a circle indicate an effect size exceeding the critical  $p$ -value 0.0308 (as adjusted for multiple comparisons at the 0.05 significance level, according to the Benjamini-Hochberg procedure), corresponding to the  $t$ -value in a two-sided independent sample  $t$ -test. Filled circles show superiority of the prescriptive model from observational data; unfilled circles show superiority of the randomized trial.

TE: treatment effect; RE: recovery effect; AE: auto-encoder representation; ACA: anterior cerebral artery; MCA: middle cerebral artery; VB: vertebrobasilar artery

## S13: Lesion representations & unobservable bias results

### S13.1: Full results table

Representation	Model	Configuration	Prescriptive balanced accuracy	Observed PEHE
VAE	ExtraTrees	Two	<i>0.634868</i>	<i>0.675041</i>
VAE	Random forest	Two	0.632986	0.675653
PCA	Random forest	Two	0.629856	0.677745
AE	ExtraTrees	Two	0.629503	0.680522
PCA	ExtraTrees	Two	0.628197	0.683752
AE	Random forest	Two	0.626798	0.680120
VAE	Logistic regression	Two	0.626791	0.705085
AE	Logistic regression	Two	0.626455	0.709188
VAE	ExtraTrees	One	0.621575	0.698383
PCA	ExtraTrees	One	0.616874	0.697986
AE	ExtraTrees	One	0.616618	0.699988
VAE	XGBoost	Two	0.615532	0.716068
PCA	XGBoost	Two	0.613898	0.716403
AE	XGBoost	Two	0.612566	0.718603
NMF	ExtraTrees	Two	0.607165	0.705433
PCA	Logistic regression	Two	0.606519	0.723128
NMF	ExtraTrees	One	0.605393	0.708592
NMF	Random forest	Two	0.597810	0.704014
NMF	Random forest	One	0.583920	0.727636
VAE	Random forest	One	0.583522	0.731577
AE	Random forest	One	0.582877	0.731212
PCA	Random forest	One	0.581141	0.732307
AE	XGBoost	One	0.571251	0.715186
VAE	XGBoost	One	0.570046	0.716167
PCA	XGBoost	One	0.566437	0.716168
NMF	XGBoost	Two	0.565989	0.760494
VAE	Gaussian process	One	0.560465	0.759893
VAE	Gaussian process	Two	0.559801	0.758888
NMF	XGBoost	One	0.558269	0.721118
NMF	Gaussian process	Two	0.543848	0.714962
NMF	Gaussian process	One	0.538039	0.717106
NMF	Logistic regression	Two	0.537959	0.713148
PCA	Gaussian process	Two	0.533801	0.755991
AE	Gaussian process	One	0.532606	0.760836
PCA	Gaussian process	One	0.532467	0.757201
AE	Gaussian process	Two	0.532157	0.759965
PCA	Logistic regression	One	0.484090	0.730363
VAE	Logistic regression	One	0.483963	0.730514
AE	Logistic regression	One	0.483900	0.731088
NMF	Logistic regression	One	0.482509	0.731510

### S13.2: Optimal model by prescriptive balanced accuracy: VAE, two-model ExtraTrees

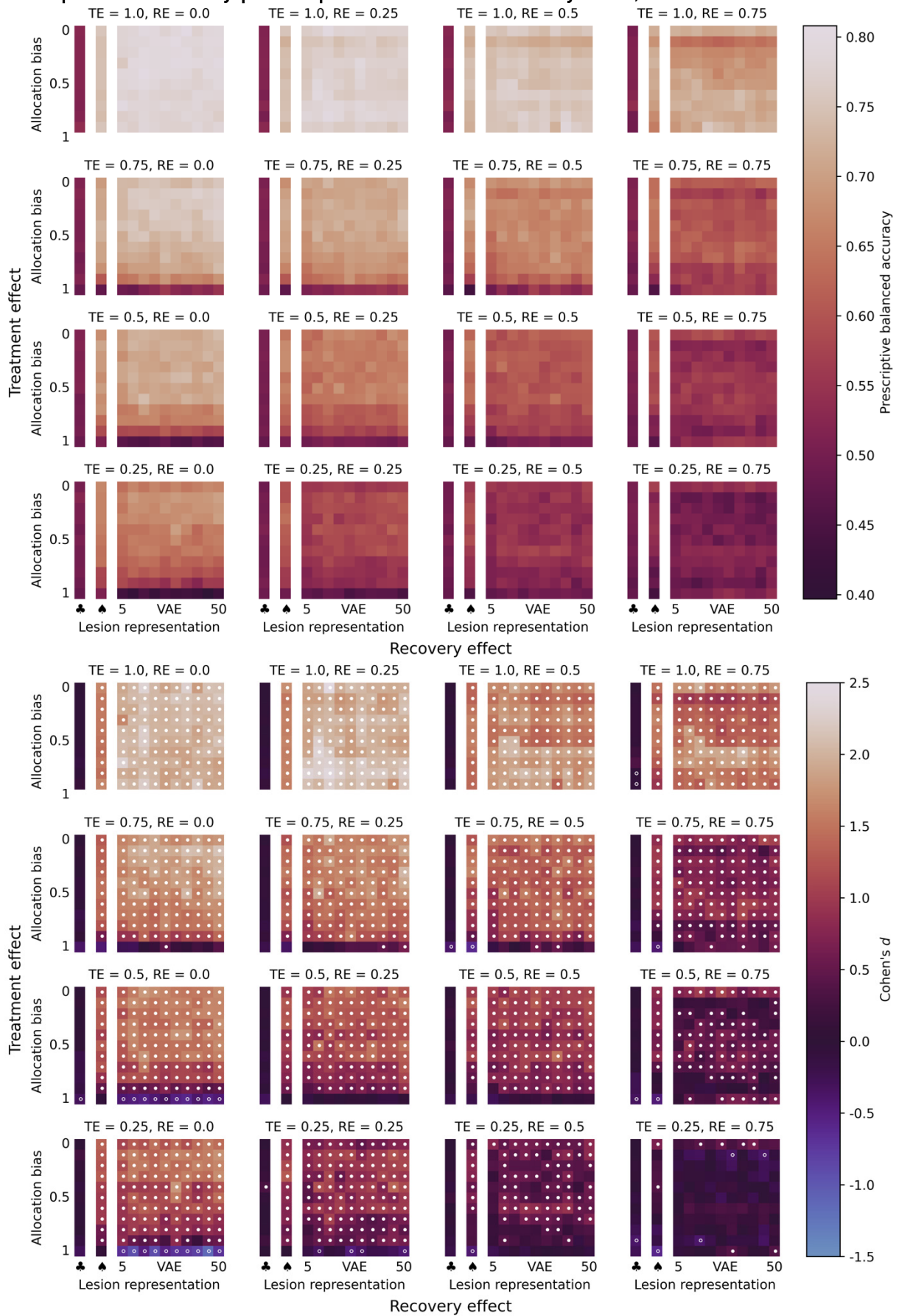


**Figure S13.2. Performance comparison of models with lesion representations: balanced accuracy (upper panel) and statistical analysis (lower panel).** Prescriptive performance of an optimized, extremely randomized trees-based treatment recommendation system, given binary lesion representations, across the range of response noise (major axes) and allocation bias (minor  $y$ -axes), at various levels of expressivity of the individualized representation quantified by embedding length (minor  $x$ -axes). The columns to the left of each minor axis show prescriptive performance when individual phenotypes are represented by classification of major affected arterial territory: anterior or posterior circulation (♣) and ACA/MCA/posterior cerebral artery/VB (♠). The upper left subplot shows performance under zero response noise and the lower right subplot shows performance under the conditions of extremely high response noise. The top row of each subplot shows perfect randomization, with zero allocation bias. The upper panel shows prescriptive performance measured by balanced accuracy—the mean proportion of patients allocated to the treatment for which they are truly susceptible—for patients that are exclusively susceptible to one treatment.

The lower panel shows Cohen's  $d$ -effect sizes, by colour, when comparing the prescriptive performance (measured by balanced accuracy, as shown in the upper panel) against a randomized trial based upon individualized information consisting of the major vascular supply (anterior or posterior circulation), at each respective TE/RE pair. Warm colours show performance greater than the comparative randomized trial, while cool colours show the converse. White shows equivalent performance. Trials marked with a circle indicate an effect size exceeding the critical  $p$ -value 0.0391 (as adjusted for multiple comparisons at the 0.05 significance level, according to the Benjamini-Hochberg procedure), corresponding to the  $t$ -value in a two-sided independent sample  $t$ -test. Filled circles show superiority of the prescriptive model from observational data; unfilled circles show superiority of the randomized trial.

TE: treatment effect; RE: recovery effect; VAE: variational auto-encoder representation; ACA: anterior cerebral artery; MCA: middle cerebral artery; VB: vertebrobasilar artery

### 13.3: Optimal model by PEHE: VAE, two-model ExtraTrees

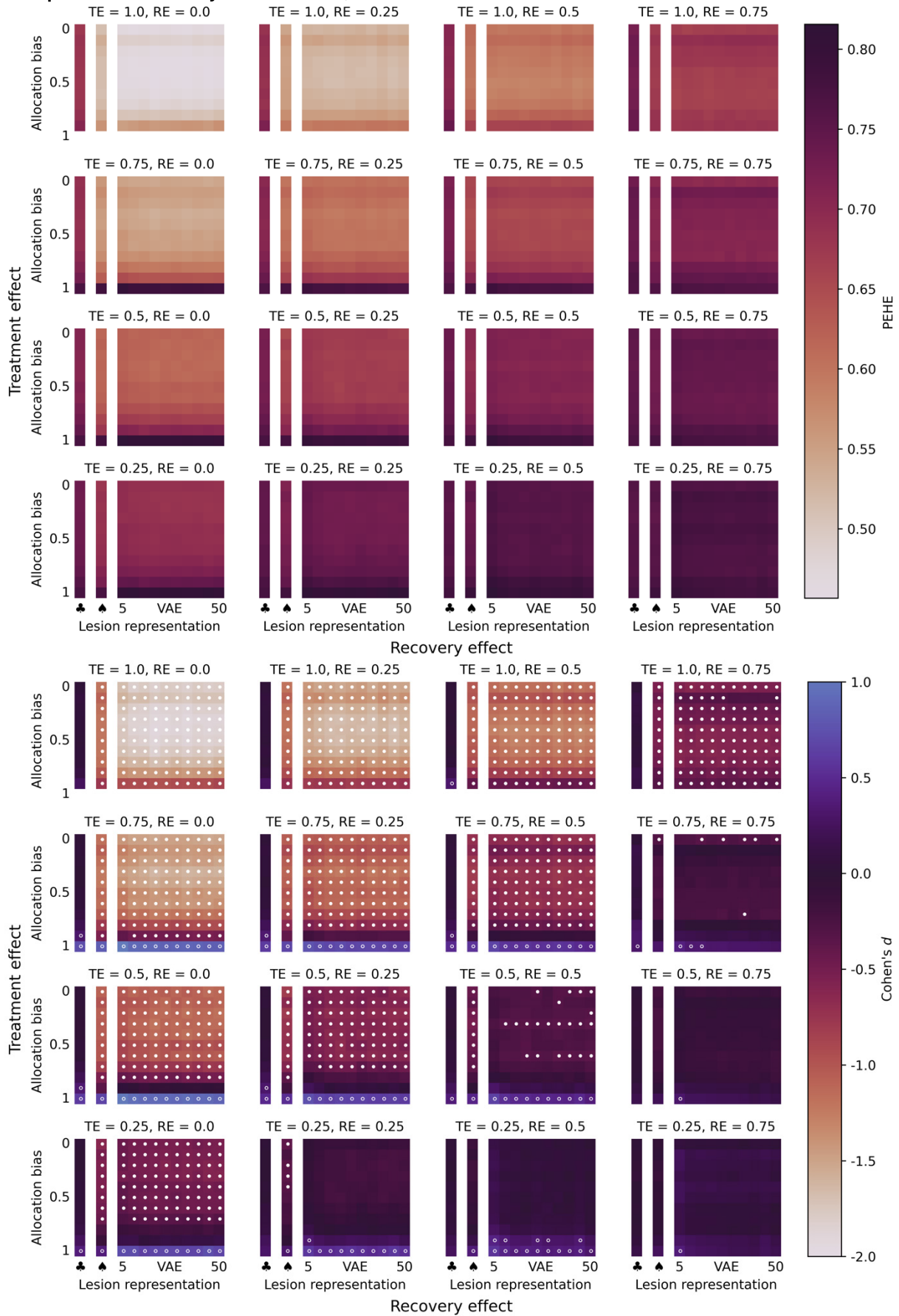


**Figure S13.3. Performance comparison of models with lesion representations: PEHE (upper panel) and statistical analysis (lower panel).** Prescriptive performance of an optimized, extremely randomized trees-based treatment recommendation system, given binary lesion representations, across the range of response noise (major axes) and allocation bias (minor y-axes), at various levels of expressivity of the individualized representation quantified by embedding length (minor x-axes). The columns to the left of each minor axis show prescriptive performance when individual phenotypes are represented by classification of major affected arterial territory: anterior or posterior circulation (♣) and ACA/MCA/posterior cerebral artery/VB (♠). The upper left subplot shows performance under zero response noise and the lower right subplot shows performance under the conditions of extremely high response noise. The top row of each subplot shows perfect randomization, with zero allocation bias. The upper panel shows prescriptive performance measured by PEHE the root-mean-squared-error in estimation of the true individualized treatment effect (lower is better).

The lower panel shows Cohen's *d*-effect sizes, by colour, when comparing the prescriptive performance (measured by PEHE, as shown in the upper panel) against a randomized trial based upon individualized information consisting of the major vascular supply (anterior or posterior circulation), at each respective TE/RE pair. Warm colours show performance greater than the comparative randomized trial, while cool colours show the converse. White shows equivalent performance. Trials marked with a circle indicate an effect size exceeding the critical *p*-value 0.0280 (as adjusted for multiple comparisons at the 0.05 significance level, according to the Benjamini-Hochberg procedure), corresponding to the *t*-value in a two-sided independent sample *t*-test. Filled circles show superiority of the prescriptive model from observational data; unfilled circles show superiority of the randomized trial.

TE: treatment effect; RE: recovery effect; VAE: variational auto-encoder representation; ACA: anterior cerebral artery; MCA: middle cerebral artery; VB: vertebrobasilar artery

## S14: Disconnectome representations & unobservable bias results

### S14.1: Full results table

Representation	Model	Configuration	Prescriptive balanced accuracy	Observed PEHE
AE	ExtraTrees	Two	<b>0.718837</b>	0.579313
AE	Random forest	Two	0.714471	0.578065
VAE	ExtraTrees	Two	0.712073	0.582655
PCA	ExtraTrees	Two	0.710911	0.584353
VAE	Random forest	Two	0.708585	0.581181
AE	ExtraTrees	One	0.708433	0.596302
AE	Logistic regression	Two	0.707938	<b>0.569637</b>
VAE	Logistic regression	Two	0.703190	0.572824
VAE	ExtraTrees	One	0.703130	0.598384
PCA	Random forest	Two	0.702288	0.583597
PCA	ExtraTrees	One	0.699538	0.599767
NMF	Gaussian process	Two	0.699174	0.619340
AE	XGBoost	Two	0.697737	0.618557
NMF	Gaussian process	One	0.695420	0.620670
PCA	Logistic regression	Two	0.693443	0.585198
VAE	XGBoost	Two	0.693418	0.622570
PCA	XGBoost	Two	0.690214	0.621575
NMF	ExtraTrees	Two	0.680675	0.601148
AE	XGBoost	One	0.675524	0.604095
VAE	XGBoost	One	0.672516	0.606058
NMF	Logistic regression	Two	0.671997	0.589040
NMF	ExtraTrees	One	0.671001	0.615725
AE	Random forest	One	0.670605	0.629387
VAE	Random forest	One	0.666972	0.630420
PCA	XGBoost	One	0.661126	0.608323
PCA	Random forest	One	0.655172	0.632082
NMF	Random forest	Two	0.650144	0.623045
NMF	XGBoost	One	0.648049	0.614402
NMF	XGBoost	Two	0.647411	0.651443
AE	Gaussian process	One	0.643552	0.678775
AE	Gaussian process	Two	0.642924	0.677752
VAE	Gaussian process	Two	0.631617	0.675007
VAE	Gaussian process	One	0.631354	0.676044
NMF	Random forest	One	0.621269	0.646555
PCA	Gaussian process	Two	0.516954	0.683877
PCA	Gaussian process	One	0.516913	0.684464
PCA	Logistic regression	One	0.500040	0.638890
AE	Logistic regression	One	0.500000	0.639670
NMF	Logistic regression	One	0.500000	0.642166
VAE	Logistic regression	One	0.500000	0.640058

### S14.2: Optimal model by prescriptive balanced accuracy: AE, two-model ExtraTrees

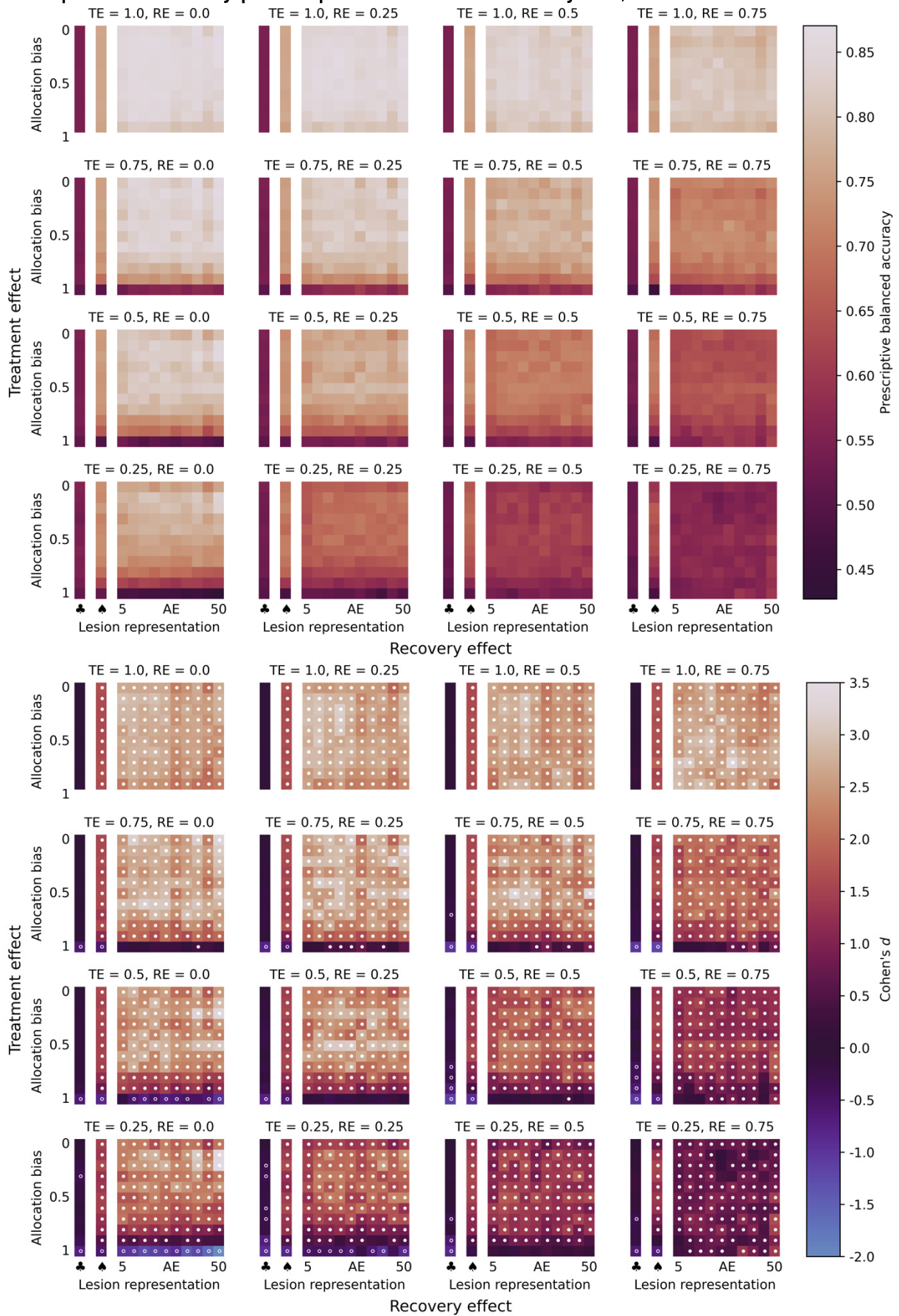


**Figure S14.2. Performance comparison of models with disconnectome representations: balanced accuracy (upper panel) and statistical analysis (lower panel).** Prescriptive performance of an optimized, extremely randomized trees-based treatment recommendation system, given lesion disconnectome representations, across the range of response noise (major axes) and allocation bias (minor y-axes), at various levels of expressivity of the individualized representation quantified by embedding length (minor x-axes). The columns to the left of each minor axis show prescriptive performance when individual phenotypes are represented by classification of major affected arterial territory: anterior or posterior circulation (♣) and ACA/MCA/posterior cerebral artery/VB (♠). The upper left subplot shows performance under zero response noise and the lower right subplot shows performance under the conditions of extremely high response noise. The top row of each subplot shows perfect randomization, with zero allocation bias. The upper panel shows prescriptive performance measured by balanced accuracy—the mean proportion of patients allocated to the treatment for which they are truly susceptible—for patients that are exclusively susceptible to one treatment.

The lower panel shows Cohen's  $d$ -effect sizes, by colour, when comparing the prescriptive performance (measured by balanced accuracy, as shown in the upper panel) against a randomized trial based upon individualized information consisting of the major vascular supply (anterior or posterior circulation), at each respective TE/RE pair. Warm colours show performance greater than the comparative randomized trial, while cool colours show the converse. White shows equivalent performance. Trials marked with a circle indicate an effect size exceeding the critical  $p$ -value 0.0429 (as adjusted for multiple comparisons at the 0.05 significance level, according to the Benjamini-Hochberg procedure), corresponding to the  $t$ -value in a two-sided independent sample  $t$ -test. Filled circles show superiority of the prescriptive model from observational data; unfilled circles show superiority of the randomized trial.

TE: treatment effect; RE: recovery effect; AE: auto-encoder representation; ACA: anterior cerebral artery; MCA: middle cerebral artery; VB: vertebrobasilar artery

### S14.3: Best-performing by PEHE: AE, two-model logistic regression

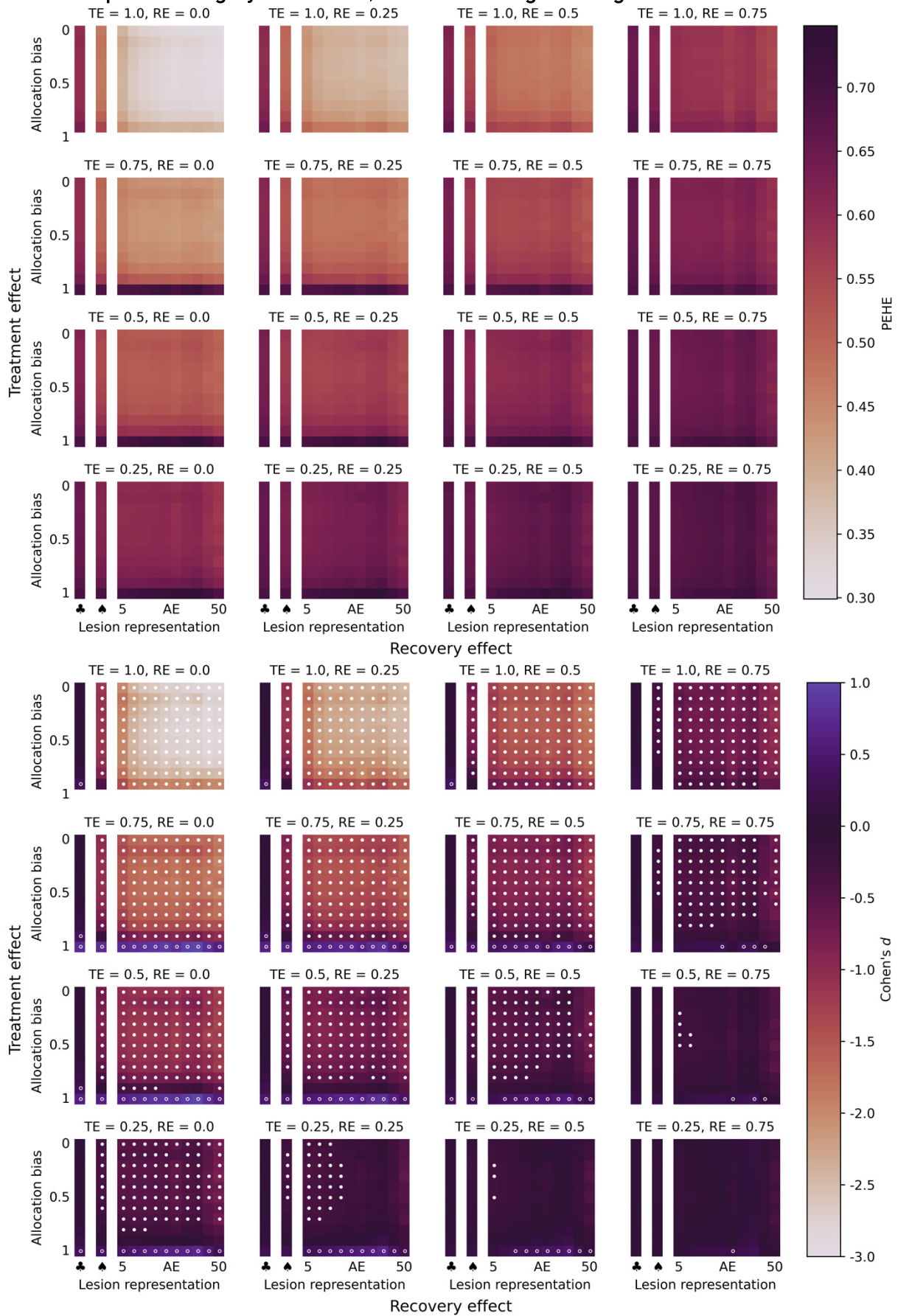


**Figure S14.3. Performance comparison of models with disconnectome representations: PEHE (upper panel) and statistical analysis (lower panel).** Prescriptive performance of an optimized, logistic regression-based treatment recommendation system, given lesion disconnectome representations, across the range of response noise (major axes) and allocation bias (minor  $y$ -axes), at various levels of expressivity of the individualized representation quantified by embedding length (minor  $x$ -axes). The columns to the left of each minor axis show prescriptive performance when individual phenotypes are represented by classification of major affected arterial territory: anterior or posterior circulation (♣) and ACA/MCA/posterior cerebral artery/VB (♠). The upper left subplot shows performance under zero response noise and the lower right subplot shows performance under the conditions of extremely high response noise. The top row of each subplot shows perfect randomization, with zero allocation bias. The upper panel shows prescriptive performance measured by PEHE the root-mean-squared-error in estimation of the true individualized treatment effect (lower is better).

The lower panel shows Cohen's  $d$ -effect sizes, by colour, when comparing the prescriptive performance (measured by PEHE, as shown in the upper panel) against a randomized trial based upon individualized information consisting of the major vascular supply (anterior or posterior circulation), at each respective TE/RE pair. Warm colours show performance greater than the comparative randomized trial, while cool colours show the converse. White shows equivalent performance. Trials marked with a circle indicate an effect size exceeding the critical  $p$ -value 0.0327 (as adjusted for multiple comparisons at the 0.05 significance level, according to the Benjamini-Hochberg procedure), corresponding to the  $t$ -value in a two-sided independent sample  $t$ -test. Filled circles show superiority of the prescriptive model from observational data; unfilled circles show superiority of the randomized trial.

TE: treatment effect; RE: recovery effect; AE: auto-encoder representation; ACA: anterior cerebral artery; MCA: middle cerebral artery; VB: vertebrobasilar artery

## S15: Results summary by PEHE

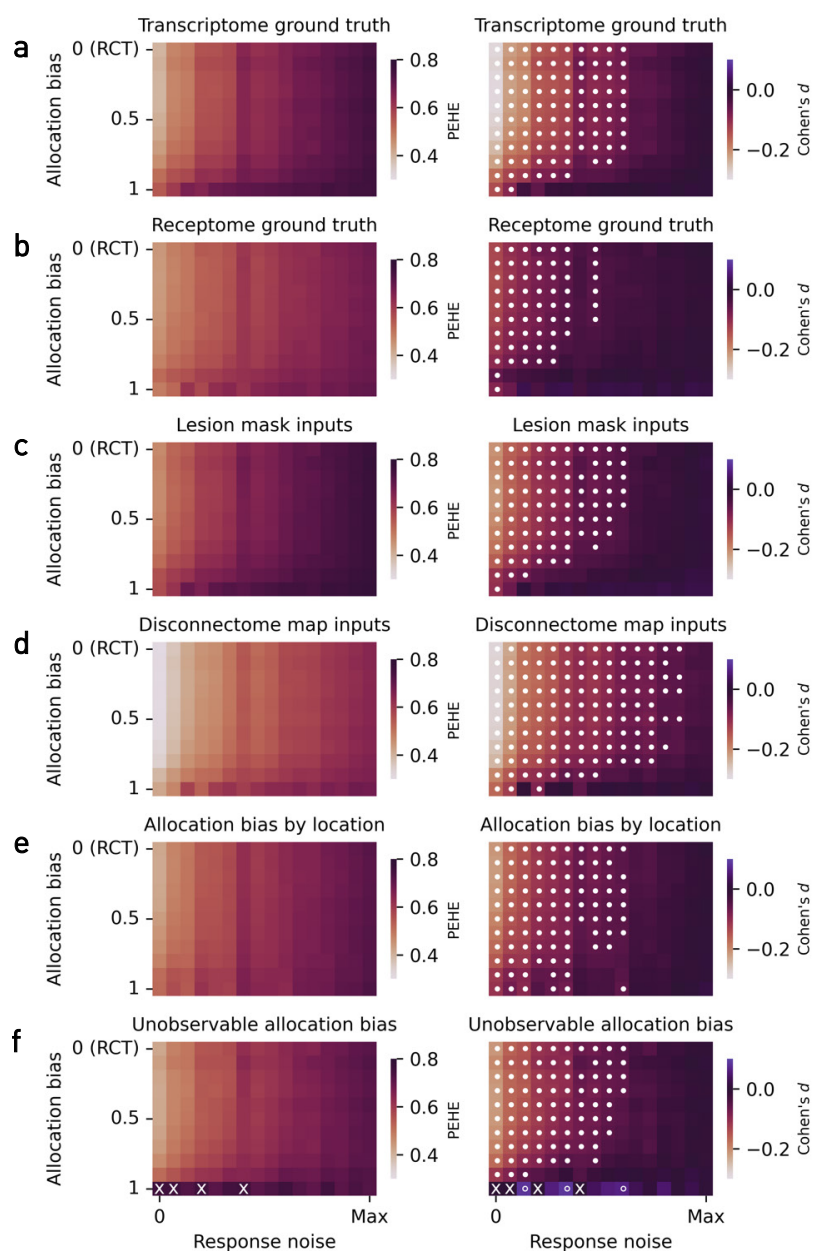


**Figure S15.** Prescriptive performance with the optimal richly expressive representation quantified by PEHE (left panel column, see Supplementary S11-S14 for full descriptions), and statistical comparison against a simple vascular baseline (anterior or posterior vascular territories) (right panel column). A filled circle indicates significantly higher performance for the expressive representation, and an unfilled circle significantly higher performance for the baseline model (using a Benjamini-Hochberg corrected critical value for 0.05 significance level). An 'x' indicates simulation conditions with insufficient class balance to permit prescriptive model fitting (e.g. because there are no non-responders). Rows **a** and **b** show performance averaged across the criteria for treatment susceptibility (transcriptome or receptome); rows **c** and **d** across lesion input representation type (lesion masks or disconnectomes); and rows **e** and **f** across allocation bias observability (location-based or unobservable). The optimal expressive representation is shown to be non-inferior to simple vascular territories at informing prescription across almost the full landscape of observational conditions, and superior in the majority. See Figure 6 for respective balanced accuracy plots.

## S16: Results summary, stratified by deficit, by PEHE

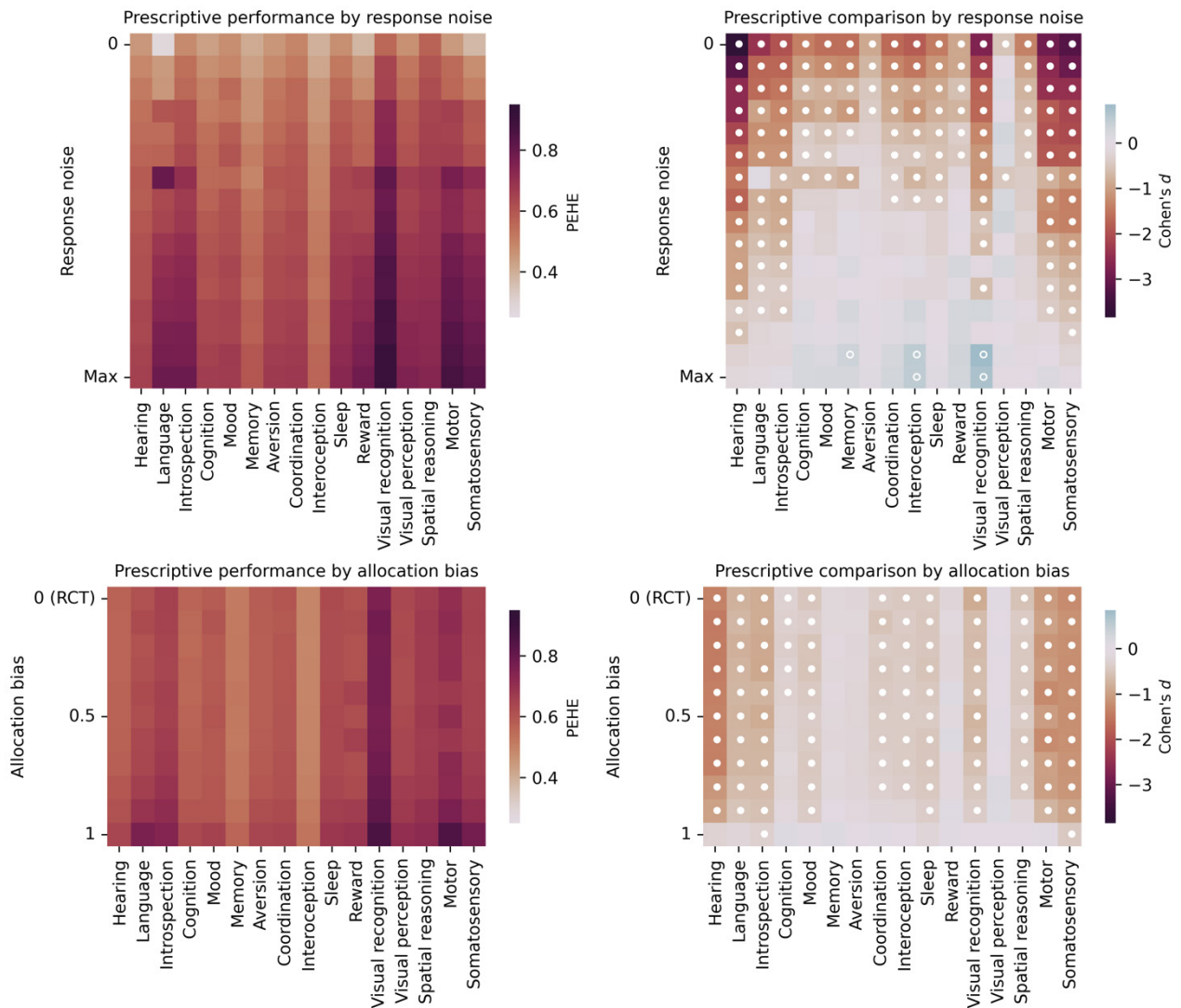


**Figure S16.** Prescriptive performance with the optimal richly expressive representation quantified by PEHE (see S11-S14 for full description), stratified according to the modelled functional deficit, and averaged across all simulation conditions. The right column shows Cohen's  $d$ -effect size when comparing prescriptive performance using the optimal representation against a simple vascular baseline. A filled circle indicates superior performance for the optimal representation, beyond the Benjamini-Hochberg corrected critical value for 0.05 significance level; an unfilled circle indicates superior performance for the simple vascular baseline correspondingly. The full anatomical—physiological modelling framework is visualized in Supplementary S9 & S10 for receptome and transcriptome, respectively. The advantage in prescriptive performance for the richly expressive approach is shown to generalize across modelled functional deficits as well as data conditions defined by outcome response noise and treatment allocation bias. See Figure 7 for respective balanced accuracy plot.

## S17: Performance comparison under ideal experimental conditions

### Prescriptive balanced accuracy; lesion representation; location bias

Representation	Embedding length	Prescriptive model	Inferential configuration	Performance (95% CI)	Control (95% CI)	<i>t</i>	<i>p</i>	<i>d</i>
VAE	30	ExtraTrees	Two-model	0.778 (0.74, 0.84)	0.521 (0.48, 0.56)	5.78	0.0000038	1.76

### Prescriptive balanced accuracy; lesion representation; unobservable bias

Representation	Embedding length	Prescriptive model	Inferential configuration	Performance (95% CI)	Control (95% CI)	<i>t</i>	<i>p</i>	<i>d</i>
AE	25	ExtraTrees	Two-model	0.773 (0.71, 0.84)	0.524 (0.48, 0.57)	5.98	0.0000019	1.70

### Prescriptive balanced accuracy; disconnectome representation; location bias

Representation	Embedding length	Prescriptive model	Inferential configuration	Performance (95% CI)	Control (95% CI)	<i>t</i>	<i>p</i>	<i>d</i>
AE	50	ExtraTrees	Two-model	0.873 (0.80, 0.94)	0.546 (0.51, 0.58)	8.85	0.000000024	2.63

### Prescriptive balanced accuracy; disconnectome representation; unobservable bias

Representation	Embedding length	Prescriptive model	Inferential configuration	Performance (95% CI)	Control (95% CI)	<i>t</i>	<i>p</i>	<i>d</i>
AE	50	ExtraTrees	Two-model	0.862 (0.79, 0.94)	0.546 (0.51, 0.58)	8.29	0.000000098	2.52

### Observed PEHE; lesion representation; location bias

Representation	Embedding length	Prescriptive model	Inferential configuration	Performance (95% CI)	Control (95% CI)	<i>t</i>	<i>p</i>	<i>d</i>
AE	25	ExtraTrees	Two-model	0.465 (0.42, 0.50)	0.676 (0.61, 0.74)	-5.53	0.0000058	-1.44

### Observed PEHE; lesion representation; unobservable bias

Representation	Embedding length	Prescriptive model	Inferential configuration	Performance (95% CI)	Control (95% CI)	<i>t</i>	<i>p</i>	<i>d</i>
Lateralized arterial territory atlas	N/A	Random forest	Two-model	0.516 (0.46, 0.57)	0.676 (0.62, 0.73)	-3.71	0.00083	-0.957

### Observed PEHE; disconnectome representation; location bias

Representation	Embedding length	Prescriptive model	Inferential configuration	Performance (95% CI)	Control (95% CI)	<i>t</i>	<i>p</i>	<i>d</i>
VAE	50	Logistic regression	Two-model	0.305 (0.26, 0.34)	0.592 (0.54, 0.64)	-6.04	0.0000066	-2.27

### Observed PEHE; disconnectome representation; unobservable bias

Representation	Embedding length	Prescriptive model	Inferential configuration	Performance (95% CI)	Control (95% CI)	<i>t</i>	<i>p</i>	<i>d</i>
VAE	50	Logistic regression	Two-model	0.304 (0.27, 0.34)	0.592 (0.54, 0.64)	-6.33	0.0000028	-2.34